

1

2 **A global model simulation of present and future nitrate** 3 **aerosols and their direct radiative forcing of climate**

4

5 **Didier A. Hauglustaine^{1,*}, Yves Balkanski¹, and Michael Schulz²**

6 [1]{Laboratoire des Sciences du Climat et de l'Environnement (LSCE), UMR 8212, CEA-
7 CNRS-UVSQ, Gif-sur-Yvette, France}

8 [2]{Norwegian Meteorological Institute, Blindern, Norway}

9 [*]{Also at Laboratoire Image Ville Environnement (LIVE), UMR 7362, CNRS-UdS,
10 Strasbourg, France}

11 Correspondence to : D. A. Hauglustaine (didier.hauglustaine@lsce.ipsl.fr)

12

13 **Abstract**

14 The ammonia cycle and nitrate particle formation have been introduced in the LMDz-INCA
15 global model. An important aspect of this new model is that both fine nitrate particle
16 formation in the accumulation mode and coarse nitrate forming on existing dust and sea-salt
17 particles are considered. The model simulates distributions of nitrates and related species in
18 agreement with previous studies and observations. The calculated present-day total nitrate
19 direct radiative forcing since the pre-industrial is -0.056 W/m^2 . This forcing corresponds to
20 18% of the sulfate forcing. Fine particles largely dominate the nitrate forcing representing
21 close to 90% of this value. The model has been used to investigate the future changes in
22 nitrates and direct radiative forcing of climate based on snapshot simulations for the four
23 Representative Concentration Pathway (RCP) scenarios and for the 2030, 2050 and 2100 time
24 horizons. Due to a decrease in fossil fuel emissions in the future, the concentration of most of
25 the species involved in the nitrate-ammonium-sulfate system drop by 2100 except for
26 ammonia which originates from agricultural practices and for which emissions significantly
27 increase in the future. Despite the decrease of nitrate surface levels in Europe and Northern
28 America, the global burden of accumulation mode nitrates increases by up to a factor of 2.6 in

29 2100. This increase in ammonium nitrate in the future arises despite decreasing NO_x
30 emissions due to increased availability of ammonia to form ammonium nitrate. The total
31 aerosol direct forcing decreases from its present-day value of -0.234 W/m^2 to a range of -
32 0.070 to -0.130 W/m^2 in 2100 based on the considered scenario. The direct forcing decreases
33 for all aerosols except for nitrates for which the direct negative forcing increases to a range of
34 -0.060 to -0.115 W/m^2 in 2100. Including nitrates in the radiative forcing calculations
35 increases the total direct forcing of aerosols by a factor of 1.3 in 2000, by a factor of 1.7-2.6 in
36 2030, by 1.9-4.8 in 2050 and by 6.4-8.6 in 2100. These results show that agricultural
37 emissions of ammonia will play a key role in the future mitigation of climate change with
38 nitrates becoming the dominant contributor to the anthropogenic aerosol optical depth during
39 the second half of the XXIst century and significantly increasing the calculated aerosol direct
40 forcing. This significant increase in the influence that nitrate exerts on climate in the future
41 will at the same time affect regional air quality and nitrogen deposition to the ecosystems.

42

43 **1. Introduction**

44 The formation of ammonium nitrate particles in the atmosphere is a secondary process
45 initiated by the oxidation of NO_2 to nitric acid (HNO_3) and by its further reaction with
46 ammonia (NH_3). HNO_3 can also be absorbed on existing particulate matter to form coarse
47 nitrate aerosols (Li and Shao, 2009). Nitrogen oxide emissions are mostly associated with
48 fossil fuel combustion (40%), land use practices (15%) and soil emissions (10%) (Olivier et
49 al., 1998). In contrast, global ammonia emissions into the atmosphere are dominated by
50 agricultural practices (Bouwman et al., 1997). In western Europe and in the United States as
51 much as 90%-100% of NH_3 emissions results from animal and crop agriculture (Sutton et al.,
52 2000; Hertel et al., 2011). In the atmosphere, NH_3 reacts not only with HNO_3 but also with
53 other acid gases such as H_2SO_4 to form ammonium (NH_4^+) containing particles. Atmospheric
54 nitrate particles have an adverse impact on health. In Europe, for instance, these particles
55 account today for about 10-20% of the total dry aerosol mass (Putaud et al., 2004a; Schaap et
56 al., 2004). These particles also contribute to the deposition of nitrogen to the surface with a
57 cascade of advert effects on terrestrial and aquatic ecosystems and possible consequences for
58 the global carbon cycle (Gruber and Galloway, 2008). Moreover, nitrate particles have the
59 potential to directly affect the Earth's radiation budget by reflecting solar radiation and
60 climate through their effect on cloud formation and precipitation (Forster et al., 2007).

61 Several global models have been used to simulate the nitrate-ammonium-sulfate aerosol
62 system and their impact on the present-day climate (e.g., van Dorland et al., 1997; Adams et
63 al., 2001; Jacobson, 2001; Martin et al., 2004; Liao and Seinfeld, 2005; Myhre et al., 2006;
64 Bauer et al., 2007; Bellouin et al., 2011; Xu and Penner, 2012). These earlier studies have
65 reported direct radiative forcings ranging from -0.02 W/m^2 to -0.19 W/m^2 . The uncertainty on
66 the nitrate particle radiative forcing of climate remains high. Recently, Myhre et al. (2013)
67 compiled the nitrate forcings calculated in the framework of AeroCom phase II by 8 global
68 models and derived a present-day direct radiative forcing for the most recent model versions
69 ranging from -0.03 W/m^2 to -0.17 W/m^2 and a mean of $-0.10 \pm 0.04 \text{ W/m}^2$. For the ACCMIP
70 historical simulations, Shindell et al. (2013) derived a direct forcing for nitrates ranging from
71 -0.03 W/m^2 to -0.41 W/m^2 , with a mean of $-0.19 \pm 0.18 \text{ W/m}^2$. Fewer studies have assessed the
72 future radiative forcing of nitrate particles. Adams et al. (2001), Liao and Seinfeld (2005), and
73 Liao et al. (2009) investigated the future evolution of nitrates under the emission scenario
74 SRES A2 and derived a direct anthropogenic radiative forcing reaching -0.95 to -1.28 W/m^2
75 in 2100. Bauer et al. (2007) also investigated the evolution of nitrates in 2030 following the
76 SRES A1B emission scenario. All these studies pointed out the steady increase of nitrate
77 aerosols since industrialization and associated direct radiative forcing of climate. They also
78 suggest that the decreased radiative forcing from sulfates particles in the future associated
79 with reduced emissions of SO_2 could be partially offset by the increased nitrate forcing since
80 the formation of ammonium nitrates is favored at lower sulfate loadings. More recently
81 Bellouin et al. (2011) included nitrate aerosols in their future CMIP5 simulations driven by
82 the RCP scenarios and indicated that nitrates could become an important aerosol species in
83 the future making the aerosol radiative forcing 2-4 times stronger by 2100.

84 In this paper, the atmospheric ammonia cycle and nitrate particle formation are introduced in
85 the LMDz-INCA global three-dimensional climate-chemistry model. Numerous detailed
86 models have been developed in order to treat the partitioning of nitrate and ammonium
87 between the gas phase and the aerosol phase assuming thermodynamical equilibrium between
88 phases (e.g., Pilinis and Seinfeld, 1987; Zhang et al., 2000; Metzger et al., 2002a; Metzger et
89 al., 2006) or treating the dynamical mass transfer between each aerosol size bin explicitly
90 (e.g., Pilinis et al., 2000; Jacobson, 1999; Sun and Wexler, 1998; Lauer et al., 2005). In order
91 to apply these computationally expensive models at the global scale, several authors have
92 chosen to apply parameterizations for the relationships between activity coefficients and the
93 relative humidity (Metzger et al., 2002ab; Myhre et al., 2006; Bauer et al., 2007; Pringle et al.,

94 2010) or to use an hybrid dynamic method (Feng and Penner, 2007; Xu and Penner, 2012). In
95 this study, since the LMDz-INCA general circulation model is designed for long term
96 simulations, we also use a simplified approach, and the phase equilibrium of the ammonium-
97 sulfate-nitrate aerosol system is introduced for fine particles based on the simple
98 thermodynamical formulation used initially in regional acid deposition chemical transport
99 models (Hov et al., 1988; Ackermann et al., 1995), in global chemical transport models (Tie
100 et al., 2005), and more recently in an Earth system model (Bellouin et al., 2011). In addition
101 to this formation of fine nitrate particles in the accumulation mode, the role of nitric acid
102 uptake on mineral dust and sea-salt particles to form coated coarse nitrate particles can also
103 play an important role in the total nitrate and nitric acid budget in the atmosphere and hence
104 on the radiative forcing (e.g., Liao and Seinfeld, 2005; Myhre et al., 2006; Bauer et al., 2007;
105 Feng and Penner, 2007; Xu and Penner, 2012). The formation of coarse nitrate particles on
106 dust and on sea-salt particles is introduced in LMDz-INCA adopting a first-order removal.
107 This method is computationally efficient and has often been used in global models (e.g.,
108 Dentener and Crutzen, 1993; Bauer et al., 2004, 2007; Evans et al., 2005; Fairlie et al., 2010)
109 despite the fact that limitations for this formulation exist (Feng and Penner, 2007). An
110 evaluation of the simulated aerosol distributions calculated with the LMDz-INCA model, of
111 the optical depth and surface nitrate and sulfate depositions are performed. Based on the
112 recent RCP CMIP5 emission scenarios we then use the model to calculate the present-day and
113 future anthropogenic direct radiative forcing of fine and coarse nitrate particules and to assess
114 the relative contribution of nitrates to the aerosol optical depth and radiative forcing.

115 The three-dimensional global model used in this study and the extension of the chemical and
116 aerosol scheme to include ammonia and nitrate particles are described in Section 2. Section 3
117 presents the present-day global distributions of aerosols, the evaluation of the model results
118 and the direct radiative forcing of aerosols. The results of the future simulations in terms of
119 atmospheric composition, surface deposition and direct radiative forcing of climate are
120 presented in Section 4. Finally, section 5 gives the summary and conclusions.

121

122 **2. Model description**

123 **2.1 The LMDz-INCA model**

124 We use the LMDz-INCA global chemistry-aerosol-climate model coupling on-line the LMDz
125 (Laboratoire de **M**étéorologie **D**ynamique, version 4) General Circulation Model (Hourdin et
126 al., 2006) and the INCA (**I**Nteraction with **C**hemistry and **A**erosols, version 3) model
127 (Hauglustaine et al., 2004). The interaction between the atmosphere and the land surface is
128 ensured through the coupling of LMDz with the ORCHIDEE (**O**Rganizing **C**arbon and
129 **H**ydrology **I**n **D**ynamic **E**cosystems, version 9) dynamical vegetation model (Krinner et al.,
130 2005). In the present configuration, the model includes 19 hybrid vertical levels extending up
131 to 4 hPa. This corresponds to a vertical resolution of about 300–500 m in the planetary
132 boundary layer (first level at 70 m height) and to a resolution of about 2 km at the tropopause
133 (with 7–9 levels located in the stratosphere). The horizontal resolution is 1.9° in latitude and
134 3.75° in longitude. The primitive equations in the GCM are solved with a 3 min time-step,
135 large-scale transport of tracers is carried out every 15 min, and physical and chemical
136 processes are calculated at a 30 min time interval. For a more detailed description and an
137 extended evaluation of the GCM we refer to Hourdin et al. (2006). The large-scale advection
138 of tracers is calculated based on a monotonic finite-volume second-order scheme (Van Leer,
139 1977; Hourdin and Armengaud 1999). Deep convection is parameterized according to the
140 scheme of Emanuel (1991). The turbulent mixing in the planetary boundary layer is based on
141 a local second-order closure formalism. The transport and mixing of tracers in the LMDz
142 GCM have been investigated and evaluated against observations for both inert tracers (e.g.,
143 Hourdin and Issartel, 2000; Hauglustaine et al., 2004; Rivier et al., 2005) and in the
144 framework of inverse modelling studies (e.g., Bousquet et al., 2005; Pison et al., 2009;
145 Bousquet et al., 2010). These studies concluded that the model at this vertical resolution is
146 well suited for the transport of tracers and chemical species. However it was also pointed out
147 that the simulated inter-hemispheric exchange time is 1.1 years for fossil CO₂ (Hauglustaine
148 et al., 2004), in the lowest part of the range (1.1–2.1 years) provided by TRANSCOM model
149 inter-comparison (Law et al., 1996). This means that LMDz has one of the fastest inter-
150 hemispheric mixing among the models of TRANSCOM and hence efficient mixing and
151 transport of pollutants. INCA includes a state-of-the-art CH₄-NO_x-CO-NMHC-O₃
152 tropospheric photochemistry (Hauglustaine et al., 2004; Folberth et al., 2006). The
153 tropospheric photochemistry and aerosols scheme used in this model version is described
154 through a total of 123 tracers including 22 tracers to represent aerosols. The model includes
155 234 homogeneous chemical reactions, 43 photolytic reactions and 30 heterogeneous reactions.
156 Please refer to Hauglustaine et al. (2004) and Folberth et al. (2006) for the list of reactions
157 included in the chemical scheme. The gas-phase version of the model has been extensively

158 compared to observations in the lower-troposphere (e.g., Hauglustaine et al., 2004; Folberth et
159 al., 2006; Fiore et al., 2009; Reidmiller et al., 2009), and in the upper-troposphere (e.g.,
160 Brunner et al., 2003; Dufour et al., 2007). For aerosols, the INCA model simulates the
161 distribution of aerosols with anthropogenic sources such as sulfates, black carbon, particulate
162 organic matter, as well as natural aerosols such as sea-salt and dust. The aerosol model keeps
163 track of both the number and the mass of aerosols using a modal approach to treat the size
164 distribution, which is described by a superposition of 5 log-normal modes (Schulz et al., 1998;
165 Schulz, 2007), each with fixed spread. To treat the optically relevant aerosol size diversity,
166 particle modes exist for three ranges: sub-micronic (diameter $< 1\mu\text{m}$) corresponding to the
167 accumulation mode, micronic (diameter between 1 and $10\mu\text{m}$) corresponding to coarse
168 particles, and super-micronic or super coarse particles (diameter $> 10\mu\text{m}$). This treatment in
169 modes is computationally much more efficient compared to a bin-scheme (Schulz et al.,
170 1998). Furthermore, to account for the diversity in chemical composition, hygroscopicity, and
171 mixing state, we distinguish between soluble and insoluble modes. In both sub-micron and
172 micron size, soluble and insoluble aerosols are treated separately. Sea-salt, SO_4 and methane
173 sulfonic acid (MSA) are treated as soluble components of the aerosol, dust is treated as
174 insoluble, whereas black carbon (BC) and particulate organic matter (POM) appear both in
175 the soluble and insoluble fractions. The ageing of primary insoluble carbonaceous particles
176 transfers insoluble aerosol number and mass to soluble with a half-life of 1.1 days (Cooke and
177 Wilson, 1996; Chung et al., 2002).

178 The uptake and loss of water from aerosol particles is generally fast and depends on the
179 chemical composition, size and surface properties of the aerosol particle. Aerosol water is
180 responsible for about 50% of the global aerosol column load. This water uptake modifies the
181 aerosol optical properties. We use a formulation of the optical depth, τ , first implemented by
182 Chin et al. (2002) to write τ as a function of the aerosol dry burden M_d (kg m^{-2}):

$$183 \quad \tau = \beta M_d (1)$$

184 where β , the specific extinction ($\text{m}^2 \text{kg}^{-1}$), is computed as follows:

$$185 \quad \beta = 3 Q M / 4 \rho r_e M_d (2)$$

186 where Q is the extinction coefficient (dimensionless) computed using Mie theory, M , is the
187 aerosol burden per unit area (kg m^{-2}), ρ is the particle density (kg m^{-3}), and r_e , the effective
188 radius (m). As relative humidity increases, this equation has to be modified to account for the

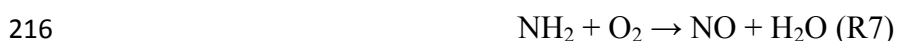
189 presence of water. The density is then recomputed as the mass-weighted sum of the dry
190 density of the aerosol and the density of water. The refractive index, hence the extinction, is
191 also changed to account for water.

192 The optical properties and hygroscopic growth of sea-salt were taken from Irshad et al.
193 (2005). For sulfates, we followed the relationships published for ammonium sulfate by Martin
194 et al. (2003). In the case of black carbon and organic carbon we took the same dependence of
195 hygroscopic growth on relative humidity as Chin et al (2002). The aerosol scheme is
196 thoroughly explained in Schulz (2007) and Balkanski (2011). Characteristic global aerosol
197 properties of the INCA model have been described and compared in all AeroCom
198 publications, as for instant recently in Myhre et al. (2013) and Koffi et al. (2012). We also
199 refer to Szopa et al. (2012) for a simulation of the global aerosol components (excluding
200 nitrates) and tropospheric ozone distributions and their associated radiative forcings between
201 1850 and 2100 following a recent historical emission dataset (Lamarque et al., 2010) and
202 under the representative concentration pathways (RCP) (Lamarque et al., 2011) for the future
203 with the same version of the model.

204

205 **2.2 Ammonia and nitrate particles**

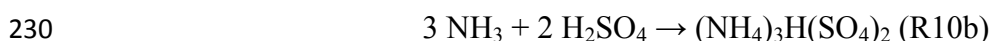
206 The LMDz-INCA chemical scheme has been extended in order to include the ammonia cycle
207 and the nitrate particle formation. The various NH₃ emissions have been introduced in the
208 model as described in the next section. Ammonia undergoes several gas phase reactions
209 which have been introduced in the model chemical mechanism:





219 The rate constants for these reactions are taken from Sander et al. (2011).

220 The most abundant acids in the troposphere are sulfuric acid (H_2SO_4) and nitric acid (HNO_3).
221 Ammonia acts as the main neutralizing agent for these two species. Therefore, formulating the
222 respective aerosol particle formation scheme as a purely sulfate-nitrate-ammonia system
223 seems to be a reasonable assumption for a global chemistry-aerosol-climate model. However,
224 we also remove nitric acid through reaction with sea salt and dust, as described below. As a
225 first step, ammonium sulfate is formed instantaneously and irreversibly from NH_3 and H_2SO_4 ,
226 only limited by the availability of the less abundant of the two species. The concentration of
227 NH_3 and SO_4 are depleted upon formation of ammonium sulfate which takes priority over
228 ammonium nitrate formation due to the low vapour pressure of sulphuric acid:



232 As in Metzger et al. (2002), three domains are considered to characterize the neutralization
233 state of the ammonium sulfate ion formed, depending on the relative ammonia and sulfate
234 concentrations. The total nitrate (T_N), total ammonia (T_A), and total sulfate (T_S)
235 concentrations are defined as:

236
$$T_N = [\text{HNO}_3] + [\text{NO}_3^-] \quad (3)$$

237
$$T_A = [\text{NH}_3] + [\text{NH}_4^+] \quad (4)$$

238
$$T_S = [\text{SO}_4^{=}] \quad (5)$$

239 If $T_A > 2 T_S$, ammonia rich condition (sulfate state $\Gamma=2.0$), the reaction pathway is provided
240 by the chemical reaction (R10c); if $T_A < 2 T_S$, sulfate rich condition (sulfate state $\Gamma=1.5$),
241 reaction (R10b) is considered; and if $T_A < T_S$, sulfate very rich condition (sulfate state $\Gamma=1.0$),
242 the reaction occurs through (R10a).

243 In a second step, if all free ammonia is consumed by the sulfate forming reaction, no
244 ammonium nitrate is formed. If free ammonia persists, it is used for the neutralization of nitric
245 acid to ammonium nitrate aerosol following the equilibrium reaction:



247 The equilibrium constant (K_p) of (R11) strongly depends on relative humidity and
248 temperature. The parameterization used for this dependence is based on Mozurkewich (1993)
249 and the deliquescence relative humidity is calculated based on Seinfeld and Pandis (1998)
250 (see Supplementary Material for more details).

251 The equilibrium concentration of ammonium nitrate is then calculated based on Seinfeld and
252 Pandis (1998). The free ammonia in the system is defined as the total ammonia minus the
253 ammonia required to neutralize the available sulfate:

$$254 \quad T_A^* = T_A - \Gamma T_S \text{ (6)}$$

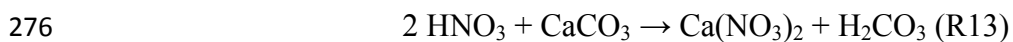
255 If $T_N T_A^* > K_p$, the ammonium nitrate concentration is calculated according to:

$$256 \quad [\text{NH}_4\text{NO}_3] = \frac{1}{2} \left[T_A^* + T_N - \sqrt{(T_A^* + T_N)^2 - 4(T_N T_A^* - K_p)} \right] \text{ (7)}$$

257 Elsewhere, ammonium nitrate dissociates and $[\text{NH}_4\text{NO}_3] = 0$. The concentration of NH_3 and
258 HNO_3 are depleted or replenished to account for ammonium nitrate formation or dissociation,
259 respectively. The chemical formation of ammonium sulfate particles according to (R10) and
260 of ammonium nitrate particles according to reaction (R11) goes into the accumulation mode.
261 The formation of nitrates through (R11) is also associated with a corresponding increase in
262 the number of particles in the accumulation mode reflecting the formation of new ammonium
263 nitrate particles. This thermodynamic model has been run as a box model and the results
264 carefully evaluated against the reference model ISORROPIA (Nenes et al., 1998). For this
265 evaluation the main parameters controlling the nitrate and ammonium aerosol concentrations
266 have been varied over specified intervals and the calculated concentrations compared to
267 ISORROPIA results. A fairly good agreement between both model results has been achieved
268 over the range of key parameters currently encountered in the global model version (see
269 Supplementary Material for more details).

270 Gaseous HNO_3 can condense on both accumulation mode and coarse particles. As in Myhre et
271 al. (2006), first photochemistry and accumulation mode aerosol formation are solved because

272 the smaller particles reach equilibrium faster than the larger ones. After the small particles are
 273 in equilibrium, the concentration of gaseous HNO₃ is updated for the condensation on coarse
 274 particles. We account for the heterogeneous reaction of HNO₃ with dust and sea-salt particles:



277 We use a standard first-order reactive uptake parameterisation to represent the uptake of
 278 HNO₃ on pre-existing dust and sea-salt particles in the model and formation of coarse nitrate
 279 particles (Dentener and Crutzen, 1993; Bauer et al., 2004; Fairlie et al., 2010). The rate
 280 constants k_{12} and k_{13} of reactions (R12) and (R13), which describe the loss of HNO₃ from the
 281 gas phase, are calculated from (Schwartz, 1986):

282
$$k_{12,13} = \int_{r_i}^{r_f} 4\pi r^2 N(r) \left(\frac{r}{D_g} + \frac{4}{v\gamma} \right)^{-1} dr \text{ (8)}$$

283 where N is the number density of dust or sea-salt particles of radius $[r, r+dr]$, D_g is the
 284 calculated, pressure and temperature dependent, molecular diffusion coefficient ($\text{cm}^2 \text{ s}^{-1}$), v
 285 the calculated, temperature dependent, mean molecular speed (cm s^{-1}), and γ the reactive
 286 uptake coefficient. Equation (8) is integrated from $r_i=0.01$ to $r_f=30\mu\text{m}$. As mentioned by Feng
 287 et al. (2007), a major limitation of this first-order formulation is the lack of relative humidity
 288 dependence for the uptake. To overcome partly this limitation, for the reaction on dust
 289 particles, we use the RH dependent uptake coefficient proposed by Fairlie et al. (2010). Based
 290 on this RH-dependence, γ increases from 1×10^{-5} for RH lower than 10% up to 1.05×10^{-3} for RH
 291 larger than 80%. Another limitation mentioned by Feng et al. (2007) is the lack of dependence
 292 of the uptake coefficient on the aerosol chemical composition. As in Fairlie et al. (2010), we
 293 introduce a Ca^{2+} limitation for the uptake of HNO₃ on dust through (R13). Based on dust
 294 source maps (Claquin et al., 1999), it is assumed that Ca^{2+} constitutes 5% of the dust mass.
 295 Dust alkalinity is then consumed by the uptake of HNO₃. Once the alkalinity is titrated by the
 296 formation of nitrates, the uptake of HNO₃ through (R13) ceases. For sea-salt particles, the
 297 same dependence is used for the γ increase with RH. The values are scaled to the
 298 accommodation coefficients compiled by Sander et al. (2011) and γ increases from 1×10^{-3} for
 299 RH lower than 10% up to 1×10^{-1} for RH larger than 80%. No alkalinity limitation is
 300 considered for sea-salt particles.

301 These new gaseous species and particles introduced in the model to represent the ammonia
302 cycle, the formation of ammonium sulfate, ammonium nitrate and coarse nitrates on dust and
303 sea-salt are subject to the same transport and mixing processes as the other tracers in the
304 model. The dry and wet deposition of NH_3 is introduced as described by Hauglustaine et al.
305 (2004) with an Henry's law coefficient taken from Sander et al. (2011). Ammonium nitrate
306 and ammonium sulfate are subject to the same dry and wet deposition processes as sulfate
307 particles already in the model and coarse nitrates on dust and sea-salt are deposited as the
308 corresponding dust and sea-salt components, respectively.

309 The hygroscopic growth of ammonium nitrate has been characterized in the laboratory by
310 measuring droplet growth for different conditions of relative humidity by Tang (1996). The
311 optical properties of nitrate particles in the accumulation and coarse modes were obtained
312 through Mie calculation using the refractive indices for two overlapping spectral intervals.
313 Gosse et al. (1997) measured the refractive index of ammonium nitrate from 0.7 to 2.6 μm ,
314 whereas Jarzembski et al. (2003) covered the far visible to the infrared wavelengths from 2.0
315 to 20 μm . Values of specific extinction, asymmetry parameter and single scattering albedo
316 were tabulated for eleven values of relative humidities: from 0 to 90% with 10% increments
317 and finally for the 95% value. For a given relative humidity, we interpolate between the two
318 closest values, if relative humidity exceeds 95% then we take for optical parameters the
319 values deduced from the Mie theory at 95% relative humidity.

320

321 **2.3 Model set-up**

322 For the simulation of 'present' (2000) and 'pre-industrial' (1850) conditions, the
323 anthropogenic emissions compiled by Lamarque et al. (2010), are added to the natural fluxes
324 used in the INCA model. All natural emissions are kept at their present-day levels. For
325 organic aerosols, the secondary organic matter formed from biogenic emissions is equal to
326 that provided by the AeroCom emission dataset (Dentener et al., 2006a). The ORCHIDEE
327 vegetation model has been used to calculate off-line the biogenic surface fluxes of isoprene,
328 terpenes, acetone and methanol as well as NO soil emissions as described by Lathière et al.
329 (2006). NH_3 emissions from natural soils and ocean are taken from Bouwman et al. (1997).
330 Natural emissions of dust and sea salt are computed using the 10m wind components from the
331 the European Center for Medium-Range Weather Forecasts (ECMWF) reanalysis for 2006
332 and, consequently, have seasonal cycles but no inter-annual variability. For the future

333 simulations (2030, 2050, 2100), the four Representative Concentration Pathways (RCP)
334 anthropogenic and biomass burning emissions provided by Lamarque et al. (2011) are used.
335 Methodological elements used to build these projections can be found in Lamarque et al.
336 (2011). Natural emissions for both gaseous species and particles are kept to their present-day
337 level as described above. Table 1 gives the list of simulations performed and the
338 corresponding total and global emissions of key species discussed in this paper. In all RCP
339 scenarios, fossil fuel driven emissions, NO_x , SO_2 , BC and OC, decrease in 2100 compared to
340 2000 emissions. It is however interesting to note that NH_3 emissions, driven by agriculture,
341 increase in all scenarios from 50 TgN in 2000 to 54-79 TgN in 2100 depending on to the
342 considered scenario. As will be discussed in the next sections, this feature will have major
343 implications in terms of nitrate future radiative forcing of climate.

344 In this study, meteorological data from the ECMWF reanalysis have been used. The
345 relaxation of the GCM winds towards ECMWF meteorology is performed by applying at each
346 time step a correction term to the GCM u and v wind components with a relaxation time of
347 2.5 h (Hourdin and Issartel, 2000; Hauglustaine et al., 2004). The ECMWF fields are provided
348 every 6 hours and interpolated onto the LMDz grid. We focus this work on the distribution of
349 nitrate particles, its evolution under future anthropogenic emissions, and its direct radiative
350 forcing of climate. In order to isolate the impact of anthropogenic emission scenarios, all
351 snapshot simulations are performed under present-day climate conditions and run for a period
352 of two years. Therefore ECMWF meteorological data for 2005-2006 are used. The results for
353 the year 2005 are used as a spin-up. Results for 2006 conditions are presented in the next
354 sections. The impact of climate change on particles and chemistry is therefore not included in
355 the results. The role played by climate change and the impact of nitrate on the indirect aerosol
356 radiative forcing of climate will be investigated in a forthcoming study.

357

358 **3. Present-day distributions**

359 **3.1 Simulated aerosol distributions**

360 In this section we present the distributions of gaseous species and aerosols involved in the
361 formation of nitrate particles. Figure 1 shows the present-day annual mean surface
362 concentration of sulfates (SO_4^-), ammonium (NH_4^+) and total (fine + coarse) nitrates (NO_3^-)
363 aerosols. Please note that all concentrations and burdens are expressed in the following

364 sections in mass of the species (e.g. $\mu\text{g}/\text{m}^3$ for $\mu\text{g}\text{-NO}_3/\text{m}^3$) unless otherwise stated (e.g., $\mu\text{g}\text{-}$
365 N/m^3 or $\mu\text{g}\text{-S}/\text{m}^3$). Maximum sulfate concentrations are calculated over regions of high SO_2
366 emissions with marked maxima reaching 4-5 $\mu\text{g}/\text{m}^3$ over the Eastern United States, Southern
367 and Eastern Europe and China. The concentration of ammonium (associated both with
368 ammonium sulfate and ammonium nitrate) is localized over continental regions and reaches
369 maxima of 1-2 $\mu\text{g}/\text{m}^3$ over the central and eastern United States, 2-3 $\mu\text{g}/\text{m}^3$ in northern Europe
370 and 4-5 $\mu\text{g}/\text{m}^3$ in northern China. These regions combine both high concentrations of sulfates,
371 nitric acid but also high agricultural emissions of NH_3 . The distribution of surface nitrates
372 (fine mode + coarse mode) shows very strong concentrations in regions of high ammonia and
373 nitric acid concentrations (see below). This is in particular the case over northern Europe and
374 China with concentrations reaching 4-5 $\mu\text{g}/\text{m}^3$. The patterns of these surface distributions for
375 the three aerosol components are in general agreement with the recent global model results
376 presented by Pringle et al. (2010) and Xu and Penner (2012) and with the nitrate distributions
377 calculated by Myhre et al. (2006) and Bauer et al. (2007).

378 Figure 2 decomposes the total surface nitrate concentration shown in Figure 1 into its three
379 components: accumulation mode, coarse mode on dust particles and coarse mode on sea-salt
380 particles. The conditions for fine mode nitrate particle formation (expressed by equation 7)
381 are met over the continents and maximum concentrations are calculated, as already seen in
382 Figure 1, over regions of high agricultural emissions of NH_3 or high HNO_3 concentrations.
383 Coarse nitrate on dust follow the distribution of dust particles in the model (Bauer et al.,
384 2004). High concentrations reaching more than 0.5 $\mu\text{g}/\text{m}^3$, and locally up to 1-3 $\mu\text{g}/\text{m}^3$, are
385 calculated over the Sahara desert and the Saudi Arabian peninsula and extend to the
386 Mediterranean sea and southern Europe; over the western United States and over China. In
387 contrast, coarse nitrate on sea-salt reaches concentrations of 0.5-1 $\mu\text{g}/\text{m}^3$ in coastal areas
388 where high concentrations of sea-salt and nitric acid are met. These two coarse nitrate
389 components add up for a total of about 0.1-0.2 $\mu\text{g}/\text{m}^3$ over the ocean. Over the continents, fine
390 mode nitrates significantly dominate over source regions. However, in coastal regions or in
391 southern Europe all components mix and coarse nitrates can contribute to 30-40% to the total
392 concentration in these specific areas. The patterns of the calculated distribution of coarse
393 nitrates on dust and sea-salt is in fairly good agreement with the results presented by Myhre et
394 al. (2006), Bauer et al. (2007), and by Xu and Penner (2012).

395 In order to evaluate the model results, we have compared the simulated and measured surface
396 concentrations of SO_4^- , NH_4^+ , and NO_3^- from the EBAS database at NILU. EBAS holds data

397 from EMEP (emep.int), from the US National Atmospheric Deposition Program/National
398 Trend Network (NADP/NTN; <http://nadp.sws.uiuc.edu/NTN>), from the US Inter- agency
399 Monitoring of Protected Visual Environments (IMPROVE;
400 <http://vista.cira.colostate.edu/IMPROVE>), from the Clean Air Status and Trends Network
401 (CASTNET; <http://java.epa.gov/castnet>) and the EANET, Data on the Acid Deposition in the
402 East Asian Region (<http://www.eanet.cc/>). These comparisons have been prepared using the
403 AeroCom evaluation tools (Schulz et al., 2006). The aerosols measurements are mostly from
404 the CASTNET/IMPROVE network over Northern America, from the EMEP network in
405 Europe. This evaluation is performed for the year 2006 based on matching daily mean data,
406 averaged to monthly means. Table 2 summarizes the comparison with the measurements (see
407 Supplementary Material for individual plots per region and per species). For SO_4^{2-} , the
408 Normalized Mean Bias (difference between the arithmetic mean of the model minus the
409 arithmetic mean of the measurements relative to the mean measurements) is +20% for Europe
410 and +21% for Northern America. Worldwide the NMB is +20%. For ammonium
411 concentrations, the evaluation shows that NH_4^+ is overestimated worldwide with a NMB of
412 +50%. Over Europe, the NMB is +62% and, in contrast, NH_4^+ is slightly underestimated over
413 Northern America with a NMB of -16%. For nitrate concentrations, a worldwide overestimate
414 is obtained with a NMB of +68%. The comparison with the measurements are more
415 contrasted over the two regions, with smaller bias but smaller correlation over Europe (NMB
416 = +64%, $R=0.43$) than over Northern America (NMB=+115%, $R=0.54$). For NO_3^- , the bias is
417 mainly driven by an overestimate of observed concentrations in summer (NMB=+143%
418 worldwide) compared to winter (NMB=+22%). These comparisons are fairly good
419 considering the difficulty to represent station measurements with a large scale atmospheric
420 model. The comparison made for a specific year (2006) using an emission inventory
421 representative of the year 2000 is also a source of bias, which we estimate to be of the order
422 of 10-30% for European and American sites (Schulz et al., 2013). These results are generally
423 in line with the comparisons obtained with more detailed aerosol models (Adams et al., 1999;
424 Park et al., 2004; Pringle et al., 2010; Xu et al., 2012; Zhang et al., 2012; Heald et al., 2012)
425 or with a model of the same complexity (Bellouin et al., 2011). In particular, these studies
426 showed the difficulty to represent nitrates particles which is currently overestimated by a
427 factor of two at the surface by the global models due to the coarse model resolution, the
428 simplified aerosol chemistry and the limitations associated with the representation of physics
429 and transport in those models. In addition, it should be noticed that a positive bias in
430 simulated nitrate aerosol is suspected to be partly linked to negative sampling artefacts in

431 measurements, because evaporation of ammonium nitrate has been frequently reported to
432 create occasionally losses of up to 50%, in particular in warm weather (See Supplementary
433 Material for more details). Further work is needed to better characterize the individual nitrate
434 measurement error, to see where modeled nitrate is consistent with measurements.

435 It should also be noted that we focus this paper on monthly mean or annual mean distributions
436 of nitrate particles and their long-term evolution during the XXIst century. However, nitrate
437 aerosols have the ability to dissociate back into the gas phase. As a consequence, and as
438 illustrated by Dall'Osto et al. (2009), this means that nitrates have a pronounced diurnal cycle
439 and spend most of the daytime in the gas phase. This implies that the radiative forcing also
440 has a pronounced diurnal cycle. The detailed evaluation of the diurnal cycle is out of the scope
441 of the use of a global model and of this paper. However with a timestep of 30 min for
442 chemistry, a full diurnal cycle is simulated by LMDz-INCA. We found a pronounced diurnal
443 cycle in the model results superimposed on a variability associated with meteorological
444 conditions and transport of pollution episodes (see Supplementary Material). The simulated
445 concentrations of nitrates, their diurnal cycle and day-to-day variability are generally in line
446 with the measurements presented for instance by Dall'Osto et al. (2009).

447 Figure 3 shows the column burden of SO_4^- , NH_4^+ , and total NO_3^- . The sulfates column
448 reaches more than 3 mg/m^2 over the continents in the Northern Hemisphere. In the Eastern
449 US, Northern and Central Europe, the column reaches more than 5 mg/m^2 . The maximum
450 column of more than 10 mg/m^2 is reached over China. These values are slightly higher than
451 the column of 1-2 mg/m^2 calculated over the continents by Pringle et al. (2010) with a more
452 complex aerosol microphysics and partitioning model. The global mean column burden for
453 SO_4^- is 2.5 mg/m^2 , on the upper range of the recent model intercomparison by Myhre et al.
454 (2013), who reported a mean burden of $1.9 \pm 0.5 \text{ mg}/\text{m}^2$. The evaluation of the aerosol optical
455 depth will be important in order to evaluate those results (see below). The column burden of
456 NH_4^+ reaches 1-3 mg/m^2 over source regions in the Northern Hemisphere. Maximum values
457 reaching 5-10 mg/m^2 are calculated over Northern China. This distribution is very close to the
458 burden calculated by Pringle et al. (2010) but exhibits somewhat lower maximum values. The
459 global mean burden for NH_4^+ is 0.54 mg/m^2 . The total (coarse + fine) nitrate aerosol column
460 shows strong maximum of 5-10 mg/m^2 over Northern and Southern Europe, over India and
461 China and over Africa. A secondary maximum of 3-4 mg/m^2 is also calculated over the central
462 US. This distribution is in agreement with the burden illustrated by Myhre et al. (2006) and
463 Pringle et al. (2010). The global mean total nitrate burden is 1.56 mg/m^2 . Fine nitrate particles

464 associated with anthropogenic emissions contribute to a large extent to the maximum
465 calculated in the central US, in Northern Europe and over the Po Valley, in Northern India
466 and in China. Over Africa, Saudi Arabia, Central Europe and in Northern China, nitrates on
467 dust contribute for more than 4-10 mg/m² to the nitrate column (see Supplementary Material).
468 Over the Mediterranean and in Southern Europe, the contribution of coarse nitrates on dust
469 represents about 50% of the calculated total nitrate column, a proportion in agreement with
470 the measurements by Putaud et al. (2004b). These results are in line with the fine and coarse
471 particles plumes calculated by Fairlie et al. (2010) off the coast of China. The contribution of
472 nitrates on sea-salt is lower and generally close to 0.5 mg/m² over the continents. It only
473 reaches 1 mg/m² in localized areas, in particular off the coast of the Eastern US, or over the
474 Mediterranean where both pollution and sea-salt particle are present. This is somewhat in
475 contrast with Myhre et al. (2006) who calculated a larger and more localized contribution of
476 sea-salt to the total nitrate column over Northern Europe reaching more than 1-1.5 mg/m².
477 The global mean burden of fine mode nitrate is 0.44 mg/m². Nitrates on dust and on sea-salt
478 contribute respectively for 0.65 mg/m² and 0.48 mg/m² to the coarse nitrate global burden.
479 This corresponds to a relative contribution of fine mode nitrates of 28% of the total nitrate
480 burden in this model, to be compared to the 21% calculated by Bauer et al. (2007) and to the
481 23% calculated by Xu and Penner (2012).

482 As discussed in section 2, the formation of fine nitrate particles depends on both the ammonia
483 and nitric acid concentrations. Figure 4 shows the annual mean surface concentration of NH₃
484 and HNO₃. The concentration of ammonia reaches more than 1-2 µg/m³ where agricultural
485 emissions are high, in particular over Northern Europe, in the central United States, in the
486 Ganges valley and in Northern China. In Northern Europe, India, and China, the concentration
487 reaches more than 5 µg/m³. Biomass burning also contributes to higher concentrations in
488 Indonesia, Africa, and South America. This distribution is very much in line with the column
489 density measured by the IASI instrument (Clarisse et al., 2009) and a more detailed and
490 quantitative evaluation of the NH₃ results with the remote sensing data will be presented in
491 forthcoming studies. Nitric acid shows high concentrations of 3-5 µg/m³ in regions of high
492 anthropogenic NO_x emissions. This is in particular the case over the Eastern United States and
493 to a lesser extent in California. In Europe, the concentration reaches 1-2 µg/m³ with a marked
494 maximum over the Mediterranean sea where pollution accumulates. A more detailed
495 evaluation of nitric acid has been provided elsewhere (Hauglustaine et al., 2004; Folberth et
496 al., 2006), although in a model version without a particle formation loss term, which we

497 estimate in budget calculations to be approximately one third, see below. These distributions
498 are in very good agreement with the results shown for instance by Xu and Penner (2012).
499 These calculated surface concentrations of nitrate precursors explain the distribution of fine
500 nitrate particles illustrated in Figure 1 and the region of formation where both NH_3 and HNO_3
501 concentrations are high. As illustrated by Xu et Penner (2012), Figure 5 shows the free
502 ammonia T_A^* to total nitrate T_N ratio. Regions with a negative ratio represent the regions
503 where no excess ammonia is present either due to very low ammonia concentrations or high
504 sulfates concentrations. In these regions all the ammonia is used to neutralize the sulfates and
505 form ammonium sulfate. At the surface these regions are mostly encountered over the ocean
506 or over the deserts and remote continental areas. Due to the short lifetime of ammonia (less
507 than 1 day), these regions expand as altitude increases. In the middle troposphere, only small
508 fine nitrate formation regions persist in convective and biomass burning areas subject to rapid
509 upward transport of emissions. A ratio larger than 1 corresponds to regions where ammonia is
510 abundant and hence the formation of nitrate is limited by the amount of nitric acid available.
511 This condition is mostly met at the surface over regions with high ammonia concentrations, in
512 Northern Europe, the central US, India, China and biomass burning regions. This is also the
513 case over the ocean where natural oceanic NH_3 emissions are present in a low NO_x
514 environment. In other regions ($0 < \text{ratio} < 1$), the formation of nitrate is limited by the amount
515 of ammonia available. These results are in agreement with the findings of Xu and Penner
516 (2012).

517 Table 3 gives the global budget of nitric acid and nitrate particles for both the ‘present-day’
518 (2000) and ‘pre-industrial’ (1850) conditions. A similar budget has been presented by Xu and
519 Penner (2012) and we refer to their study for sake of comparison with our results. It should be
520 mentioned though that Xu and Penner (2012) used a simplified nitrogen chemistry with fixed
521 monthly mean fields of OH and O_3 and without considering the role of organics on gas phase
522 nitrogen chemistry. For the present, we calculate a total source of HNO_3 of 48.5 TgN/yr
523 mostly arising (44.6 TgN/yr) from the gas phase reaction of NO_2 with OH. The heterogeneous
524 formation of HNO_3 from the reaction of N_2O_5 with sulfate aerosols contributes only 3.9
525 TgN/yr (or 8%) nitric acid. This is in contrast to Xu and Penner (2012) who calculated a
526 larger contribution of heterogeneous chemistry of 42%. The reason for this disagreement is
527 unclear. The fact that a simplified nitrogen chemistry not considering the role played by non
528 methane hydrocarbons was used in Xu and Penner (2012), as it was also the case in Bauer et
529 al. (2004), is a possible cause for this difference. It is also unclear which types of aerosols

530 were considered in Xu and Penner (2012) for N_2O_5 hydrolysis. In our model, only the
531 hydrolysis on sulfate aerosols is considered. Also, as pointed out by Evans and Jacob (2005),
532 the impact of N_2O_5 hydrolysis on global chemistry is still uncertain and dependent on the
533 accommodation coefficient used in the models. The accommodation coefficient among the
534 various studies and could also explain this different in HNO_3 heterogenous formation. The
535 total loss of HNO_3 totals 49.5 TgN/yr. The small unbalance between source and loss arises
536 from the stratospheric input of nitric acid into the considered domain for this budget (up to
537 200hPa). Dry and wet deposition contribute about equally (respectively 14.7 and 17.0 TgN/yr)
538 to the total nitric acid deposition loss representing more than 60% of the total HNO_3 loss. The
539 total loss through nitrate formation totals 14.4 TgN/yr. Nitric acid photolysis and reaction
540 with OH contribute for 3.4 TgN/yr. These terms are in line with Xu and Penner (2012) with a
541 larger contribution of dry deposition in LMDz-INCA. The HNO_3 tropospheric burden is 0.3
542 TgN, a value similar to Xu and Penner (2012) and the burden lifetime (burden divided by total
543 loss rate) is 2.25 days in this model to be compared to a burden lifetime of 2.59 days derived
544 from their budget. The source of nitrates (14.4 TgN/yr) is constituted as 22% from the fine
545 mode ammonium nitrate formation and the rest from the formation of coarse nitrates on dust
546 and sea-salt. Most of the nitrate loss is caused by wet deposition (12.7 TgN/yr). We calculate
547 a total nitrate burden of 0.18 TgN with 28% corresponding to the fine mode and the rest as
548 coarse particles on dust and sea-salt. The corresponding lifetime is 4.61 days. The burden of
549 NO_3^- in the troposphere has doubled since the pre-industrial and its lifetime has decreased
550 from 6.75 days in the pre-industrial to its present-day value, reflecting the more efficient
551 scavenging of accumulation mode nitrate particles.

552 Table 4 summarizes the global budget of ammonia and ammonium. The only source of NH_3
553 into the atmosphere is the surface emission totalizing 50.5 TgN/yr for the present-day. The
554 deposition of ammonia arises from dry (11.0 TgN/yr) and wet deposition (21.3 TgN/yr). The
555 formation of ammonium sulfate and ammonium nitrate contributes for 17.5 TgN/yr (35%) to
556 the total loss of NH_3 . The gas phase chemistry oxidation of NH_3 contributes for a negligible
557 amount to its loss. The loss for NH_3 through this oxidation pathway is however a source of
558 N_2O for roughly a similar amount of 0.6 TgN/yr. This number is similar to the estimate by
559 Dentener and Crutzen (1994) and represents about 10% of the anthropogenic source of N_2O
560 as pointed out by these authors. The burden of NH_3 has increased from 0.05 TgN in the pre-
561 industrial to 0.09 TgN for the present-day. The corresponding present-day lifetime of
562 ammonia in the atmosphere is 0.63 days. The only source of NH_4^+ is the ammonium sulfate

563 and ammonium nitrate formation (17.5 TgN/yr). The loss arises mostly from wet deposition
564 (14.9 TgN/yr) and to a lesser extent from surface dry deposition (2.5 TgN/yr). The burden of
565 NH_4^+ is 0.22 TgN with a lifetime of 4.52 days in the atmosphere.

566

567 **3.2 Surface deposition**

568 In Figure 6 we present the total (dry + wet) annual deposition of SO_x ($=\text{SO}_2+\text{SO}_4^-$), NH_x
569 ($=\text{NH}_3+\text{NH}_4^+$), and NO_y ($=\text{NO}+\text{NO}_2+\text{NO}_3+\text{HNO}_2+\text{HNO}_3+\text{HNO}_4+2\text{N}_2\text{O}_5+\text{PAN}+\text{organic}$
570 nitrates+particulate NO_3^-). The three plots show similar patterns with high deposition over
571 Northern America, Europe, India and China. The total SO_x deposition is 107 TgS/yr with wet
572 deposition contributing for 75% to this total. The maximum sulfur deposition reaches 5
573 $\text{gS/m}^2/\text{yr}$ in Northern China. Over Northern America a maximum deposition reaching 1-2
574 $\text{gS/m}^2/\text{yr}$ is calculated over the Eastern United States. In Western Europe, the deposition
575 ranges from 500 $\text{mgS/m}^2/\text{yr}$ in the South to about 2 $\text{gS/m}^2/\text{yr}$ in the North, value reached over
576 the United-Kingdom. A maximum deposition reaching 2 $\text{gS/m}^2/\text{yr}$ is calculated in central
577 Europe. The global NH_x deposition is close to 50 TgN/yr with wet and dry deposition
578 contributing each for 50% to this total (see Table 3). The total ammonia deposition reaches
579 maximum values of 2-3 $\text{gN/m}^2/\text{yr}$ over Northern Europe, Northern India and more than 5
580 $\text{gN/m}^2/\text{yr}$ in China. Over Northern America, a maximum deposition reaching 800 $\text{mgN/m}^2/\text{yr}$
581 is calculated over the central United States. The total oxidized nitrogen deposition totals 50
582 TgN/yr with wet deposition contributing for 60% to this term. Interestingly, total NH_x and
583 total NO_y contribute for the same amount to the global nitrogen deposition to the surface
584 ecosystems. The total NO_y deposition shows a slightly different pattern from the other
585 deposition terms with a maximum reaching 1.5 $\text{gN/m}^2/\text{yr}$ over the Eastern United States,
586 Northern India and China. In Europe the NO_y deposition reaches 800-900 $\text{mgN/m}^2/\text{yr}$. These
587 distributions are in good agreement with the total deposition illustrated by Dentener et al.
588 (2006b) and resulting from the ensemble mean of 23 atmospheric models and with the
589 distributions illustrated by Lamarque et al. (2013) for the ACCMIP simulations.

590 Table 2 summarizes the comparison of the wet deposition of these three terms calculated by
591 the model with the measurements from the EMEP network over Europe, from the NADP
592 network over Northern America and from the EANET network over Eastern Asia (see
593 Supplementary Material for individual plots). The sulfate deposition is slightly
594 underestimated by the model with a Normalized Mean Bias (NMB) of -27% in Europe and -

595 20% in Northern America. In Eastern Asia, a higher underestimation is obtained (NMB=-
596 80%). A similar disagreement in Eastern Asia was also obtained by Dentener et al. (2006b)
597 and by Lamarque et al. (2013) and tentatively attributed to unaccounted sources of SO₂ from
598 coal burning in China. The wet deposition of NH_x is well represented in Europe (NMB=-
599 4.5%) and to a lesser extent in Northern America (NMB=-32%). We note however that the
600 deposition term is again significantly underestimated in Eastern Asia (NMB=-60%). The wet
601 deposition of oxidized nitrogen from HNO₃+NO₃⁻ is relatively well represented in Europe but
602 underestimated by -28%. Over Northern America, a better comparison is obtained
603 (NMB=+13%). Again, in Eastern Asia, a significant underestimate of the wet deposition is
604 obtained (NMB=-54%). Work is underway in order to better understand the reason of the
605 significant underestimate of the deposition terms in Eastern Asia and in particular in China
606 based on new emission inventories generated for this region (Wang et al., 2012).

607

608 **3.3 Aerosol optical properties and radiative forcings**

609 The aerosol optical depth and direct radiative forcings of the various aerosol components are
610 calculated on-line by the General Circulation Model. The solar radiation code in the LMDz
611 GCM consists of an improved version of the parameterizations of Fouquart and Bonnel
612 (1980). The shortwave spectrum is divided into two intervals: 0.25–0.68 μm and 0.68–4.00
613 μm. The model accounts for the diurnal cycle of solar radiation and allows fractional
614 cloudiness to form in a grid box. The radiative fluxes are computed every 2 h, at the top of the
615 atmosphere and at the surface, with and without the presence of clouds. The clear-sky and all-
616 sky direct radiative forcings of the various aerosol components are finally obtained by
617 subtracting the 1850 radiative fluxes from the considered simulation. Since we focus this
618 study on direct aerosol forcings, the cloudiness is not affected by the presence of aerosols in
619 this version of the model.

620 Figure 7 shows the calculated total aerosol optical depth at 550 nm and the optical depth
621 associated with fine and coarse nitrate particles. The total aerosol optical depth (AOD)
622 exhibits values of 0.15-0.25 over the Eastern United States and Europe associated mostly with
623 pollution aerosols. Maximum values reaching more than 0.5 and associated with dust aerosols
624 are calculated over Northern Africa, Arabia, and China. In China, both natural and pollution
625 aerosols contribute to the high aerosol optical depth. Distributions very similar to these results
626 have also been presented in other studies (e.g., Kinne et al., 2006; Bellouin et al., 2011; Xu

627 and Penner, 2012; Shindell et al., 2013). The global mean and total AOD is 0.135 with
628 accumulation mode particules contributing for an AOD of 0.059. As expected from the
629 burden shown in Figure 3, nitrates exhibit higher optical depth over source regions: values of
630 0.02-0.03 over the central United States, and maximum optical depth of 0.05 in northern
631 Europe and more than 0.1 in Northern China. The contribution of nitrates formed from
632 biomass burning emissions is also visible in South America, Africa, and Indonesia with values
633 reaching 0.1 in the later region. The nitrate optical depth is in good agreement with the results
634 presented by Myhre et al. (2006) regarding both the general patterns of the distribution and
635 the calculated values. The global mean and total nitrate optical depth is 0.0053. Fine nitrate
636 particles contribute for 0.0048 to this total number. The evaluation of the calculated total
637 AOD by comparing with the measurements from the AERONET network (Holben et al.,
638 2001, Kinne et al., 2006) is summarized in Table 2 (see Supplementary Material for
639 individual plots). Matching daily data from the model and Aeronet were aggregated to
640 monthly averages. Worldwide, the measured and modeled AOD show a relatively good
641 correlation ($R=0.57$). The arithmetic mean for the measurements of 0.226 is however
642 underestimated by the modeled values of 0.202 with a Normalized Mean Bias (NMB) of -
643 11%. A good agreement with the AERONET measurements is obtained over Northern
644 America. Over this region the model slightly underestimates the measurements (NMB=-4.5%,
645 $R=0.77$). Over Africa, higher AOD associated with dust aerosols are calculated. A fairly good
646 correlation is reached ($R=0.66$) with also a light underestimate by the model of -10%. Over
647 Eastern Asia, the model underestimate the AOD (NMB=-39%). Over Europe, a fairly good
648 correlation between model and measurement is obtained ($R=0.58$). However, over this region,
649 the model overestimates the measurements (NMB=+6%).

650 Figure 8 shows the zonal nitrate column and the corresponding optical depth at 550 nm. This
651 figure illustrates both the fine and coarse mode components for the two variables. The total
652 zonal mean nitrate aerosol column peaks in the northern hemisphere around 25°-50° as shown
653 already in Figure 3. Coarse particles dominate the zonal mean nitrate burden and reach 2.5
654 mg/m^2 . These particles are also responsible for a background column of 0.5-0.8 mg/m^2 in
655 remote areas, associated mainly with coarse nitrate particles on sea-salt. Fine particles
656 associated with pollution present a maximum of about 1 mg/m^2 at 40°N and a secondary
657 maximum of about 0.5 mg/m^2 associated with biomass burning emissions around the equator.
658 The zonal mean nitrate optical depth shows the opposite behavior since coarse particles
659 contribute less efficiently to the Mie scattering. The total zonal mean nitrate optical depth

660 reaches more than 0.012 around 40°N. This optical depth is largely associated with fine
661 particles with coarse nitrates contributing for a maximum optical depth of about 2×10^{-3} .

662 Figure 9 gives the direct radiative forcings of aerosols since pre-industrial times calculated at
663 the top of the atmosphere for all-sky conditions. The forcings are calculated as the difference
664 between the present-day and pre-industrial aerosol distributions. The sulfate radiative forcing
665 is -0.315 W/m^2 in global mean. A value in agreement with the recent intercomparison of
666 models provided in the framework of AeroCom by Myhre et al. (2013) indicating a mean
667 forcing of $-0.32 \pm 0.11 \text{ W/m}^2$ and with the most probable range of -0.18 to -0.44 W/m^2
668 provided by Shindell et al. (2013). The forcing shows values of -2 W/m^2 over regions of high
669 sulfate load over the Eastern United States, Southern Europe and Eastern Asia. The radiative
670 forcing associated with Black Carbon (BC) particles including both the fossil fuel, biofuel and
671 biomass burning components is equal to 0.19 W/m^2 in global mean. Over the Southeastern
672 United States and the United Kingdom, the negative forcing indicates that BC emissions have
673 decreased in these regions since the reference year of 1850 already included emissions from
674 biofuel and to a lesser extent coal burning. The Organic Carbon (OC) forcing is -0.056 W/m^2 .
675 The forcing is negative except in regions where emissions have decreased as mentioned for
676 BC. Myhre et al. (2013) reported a radiative forcing arising from fossil fuel and biofuel of
677 $+0.18 \pm 0.07 \text{ W/m}^2$ for BC and $-0.03 \pm 0.01 \text{ W/m}^2$ for OC, and a combined BC+OC forcing
678 from biomass burning of $-0.00 \pm 0.05 \text{ W/m}^2$. The calculated forcings for BC and OC with this
679 model are in agreement with this compilation and with Shindell et al. (2013). The calculated
680 global mean forcing for nitrate particles is -0.056 W/m^2 . Fine nitrate particules contribute for
681 -0.049 W/m^2 to this forcing and anthropogenic coarse nitrate particulate matter for only -0.006
682 W/m^2 . The total nitrate forcing reaches -2.6 W/m^2 over China, -1.0 W/m^2 over Northern
683 Europe and -0.5 W/m^2 over the central United States. The nitrate forcing also reaches more
684 than -1.0 W/m^2 over biomass burning regions. For this forcing, Myhre et al. (2013) reported a
685 global value of $-0.08 \pm 0.04 \text{ W/m}^2$ and Shindell et al. (2013) a value of $-0.19 \pm 0.18 \text{ W/m}^2$.
686 There is a significant spread in the calculated nitrate forcings from the various model ranging
687 from a value of -0.02 W/m^2 with the OsloCTM2 to -0.12 W/m^2 with the GEOS-CHEM model
688 (Myhre et al., 2013) and even to -0.41 W/m^2 with the GISS model (Shindell et al., 2013). The
689 value calculated with this model is in the range provided by this previous work. Additional
690 work is required to understand the reason of the spread in the various model estimates. In
691 particular, the role played by coarse nitrate formation is important since it subtracts HNO_3

692 from the gas phase decreasing the formation of fine particles of ammonium nitrates and hence
693 reducing the total forcing of nitrates particules.

694

695 **4. Future evolution of nitrate aerosols**

696 In this section, we present the future evolution of nitrate aerosols under the various RCP
697 scenarios for the 2030, 2050 and 2100 periods. The associated direct radiative forcings are
698 presented and the nitrate forcing compared to the forcing of the other particles in order to
699 investigate their relative contribution in the future. Snapshot simulations have been performed
700 for these various cases as described in section 2.3 and the global emissions for key species
701 related to nitrate formation have been presented in Table 1. In order to better understand the
702 contribution of NH_3 , NO_x , and SO_2 emissions to the future nitrate levels, sensitivity
703 simulations have been performed in the particular case of the RCP4.5 scenario for the year
704 2100.

705

706 **4.1 Atmospheric composition**

707 The four RCP scenarios have been simulated with the model but, as far as nitrate particles and
708 their radiative forcing are concerned, and as visible from the total emissions presented in
709 Table 1, two particular scenarios are interesting to compare. In all scenarios, SO_2 and BC
710 emissions decrease from their present day value to their 2100 level. Despite significant
711 differences in 2030 and 2050 (in particular in the case of SO_2 emissions), the level reached in
712 2100 for the four emission scenarios are often close to each other for these species. This is not
713 the case for two important precursors of nitrate particles: ammonia and nitrogen oxides. For
714 NH_3 and NO_x , RCP4.5 and RCP8.5 represent the extremes for emissions in 2100 and are
715 expected to lead to very different nitrate levels in the future. This is in particular the case for
716 NH_3 emissions, which remain close to their present-day level (51 TgN) in 2100 for the
717 RCP4.5 scenario (54 TgN), but increase by 50% in 2100 for RCP8.5 (78 TgN). For NO_x ,
718 emissions decrease from 46 TgN for the present-day to 24 TgN in 2100 for RCP4.5 but
719 decrease only to 31 TgN in 2100 for RCP8.5.

720 As a consequence of these changes in emissions, the concentration of NH_3 varies quite
721 significantly in the future between these two extreme scenarios (see Supplementary Material

722 for additional figures on future changes of the key atmospheric constituents). For surface
723 NH₃ concentrations, for scenario RCP8.5, a significant increase is calculated everywhere in
724 2030 and 2100 except in Indonesia where biomass burning emissions are reduced. In the
725 central United States, Northern and central Europe, India and China, NH₃ increases by up to 2
726 µg/cm³ in 2100 compared to the reference levels illustrated in Figure 4. For the RCP4.5
727 scenario, a significant increase is still predicted in India and in China where emissions are still
728 predicted to rise. However, concentrations are significantly reduced in Western and Eastern
729 Europe by up to 1 µg/cm³ and a lesser increase of 0.5-1 µg/cm³ is calculated in the central US.
730 Due to a reduction in NO_x emissions, HNO₃ has already significantly decreased in 2030 in
731 Northern America and Europe in both scenarios. In contrast, a strong increase is calculated in
732 India and in China reaching more than 2 µg/cm³ in 2030. In 2100, the HNO₃ reduction is
733 almost generalized over the continents with the exception of biomass burning regions in
734 Africa and India in the case of RCP8.5. The concentration of SO₄⁼ increases in India and
735 Southeast Asia by more than 2 µg/cm³ in 2030. As expected from the sharp decrease in SO₂
736 emissions, at the end of the XXIst century, a general decrease of the surface concentration is
737 calculated in 2100, reaching more than 2 µg/cm³ in Northern America, Europe, and China.

738 As a result of these changes in nitrate precursor surface concentrations, nitrate particles are
739 expected to undergo significant variations in the future. Figure 10, shows the evolution of
740 nitrate particles surface concentrations for the various simulations performed and averaged
741 over several regions of the world. As shown earlier (Fig. 1), present-day nitrate concentrations
742 are higher in Europe (1.4 µg/cm³) than in Northern America (0.35 µg/cm³). Due to the
743 decrease in precursors, the concentrations in these two regions decrease for all scenarios
744 during the XXIst century. By 2100, the mean surface concentration in Europe is in the range
745 0.14-0.43 µg/cm³ and in the range 0.03-0.15 µg/cm³ in northern America. In northern and
746 southern Asia, the concentration increases significantly in 2030 and 2050 in scenarios RCP6.0
747 and RCP8.5 reaching 3.6 µg/cm³. By 2100, the surface concentration is in the range 0.38-0.78
748 µg/cm³ and 0.01-0.51 µg/cm³ in northern and southern Asia, respectively. In India, the surface
749 nitrate concentration increases until 2050 in most scenarios, reaching 1.45 µg/cm³ on average.
750 The concentration then decreases and is in the range 0.27-0.65 µg/cm³ in 2100. The
751 concentration of nitrates in other regions (Africa, South America, Australia) show little
752 variation from their present-day value (not shown). The global nitrate concentration increases
753 from 0.38 µg/cm³ for the present to 0.58 µg/cm³ in 2030 and decreases to 0.10-0.21 µg/cm³ in
754 2100.

755 Figure 11 shows the free ammonia (T_A^*) to total nitrate ratio (T_N) for the year 2100 and
756 scenario RCP8.5. There is a significant increase in this ratio at the surface and in the free
757 troposphere compared to the reference simulation (Fig. 5). At the surface, negative ratios
758 indicating the formation of ammonium sulfate instead of ammonium nitrate have vanished
759 over the continents due to a significant and general reduction in SO_4^- concentrations. The
760 ratio has also increased over the continents to values generally larger than 1, indicating an
761 increased excess of ammonia over nitric acid, and a stronger limitation of particle formation
762 by HNO_3 concentrations. This is a direct consequence of lower HNO_3 and higher NH_3
763 concentrations in 2100. Interestingly, in the free troposphere, the T_A^*/T_N ratio becomes
764 positive in the northern hemisphere due to the decreased sulfate concentrations. As a
765 consequence nitrate particles will form at higher altitudes, mostly limited by the amount of
766 NH_3 present at these altitudes.

767 As discussed above, the change in nitrate precursors is responsible for a strong increase of the
768 nitrate column in the northern hemisphere (see Supplementary Material). In both RCP8.5 and
769 RCP4.5 scenarios, the increase in the nitrate column is more than compensated by strong
770 decreases in surface concentrations over Europe and China in 2030 and 2100 (Fig. 10) and
771 over these regions the column decreases by up to 2 mg/m^2 . In the case of RCP4.5, this is also
772 the case over the central US with a decrease of the column reaching 0.4 mg/m^2 . For scenario
773 RCP8.5, in 2100, it is interesting to note that the nitrate column also increases in the southern
774 hemisphere mostly associated with transport from source regions in Africa and South
775 America. Figure 12 and Table 5 present the evolution in the global burden of nitrate particles
776 and its main precursors for the various scenarios and time-slice experiments. In all scenarios,
777 the burden of fine nitrate particles increases in the atmosphere from a present-day value of
778 0.05 TgN to 0.13 TgN for RCP8.5 and 0.07 TgN for RCP4.5. As expected, these two extreme
779 values are mainly driven by the change in NH_3 emissions and burden. The burden of NH_3
780 increases from its present-day value of 0.09 TgN to a maximum value of 0.23 TgN in 2100 in
781 the case of RCP8.5 and to a minimum value of 0.14 TgN for RCP4.5. The formation of coarse
782 nitrate on dust and sea-salt is a result of HNO_3 heterogeneous uptake on these particles. Since
783 no change in climate is considered in these simulations, the burden of dust and sea-salt
784 particles is similar in all simulations. Therefore, the evolution of the coarse nitrate particle
785 burden follows the evolution of the nitric acid in the atmosphere, and decreases from 0.13
786 TgN to $0.09\text{-}0.12 \text{ TgN}$ in 2100. Overall, the burden of total nitrate particles increases from
787 0.181 TgN to 0.183 TgN in 2100 in the case of RCP4.5 and to 0.247 TgN in the case of

788 RCP8.5. The relative contribution of fine particles to this total is however modified and
789 increased from a present-day value 28% to 40% in 2100 for RCP4.5 and to 51% for RCP8.5.
790 Since fine particles contribute the most to the nitrate optical depth and radiative forcing this
791 feature will have consequences on the climate impact of these particles. The future decrease in
792 sulfates leading less ammonium sulfate formation is partially compensated by an increase in
793 ammonia and formation of ammonium nitrate. As a consequence, the NH_4^+ global burden
794 remains fairly constant in time and varies from a present-day value of 0.21 TgN to 0.17-0.24
795 TgN in 2100.

796

797 **4.2 Sensitivity to NH_3 , NO_x , and SO_2 emissions**

798 As discussed earlier, as a direct consequence of future changes in nitrate precursors, scenarios
799 RCP8.5 and RCP4.5 represent the two extremes as far as future nitrates concentrations are
800 concerned. Indeed, SO_2 emissions are close in both scenarios but NO_x and to a larger extent
801 NH_3 emissions are significantly different and at the extremes of their future evolution. Three
802 sensitivity experiments have been performed in order to investigate the relative importance of
803 these emissions on the future nitrate levels. These sensitivity studies have been derived from
804 scenario RCP4.5 for 2100 in order to better understand the role played by SO_2 , NO_x and NH_3
805 emissions on the differences obtained between RCP4.5 and RCP8.5 (see Table 1). Simulation
806 2100 RCP4.5- NO_x has the same emissions as scenario RCP4.5 except that the NO_x emissions
807 are replaced by 2100 RCP8.5 emissions. Similarly in simulation 2100 RCP4.5- NH_3 all
808 emissions are similar to RCP4.5 except that the NH_3 emissions are replaced by 2100 RCP8.5
809 emissions. Finally, in simulation 2100 RCP4.5- SO_2 all emissions are similar to RCP4.5 except
810 that SO_2 emissions are replaced by 2000 emissions. The latter are chosen to come not from
811 the rather similar RCP8.5, and to isolate the impact of sulfates.

812 Figure 12 and Table 5 summarize the impact of these sensitivity simulations on the global
813 burden of nitrates and related species in 2100. When NH_3 emissions are increased to their
814 RCP8.5 level (RCP4.5- NH_3) the burden of NH_3 increases to 0.24 TgN, a value even larger
815 than in scenario RCP8.5. In this case, the fine nitrate burden increases to 0.12 TgN, showing
816 that more than 80% of the difference in fine nitrates between RCP4.5 and RCP8.5 can be
817 explained by the higher NH_3 emissions in scenario RCP8.5. In this case, more ammonium
818 nitrate is formed, and the NH_4^+ burden increases to 0.22 TgN, a value slightly below the
819 RCP8.5 scenario. This can be explained by the fact that less nitric acid is present in RCP4.5

820 compared to RCP8.5 and hence less ammonium nitrate is formed since HNO_3 is the limiting
821 species as seen in Figure 19. Since ammonium sulfates form on preexisting SO_4^- particles,
822 changing the NH_3 emissions has no effect on the sulfates themselves in this sensitivity
823 simulation. The impact of somewhat higher NO_x emissions (simulation RCP4.5- NO_x),
824 increases the nitric acid burden to a value close to their RCP8.5 level. As a result, the fine
825 nitrate burden increases by 0.01 TgN, explaining the remaining difference obtained between
826 RCP4.5 and RCP8.5 scenarios. These sensitivity simulations show that the strong difference
827 calculated in fine nitrate particle levels in 2100 between scenario RCP4.5 and RCP8.5 can be
828 explained mostly (80%) by the higher NH_3 emissions in the case of RCP8.5 and the remaining
829 explained by the higher NO_x emissions. Finally, we illustrate the impact of higher SO_2
830 emissions in the system (simulation RCP4.5- SO_2). In this case, since 2000 emissions have
831 been used, as expected the SO_4^- burden increases to the present-day value. As a consequence,
832 more NH_3 is used to neutralize the sulfates and form ammonium sulfates in priority, and the
833 fine nitrate burden decreases by 0.02 TgN.

834 **4.3 Surface deposition**

835 We have also investigated the evolution of total nitrogen deposition ($\text{NO}_y + \text{NH}_x$ wet and dry
836 deposition) averaged over various regions of the world (see Supplementary Material). In
837 Europe and Northern America, the total N deposition slightly decreases or remains close to its
838 present-day value in the case of scenario RCP8.5. In these regions, the NO_y deposition
839 significantly decreases in the future due to reduced NO_x emissions (from 360 $\text{mgN/m}^2/\text{yr}$ to
840 88-150 $\text{mgN/m}^2/\text{yr}$ in Europe in 2100 and from 265 $\text{mgN/m}^2/\text{yr}$ to 60-108 $\text{mgN/m}^2/\text{yr}$ in
841 Northern America). However, this decrease is largely compensated by an increase in NH_x
842 deposition. In Europe for instance, this term increases from 426 $\text{mgN/m}^2/\text{yr}$ to 672 $\text{mgN/m}^2/\text{yr}$
843 in 2100 for RCP8.5. As a consequence, the fraction of N deposited as NH_x increases from
844 about 50% for the present-day to 70-80% in 2100 in these two regions. In Asia and India, the
845 NO_y deposition generally increases in 2030 or 2050 due to higher NO_x emissions in these
846 regions before decreasing at the end of the XXIst century. In addition, the NH_x deposition
847 generally increases during the course of the century to reach maximum values in 2100. As a
848 result, the total N deposition generally reaches a maximum in 2030-2050 and further increases
849 or remains stable until 2100. In Northern Asia (mostly China) for instance, the total
850 deposition increases from 965 $\text{mgN/m}^2/\text{yr}$ for the present to up to 1443 $\text{mgN/m}^2/\text{yr}$ in 2050
851 before decreasing to 880-1251 $\text{mgN/m}^2/\text{yr}$ in 2100. In India, the deposition increases during
852 the century from a present-day value of 780 $\text{mgN/m}^2/\text{yr}$ to 1100-1700 $\text{mgN/m}^2/\text{yr}$ in 2100. As

853 seen in other regions, this increase in total N deposition is also associated with a new balance
854 between NO_y and NH_x deposition. The fraction of N deposited as NH_x increases from about
855 60% to 80% in these regions. The same tendency is found over oceanic regions and globally.
856 The total N deposited remains fairly stable or slightly decreases in these regions during the
857 XXIst century but the fraction of N deposited as NH_x increases from 45% to 55-70% over the
858 ocean and from 55% to 70-80% globally. This feature has possible strong consequences for
859 terrestrial or oceanic ecosystems because deposition of nitric acid, which dissociates readily in
860 water causes a significant drop in pH, but deposition of NH_x increases the water alkalinity
861 (Doney et al., 2007).

862 **4.4 Anthropogenic aerosol optical depths and radiative forcings**

863 Table 6 gives the anthropogenic aerosol optical depth at 550 nm for the various aerosol
864 components and for the different performed simulations. As in Bellouin et al. (2011), we
865 define the anthropogenic optical depth by subtracting the optical depth calculated in 1850 to
866 the calculated value. The total anthropogenic optical depth decreases in all scenarios from a
867 present-day value of 0.027 to a range of 0.009 for RCP4.5 to 0.016 for RCP6.0 and RCP8.5 in
868 2100. The anthropogenic optical depth of all aerosols decreases from 2000 to 2100 for all
869 scenarios except for nitrates for which the optical depth increases in all RCP storylines. The
870 nitrate optical depth increases from 0.004 in 2000 to a range in 2100 of 0.005 for RCP4.5 to
871 0.009 for RCP8.5. Figure 13 summarizes the contributions of the various aerosol components
872 to this total anthropogenic optical depth. For the present-day, sulfates have the largest
873 contribution of 64%. OC and BC contribute respectively for 19% and 5% to the
874 anthropogenic optical depth. Nitrates have a contribution of 13%. In the future, the
875 contribution of sulfate decreases for all scenarios to a range of 16% in the case of RCP2.6 to
876 36% for RCP4.5 in 2100. The contribution of BC in 2100 ranges from 3% for RCP2.6 to 5%
877 in RCP6.0 and the contribution of OC from 3% in RCP4.5 to 30% in RCP6.0. In all scenarios,
878 we calculate an increasing contribution of nitrates to the anthropogenic aerosol optical depth,
879 and in 2100, nitrates become the dominant contributors to the anthropogenic optical depth.
880 This contribution in 2100 ranges from 46% for RCP6.0 to 64% in RCP2.6.

881 Table 7 gives the all-sky direct radiative forcings since 1850 at the Top Of the Atmosphere
882 (TOA) of the various aerosol components calculated for the different scenarios and time
883 periods. The total forcing decreases from a present-value of -0.23 W/m^2 to -0.11 , -0.07 , -0.11
884 and -0.13 for scenarios RCP2.6, 4.5, 6.0 and 8.5, respectively. The geographical distribution

885 of the total direct forcing for scenario RCP8.5 is shown in Figure 14. In 2000, the forcing is
886 strongly dominated by the negative sulfate forcing in the northern hemisphere with negative
887 values over the continents reaching -6 W/m^2 in China. The positive forcing associated with
888 BC dominates in several areas, in particular in the tropics, in biomass burning regions, or over
889 regions with high surface albedo (see also Fig. 9 for the individual aerosol forcings in 2000).
890 In 2100, the negative total forcing decreases but remains negative over most of the Northern
891 hemisphere. The maximum negative forcings are calculated over the central US where the
892 nitrate forcing is high, over India and China. In these regions, the negative forcing reaches $-$
893 1.6 W/m^2 . The positive forcing also decreases, except over the southeastern United States due
894 to decreasing emissions of OC since 1850.

895 Figure 15 shows the evolution of the radiative forcings associated with the various aerosol
896 components for the different RCP scenarios. As discussed above, the total aerosol forcing
897 decreases from 2000 to 2100 for all scenarios. The negative forcing associated with sulfates
898 decreases from -0.31 W/m^2 in 2000 to a range of -0.03 W/m^2 in RCP 2.6 to -0.08 W/m^2 for
899 RCP8.5. Similarly, the forcing arising from OC decreases from -0.06 W/m^2 in 2000 to -0.03
900 W/m^2 in 2100 for RCP4.5 and to -0.05 W/m^2 for RCP6.0. In addition, the positive forcing
901 associated with BC decreases from 0.19 W/m^2 in 2000 to $0.04\text{-}0.10 \text{ W/m}^2$ in 2100. In contrast,
902 to the other aerosol components, the nitrate negative forcing increases in all scenarios from a
903 present-day value of -0.05 W/m^2 to a value ranging in 2100 from -0.06 W/m^2 for RCP4.5 to $-$
904 0.11 W/m^2 for RCP8.5.

905 Finally, Figure 16 summarizes the impact of nitrates on the future evolution of the
906 anthropogenic AOD at 550nm and on the direct radiative forcing of aerosols at the top of the
907 atmosphere. This figure can be compared to the results shown by Bellouin et al. (2011). As
908 indicated before, the anthropogenic aerosol optical depth generally decreases for all scenarios.
909 Nitrates have an increasing contribution to this AOD and their contribution increases the
910 AOD in 2100 from a factor of 1.8 for RCP6.0 to a factor of 2.8 for RCP2.6. These results are
911 similar to Bellouin et al. (2011) who calculated a ratio for the AOD with and without nitrates
912 of 2 in the case of RCP6.0 and 3.3 in the case of RCP2.6. The total aerosol forcing
913 significantly decreases for all scenarios as a consequence of emission reduction for the main
914 aerosols and aerosol precursors. In contrast, we have seen that the negative nitrate forcing
915 increases in the future for all scenarios due to higher emissions of NH_3 from agriculture.
916 Including nitrates in the radiative forcing calculations significantly increases the total direct
917 forcing of aerosols by a factor of 1.3 in 2000, by a factor of 1.7-2.6 in 2030, by 1.9-4.8 in

918 2050, and by 6.4-8.6 in 2100. These ratios are larger than Bellouin et al. (2011) who included
919 the first indirect effect in the aerosol forcing. These results show that due to increasing NH₃
920 emissions from agriculture in the future, nitrates have the potential to maintain the aerosol
921 forcing at significantly higher values than those expected without including them in the
922 climate simulations and become the main agent contributing to this forcing.

923

924 **5. Conclusion**

925 In this paper, the ammonia cycle and nitrate particle heterogeneous formation have been
926 introduced in the LMDz-INCA global model. The model treats ammonia and nitrates
927 interactively with the full tropospheric chemistry and the other types of aerosols. An
928 important feature of this new model is that both fine nitrate particle formation in the
929 accumulation mode from nitric acid and ammonia reaction and coarse nitrate particles
930 forming on existing dust and sea-salt particles are considered. The model developed in this
931 work reproduces distributions of nitrates and related species in agreement with previous
932 pioneering studies. The present-day surface concentrations of sulfates, nitrates, and
933 ammonium have been evaluated by comparison against network measurements from the
934 EBAS database. In Europe and Northern America, the model captures the sulfates
935 measurements with a mean bias of about 20%. As obtained with other models, ammonium
936 and nitrates particles are more difficult to reproduce and higher biases are obtained, reaching,
937 for nitrates, 60% and 100% over Europe and Northern America, respectively. A positive bias
938 in simulated nitrate aerosol concentrations is suspected to be partly linked to negative
939 sampling artefacts in measurements, because evaporation of ammonium nitrate has been
940 frequently reported to create occasionally losses of up to 50%, in particular in warm weather.
941 Further work is needed to better characterize the individual nitrate measurement error, to see
942 where modeled nitrate is consistent with measurements. The model total sulfate, ammonia,
943 and nitrate deposition have also been compared to network measurements. This evaluation
944 shows a reasonable agreement over Europe and Northern America for these three terms, with
945 mean biases of about 20-30% or better. This is not the case in Eastern Asia where
946 systematically underestimated depositions are calculated. This points to the need to further
947 improve the emission inventories in this region and in China in particular. The calculated total
948 aerosol optical depth distribution is generally well reproduced by the model with a mean bias
949 against the AERONET observations of -11%.

950 The main objective of this work is to investigate the direct radiative forcing of climate of fine
951 and coarse nitrate particles for both present-day and future conditions and investigate their
952 relative contribution to the total aerosol forcing. Fine nitrate particles represent less than 30%
953 of the total nitrate burden. Nitrates contribute for 13% to the anthropogenic AOD since the
954 pre-industrial (1850). The calculated present-day total nitrate direct radiative forcing since the
955 pre-industrial at the top of the atmosphere is -0.056 W/m^2 . Despite their small contribution to
956 the total nitrate burden, fine particles largely dominate the nitrate forcing representing close to
957 90% of this forcing. The present-day nitrate direct radiative forcing has the same magnitude
958 than the forcing associated with organic carbon particles and represent 18% of the sulfate
959 forcing. The nitrate forcing is subject to a significant spread in the previous model estimates.
960 The forcing calculated with this model is within the range of -0.03 to -0.17 W/m^2 reported by
961 Myhre et al. (2013) but in the lower range of this multi-model estimate. We note that both fine
962 and coarse nitrate formation have been included in our calculations. This feature is important
963 since coarse nitrate formation depletes gas phase HNO_3 reducing the formation of fine
964 particles of ammonium nitrate and hence decreasing the total forcing of nitrate particles.

965 The model has been used to investigate the future changes in nitrate concentration and direct
966 radiative forcing of climate based on the four RCP scenarios and for the 2030, 2050 and 2100
967 time horizons. Due to a decrease in fossil fuel emissions in the future, the concentration of
968 most of the species involved in the nitrate-ammonium-sulfate system drop by 2100 under the
969 different scenarios. This is not the case for ammonia which originates from agricultural
970 practices and for which emissions significantly increase in the future. As a consequence, NH_3
971 future concentrations significantly increase in India, in Eastern Asia, and in Northern America
972 for the four scenarios, but also in Europe for the most extreme scenario RCP8.5. Despite this
973 increase in NH_3 surface levels, the surface concentration of nitrates decreases in Europe and
974 Northern America due a significant reduction in NO_x and hence HNO_3 concentration at the
975 surface. In other regions (India, Asia), the nitrate surface concentration generally increases
976 until 2030-2050 due to increasing NO_x and NH_3 and then decrease until 2100. Due to the
977 significant reduction in $\text{SO}_4^{=}$ levels in the future and concomitant increase in NH_3 , large
978 regions of the atmosphere, not only at the surface but also in the free troposphere, shift from
979 an ammonium sulfate to an ammonium nitrate formation regime. As a consequence, despite
980 the decrease of nitrates at the surface level in several regions, the global burden of
981 accumulation mode nitrates in the atmosphere increases by a factor of 1.4-2.6 in 2100
982 depending on the scenario. This range is associated for 80% to the range in future NH_3

983 emissions among the various scenarios with NO_x emissions contributing to the remaining
984 variability between the different scenarios. The total nitrogen ($\text{NH}_x + \text{NO}_y$) deposition
985 generally increases or remains fairly stable in the future for the different scenarios. However
986 this feature is mostly associated with a decrease in NO_y deposition and an increase in NH_x
987 deposition. As a consequence the fraction of nitrogen deposited as NH_x increases from about
988 50% for the present-day to 70-80% by 2100. This feature has possible strong consequences
989 for the environment because as nitric acid causes a significant drop in pH, NH_x in contrast,
990 increases the water alkalinity.

991 The total anthropogenic AOD decreases in all scenarios from a present-day value of 0.027 to
992 a range of 0.009 for RCP4.5 to 0.016 for RCP6.0 and RCP8.5 in 2100. Since all aerosols
993 concentrations decrease in the future except for nitrates, they become the dominant
994 contributors to the anthropogenic AOD. Their contribution increases from 13% for the
995 present-day to 46%-64% in 2100 depending on the considered scenario. The total aerosol
996 direct forcing decreases from its present-day value of -0.23 W/m^2 to -0.07 to -0.13 W/m^2 in
997 2100 based on the considered scenario. As expected from the changes in the AOD, the direct
998 forcing decreases for all aerosols in the future except for nitrates for which the direct negative
999 forcing increases from -0.056 W/m^2 in 2000 to a range of -0.060 to -0.115 W/m^2 in 2100.
1000 Including nitrates in the radiative forcing calculations significantly increases the total direct
1001 forcing of aerosols by a factor of 1.3 in 2000, by a factor of 1.7-2.6 in 2030, by 1.9-4.8 in
1002 2050 and by 6.4-8.6 in 2100. These results indicate and confirm that, due to increasing NH_3
1003 agricultural emissions in the future according to the RCP emission scenarios, nitrates become
1004 the dominant contributor to the anthropogenic aerosol optical depth during the second half of
1005 the XXIst century and significantly increase the calculated aerosol direct forcing.

1006 Agricultural emissions of ammonia are found to play a key role in the future mitigation of
1007 climate change. It is found in this study that ammonium nitrate particles become the dominant
1008 contributor to the future direct forcing of aerosols. In addition, in terms of regional air quality,
1009 we have shown that nitrate levels at the surface are also significantly affected by future
1010 emissions of nitrate precursors with consequences on Particulate Matter levels in Northern
1011 America, Europe and Asia, and hence health impact. The future ammonia emissions also
1012 affect the total nitrogen deposited at the surface with possible consequences on land and
1013 ocean ecosystems. We note however that significant uncertainties remain in our simulations
1014 of future nitrate levels. The ammonium-nitrate-sulfate chemistry module used in this study
1015 has been designed for long-term coupled climate-chemistry simulations and remains relatively

1016 simple compared to the work of Nenes et al. (1998) for instance. This module could be
1017 improved in a future version of the model. We note however, the agreement with previous
1018 studies in terms of simulated distributions or in terms of comparison with measurements. No
1019 particular biases were obtained compared to these previous calculations. Another important
1020 limitation arises from the fact that in this study we analyze the role of future emissions acting
1021 separately on atmospheric composition. The impact of future climate change on nitrate
1022 formation or on dynamical regimes, on future levels of oxidants, on future biogenic emissions
1023 has not been considered. This will be investigated in forthcoming studies along with the
1024 impact of nitrate particles on the aerosol indirect effect. It should also be noted that this study
1025 is based on the RCP scenarios for the future evolution of surface emissions of pollutants. All
1026 RCP scenarios assume aggressive air pollution abatement measures and this assumption is a
1027 major caveat in the projections of future nitrate precursor emissions. In addition, the small
1028 range of possible air pollutant emission trajectories across the RCPs may not necessarily be
1029 representative of the true regional air quality legislation and hence emission pathways. This
1030 type of study needs to be investigated with more realistic emission scenarios for air pollutants
1031 when they become available.

1032 As stressed in this work and previous studies before, nitrate is an increasingly important
1033 aerosol component which impacts climate, air quality, and ecosystems through nitrogen
1034 deposition. Nevertheless, despite this importance for future climate and air quality
1035 projections, and unlike other aerosol components, the simulation of nitrate particles from
1036 global models and their impact on climate has not yet been extensively evaluated. Such an
1037 evaluation in the framework of the AeroCom community effort (Schulz et al., 2006; Myhre et
1038 al., 2013) will be of great interest to better understand the sources of uncertainty on this
1039 aerosol component and is currently underway ([https://wiki.met.no/aerocom/phase3-](https://wiki.met.no/aerocom/phase3-experiments)
1040 [experiments](https://wiki.met.no/aerocom/phase3-experiments)). The results from this exercise will be presented in future AeroCom publications.

1041

1042 **Acknowledgements.**

1043 This study was co-funded by the European Commission under the EU Seventh Research
1044 Framework Programme (ECLAIRE and COMBINE projects), by ADEME under the ACHIA
1045 project and by DGAC under the IMPACT project. D. A. H. is grateful to J.-F. Lamarque for
1046 his assistance with the revised ammonia anthropogenic emissions. We thank A. Cozic for her
1047 continuous support with the LMDz-INCA model development and M. Mendez for his help

1048 with the use of ISORROPIA model. This work was performed using DSM-CCRT resources
1049 under the GENCI (Grand Equipement National de Calcul Intensif) computer time allocation.
1050 We are grateful to the numerous data providers of surface concentrations and deposition in
1051 the various networks (EMEP, NADP, IMPROVE, EANET). Essential is also the provision of
1052 the EBAS database extracts for model evaluation from NILU by Paul Eckhardt, and help from
1053 Jan Griesfeller in preparing these data for the AeroCom tools, which is supported by the EU
1054 ACTRIS project and EMEP.

1055

1056 **References**

- 1057 Ackermann, I. J., H. Hass, M. Memmesheimer, C. Ziegenbein, and A. Ebel, The
1058 parameterization of the sulfate-nitrate-ammonia aerosol system in the long-range transport
1059 model EURAD, *Meteorol. Atmos. Phys.*, 57, 101-114, 1995.
- 1060 Adams, P. J., J. H. Seinfeld, and D. M. Koch, Global concentrations of tropospheric sulfate,
1061 nitrate, and ammonium aerosol simulated in a general circulation model, *J. Geophys. Res.*,
1062 104, 13,791-13,823, 1999.
- 1063 Adams, P. J., J. H. Seinfeld, D. Koch, L. Mickley, and D. Jacob, General circulation model
1064 assessment of direct radiative forcing by the sulfate-nitrate-ammonium-water inorganic
1065 aerosol system, *J. Geophys. Res.*, 106, 1097-1112, doi:10.1029/2000JD900512, 2001.
- 1066 Balkanski, Y., *L'Influence des Aérosols sur le Climat*, Thèse d'Habilitation à Diriger des
1067 Recherches, Université de Versailles Saint-Quentin, Saint-Quentin-en-Yvelines, 2011.
- 1068 Bauer, S. E., Y. Balkanski, M. Schulz, D. A. Hauglustaine, F. Dentener, Global modeling of
1069 heterogeneous chemistry on mineral aerosol surfaces: influence on tropospheric ozone
1070 chemistry and comparison to observations, *J. Geophys. Res.*, 109, D02304,
1071 doi:10.1029/2003JD003868, 2004.
- 1072 Bauer, S. E., D. Koch, N. Unger, S. M. Metzger, D. T. Shindell, and D. G. Streets, Nitrate
1073 aerosols today and in 2030: a global simulation including aerosols and tropospheric ozone,
1074 *Atmos. Chem. Phys.*, 7, 5043-5059, 2007.
- 1075 Bellouin, N., J. Rae, A. Jones, C. Johnson, J. Haywood, and O. Boucher, Aerosol forcing in
1076 the climate model intercomparison project (CMIP5) simulations by the HadGEM2-ES and the
1077 role of ammonium nitrate, *J. Geophys. Res.*, 16, D20206, doi :10.1029/2001JD016074, 2011.
- 1078 Bousquet, P., D. A. Hauglustaine, P. Peylin, C. Carouge, et P. Ciais, Two decades of OH
1079 variability as inferred by an inversion of atmospheric transport and chemistry of methyl
1080 chloroform, *Atmos. Chem. Phys.*, 5, 2635-2656, 2005.
- 1081 Bousquet, P., C. Yver, I. Pison, Y. S. Li, A. Fortems, D. Hauglustaine, S. Szopa, P. J. Rayner,
1082 P. Novelli, R. Langenfelds, P. Steele, M. Ramonet, M. Schmidt, P. Foster, C. Morfopoulos, et
1083 P. Ciais, A 3D synthesis inversion of the molecular hydrogen cycle: sources and sinks budget
1084 implications for the soil uptake, *J. Geophys. res.*, 116, D01302, 2010.

- 1085 Bouwman, A. F., D. S. Lee, W. A. H. Asman, F. J. Dentener, K. W. Van Der Hoek, and J. G.
1086 J. Olivier, A global high-resolution emission inventory for ammonia, *Global Biogeochem.*
1087 *Cycles*, 11, 561-587, 1997.
- 1088 Brunner, D., J. Staehelin, H. L. Rogers, M. O. Köhler, J. A. Pyle, D. A. Hauglustaine, L.
1089 Jourdain, T. K. Berntsen, M. Gauss, I. S. A. Isaksen, E. Meijer, P. van Velthoven, G. Pitari, E.
1090 Mancini, V. Grewe, et R. Sausen, An evaluation of the performance of chemistry transport
1091 models by comparison with research aircraft observations. Part 1: concepts and overall model
1092 performance, *Atmos. Chem. Phys.*, 3, 1606-1631, 2003.
- 1093 Chin, M., P. Ginoux, S. Kinne, B. N. Holben, B. N. Duncan, R. V. Martin, J. A. Logan, A.
1094 Higurashi, and T. Nakajima, Tropospheric Aerosol Optical Thickness from the GOCART
1095 Model and Comparisons with Satellite and Sun Photometer Measurements, *J. Atmos. Sci.*, 59,
1096 461-483, 2002.
- 1097 Chung, S. H. , J. H. Seinfeld, Global distribution and climate forcing of carbonaceous
1098 aerosols, *J. Geophys. Res.*, 107, 4407, 10.1029/2001JD00397, 2002.
- 1099 Claquin, T., Schulz, M., and Balkanski, Y. J., Modeling the mineralogy of atmospheric dust
1100 source. *J. Geophys. Res.*, 104, 22243–22256, 1999.
- 1101 Clarisse, L., C. Clerbaux, F. Dentener, D. Hurtmans, and P.-F. Coheur, Global ammonia
1102 distribution derived from infrared satellite observations, *Nature Geoscience*, 2, 479 – 483,
1103 2009.
- 1104 Cooke, W. F., and J. J. N. Wilson, A global black carbon aerosol model, *J. Geophys. Res.*,
1105 101, 19,395–19,409, 1996.
- 1106 Dall’Osto, M., R. M. Harrison, H. Coe, P. I. Williams, and J. D. Allan, Real time chemical
1107 characterization of local and regional nitrate aerosols, *Atmos. Chem. Phys.*, 9, 3709-3720,
1108 2009.
- 1109 Dentener, F. J., and P. J. Crutzen, Reaction of N₂O₅ on tropospheric aerosols: impact on the
1110 global distributions of NO_x, O₃, and OH, *J. Geophys. Res.*, 98, 7149-7163, 1993.
- 1111 Dentener, F., S. Kinne, T. Bond, O. Boucher, J. Cofala, S. Generoso, P. Ginoux, S. Gong, J.
1112 Hoelzemann, A. Ito, L. Marelli, J. Penner, J.-P. Putaud, C. Textor, M. Schulz, G. v. d. Werf,

1113 and J. Wilson, Emissions of primary aerosol and precursor gases in the years 2000 and 1750 -
1114 prescribed data-sets for AeroCom, *Atmos. Chem. Phys.*, 6, 4321-4344, 2006a.

1115 Dentener, F., , Stevenson, D., Drevet, J., Lamarque, J.-F., Bey, I., Eickhout, B., Fiore, A.,
1116 Hauglustaine, D., Horowitz, L., Krol, M., Kuhlshrestha, U., Lawrence, M., Galy-Lacaux, C.,
1117 Rast, S., Shindell, D., Stevenson, D., Van Noije, T., Atherthon, C., Bell, N., Bergman, D.,
1118 Butler, T., Cofala, J., Collins, W., Doherty, R., Ellingsen, K., Galloway, J., Gauss, M.,
1119 Montanaro, V., Muller, J.-F., Pitari, G., Rodriquez, J., Sanderson, M., Strahan, S., Schultz,
1120 M., Sudo, K., Szopa, S., and Wild, O., Nitrogen and sulfur deposition on regional and global
1121 scales : a multimodel evaluation, *Global Biogeochem. Cycles*, 20, GB4003,
1122 doi:10.1029/2005GB002672, 2006b.

1123 Doney, S. C. N. Mahowald, I. Lima, R. A. Feely, F. T. Mackenzie, J.-F. Lamarque, and P. J.
1124 Rasch, Impact of anthropogenic atmospheric nitrogen and sulfur deposition on ocean
1125 acidification and the inorganic carbon system, *Proc. Natl Acad. Sci.*, 104, 14580–14585,
1126 doi:10.1073/pnas.0702218104, 2007.

1127 Dufour, G., S. Szopa, D. A. Hauglustaine, C. D. Boone, C. P. Rinsland, and P. F. Bernath,
1128 The influence of biogenic emissions on upper-tropospheric methanol as revealed from space,
1129 *Atmos. Chem. Phys.*, 7, 6119-6129, 2007.

1130 Emanuel, K. A., A scheme for representing cumulus convection in large-scale models, *J*
1131 *Atmos. Sci.*, 48, 2313–2335, 1991.

1132 Evans, M. J. and D. J. Jacob, Impact of new laboratory studies of N₂O₅ hydrolysis on global
1133 model budgets of tropospheric nitrogen oxides, ozone, and OH, *Geophys. Res. Lett.*, 32,
1134 L09813, doi:10.1029/2005GL022469, 2005.

1135 Fairlie, T. D., D. J. Jacob, J. E. Dibb, B. Alexander, M. A. Avery, A. van Donkelaar, and L.
1136 Zhang, Impact of mineral dust on nitrate, sulfate, and ozone in transpacific Asian pollution
1137 plumes, *Atmos. Chem. Phys.*, 10, 3999-4012, 2010.

1138 Feng, Y., and J. E. Penner, Global modeling of nitrate and ammonium: interaction of aerosols
1139 and tropospheric chemistry, *J. Geophys. Res.*, 112, D01304, doi:10.1029/2005JD006404,
1140 2007.

1141 Fiore, A. M., Dentener, F. J., Wild, O., Cuvelier, C., Schultz, M. G., Hess, P., Textor, C.,
1142 Schulz, M., Doherty, R. M., Horowitz, L. W., MacKenzie, I. A., Sanderson, M. G., Shindell,

1143 D. T., Stevenson, D. S., Szopa, S., Van Dingenen, R., Zeng, G., Atherton, C., Bergmann, D.,
1144 Bey, I., Carmichael, G., Collins, W. J., Duncan, B. N., Faluvegi, G., Folberth, G., Gauss, M.,
1145 Gong, S., Hauglustaine, D., Holloway, T., Isaksen, I. S. A., Jacob, D. J., Jonson, J. E.,
1146 Kaminski, J. W., Keating, T. J., Lupu, A., Marnmer, E., Montanaro, V., Park, R. J., Pitari, G.,
1147 Pringle, K., J., Pyle, J. A., Schroeder, S., Vivanco, M. G., Wind, P., Wojcik, G., Wu, S., and
1148 Zuber, A, Multi-model Estimates of Intercontinental Source-Receptor Relationships for
1149 Ozone Pollution, *J. Geophys. Res.*, 114, D04301, doi:10.1029/2008JD010816, 2009.

1150 Folberth, G. A., D. A. Hauglustaine, J. Lathière, and F. Brocheton, Interactive chemistry in
1151 the Laboratoire de Météorologie Dynamique general circulation model : model description
1152 and impact analysis of biogenic hydrocarbons on tropospheric chemistry, *Atmos. Chem.*
1153 *Phys.*, 6, 2273–2319, 2006.

1154 Forster, P., V. Ramaswamy, P. Artaxo, T. Berntsen, R. Betts, D.W. Fahey, J. Haywood, J.
1155 Lean, D.C. Lowe, G. Myhre, J. Nganga, R. Prinn, G. Raga, M. Schulz and R. Van Dorland,
1156 2007: Changes in Atmospheric Constituents and in Radiative Forcing. *In: Climate Change*
1157 *2007: The Physical Science Basis. Contribution of Working Group I to the Fourth Assessment*
1158 *Report of the Intergovernmental Panel on Climate Change*, Solomon, S., D. Qin, M.
1159 Manning, Z. Chen, M. Marquis, K.B. Averyt, M. Tignor and H.L. Miller (eds.), Cambridge
1160 University Press, Cambridge, United Kingdom and New York, NY, USA.

1161 Fouquart, Y., and B. Bonel, Computations of solar heating of the earth's atmosphere: a new
1162 parameterization, *Beitr. Phys. Atmos.*, 53, 35-62, 1980.

1163 Gosse, S. F., M. Wang, D. Labrie, and P. Chylek, Imaginary part of the refractive index of
1164 sulfates and nitrates in the 0.7–2.6 μm spectral region, *Appl. Opt.*, 36, 16, 3622–3634, 1997.

1165 Gruber, N., and Galloway, J. N., and Earth-system perspective of the global nitrogen cycle,
1166 *Nature*, 451, 293-296, 2008.

1167 Hauglustaine, D. A., F. Hourdin, S. Walters, L. Jourdain, M.-A. Filiberti, J.-F. Lamarque,
1168 and E. A. Holland, Interactive chemistry in the Laboratoire de Météorologie Dynamique
1169 general circulation model : description and background tropospheric chemistry evaluation, *J.*
1170 *Geophys. Res.*, 109, D04314, doi:10.1029/2003JD003957, 2004.

1171 Heald, C. L., J. L. Collett Jr., T. Lee, K. B. Benedict, F. M. Schwandner, Y. Li, L. Clarisse, D.
1172 R. Hurtmans, M. Van Damme, C. Clerbaux, P.-F. Coheur, S. Philip, R. V. Martin, and H. O.

- 1173 T. Pye, Atmospheric ammonia and particulate inorganic nitrogen over the United States,
1174 *Atmos. Chem. Phys.*, 12, 10295-10312, 2012.
- 1175 Hertel, O., Reis, S., Skjoth, C. A., Bleeker, A., Harrison, R., Cape, J. N., Fowler, D., Skiba,
1176 U., Simpson, D., Jickells, T., Baker, A., Kulmala, M., Gyldenkaerne, S., Sorensen, L. L., and
1177 Erisman, J. W., Nitrogen processes in the atmosphere, in *The European Nitrogen Assessment*,
1178 M. A. Sutton, C. M. Howard, J. W. Erisman, G. Billen, A. Bleeker, P. Grennfelt, H. van
1179 Grinsven, and B. Grizzetti (Eds), pp. 177-207, Cambridge University Press, Cambridge, 2011.
- 1180 Holben, B.N., D.Tanre, A.Smirnov, T.F.Eck, I.Slutsker, N.Abuhassan, W.W.Newcomb,
1181 J.Schafer, B.Chatenet, F.Lavenue, Y.J.Kaufman, J.Vande Castle, A.Setzer, B.Markham,
1182 D.Clark, R.Frouin, R.Halthore, A.Karnieli, N.T.O'Neill, C.Pietras, R.T.Pinker, K.Voss, and
1183 G.Zibordi, An emerging ground-based aerosol climatology: Aerosol Optical Depth from
1184 AERONET, *J. Geophys. Res.*, 106, 12 067-12 097, 2001.
- 1185 Hourdin, F. and A. Armengaud, The use of finite-volume methods for atmospheric advection
1186 of trace species-1. test of various formulations in a general circulation model, *Month. Weather*
1187 *Rev.*, 127, 822-837, 1999
- 1188 Hourdin, F. and J. P. Issartel, Sub-surface nuclear tests monitoring through the CTBT xenon
1189 network, *Geophys. Res. Lett.*, 27, 2245-2248, 2000.
- 1190 Hourdin, F., I. Musat, S. Bony, P. Braconnot, F. Codron, J.-L. Dufresne, L. Fairhead, M.-A.
1191 Filiberti, P. Friedlingstein, J.-Y. Grandpeix, G. Krinner, P. Levan, Z.-X. Li, and F. Lott, The
1192 LMDZ4 general circulation model: climate performance and sensitivity to parametrized
1193 physics with emphasis on tropical convection, *Clim. Dyn.*, 27, 787–813, 2006.
- 1194 Hov, O., A. Eliassen, and D. Simpson, Calculation of the distribution of NO_x compounds in
1195 Europe, in *Tropospheric ozone, regional and global scale interactions*, I. S. A. Isaksen (Ed),
1196 pp. 239-261, Reidel, Dordrecht, 1988.
- 1197 Irshad, R., R. G. Grainger, D. M. Peters, R. A. McPheat, K. M. Smith, and G. Thomas,
1198 Laboratory measurements of the optical properties of sea salt aerosol, *Atmos. Chem. Phys.*, 9,
1199 221–230, 2009
- 1200 Jacobson, M. Z., Global direct radiative forcing due to multicomponent anthropogenic and
1201 natural aerosols, *J. Geophys Res.*, 106, 1551–1568, 2001.

1202 Jacobson, M. Z., Studying the effects of calcium and magnesium on size-distributed nitrate
1203 and ammonium with EQUISOLV II, *Atmos. Environ.*, 33(22), 3635–3649, 1999.

1204 Jarzembski, M. A., M. L. Norman, K. A. Fuller, V. Srivastava, and D. R. Cutten, Complex
1205 refractive index of ammonium nitrate in the 2-20 μm spectral range, *Appl. Opt.*, 42(6), 922-
1206 930, 2003.

1207 Kinne, S, and 43 co-authors, An AEROCOM initial assessment – optical properties in aerosol
1208 component modules of global models, *Atmos. Chem. Phys.*, 6, 1815-1834, 2006.

1209 Krinner, G., N. Viovy, N. de Noblet-Ducoudre, J. Ogee, J. Polcher, P. Friedlingstein, P. Ciais,
1210 S. Sitch, and I. C. Prentice, A dynamic global vegetation model for studies of the coupled
1211 atmosphere-biosphere system, *Global Biogeochem. Cycles*, 19, GB1015, doi:
1212 10.1029/2003GB002199, 2005.

1213 Koffi, B., M. Schulz, F.-M. Breon, J. Griesfeller, D. Winker, Y. Balkanski, S. Bauer, T.
1214 Berntsen, M. Chin, W. D. Collins, F. Dentener, T. Diehl, R. Easter, S. Ghan, P. Ginoux, S.
1215 Gong, L. W. Horowitz, T. Iversen, A. Kirkevåg, D. Koch, M. Krol, G. Myhre, P. Stier, and T.
1216 Takemura, Application of the CALIOP layer product to evaluate the vertical distribution of
1217 aerosols estimated by global models: AeroCom phase I results, *J. Geophys. Res.*, 117,
1218 D10201, doi:10.1029/2011JD016858, 2012.

1219 Lamarque J.-F., T. C. Bond, V. Eyring, C. Granier, A. Heil, Z. Klimont, D. Lee, C. Liousse,
1220 A. Mieville, B. Owen, M. G. Schultz, D. Shindell, S. J. Smith, E. Stehfest, J. Van Aardenne,
1221 O. R. Cooper, M. Kainuma, N. Mahowald, J. R. McConnell, V. Naik, K. Riahi, and D. P. van
1222 Vuuren, Historical (1850–2000) gridded anthropogenic and biomass burning emissions of
1223 reactive gases and aerosols: methodology and application, *Atmos. Chem. Phys.*, 10, 7017-
1224 7039, 2010.

1225 Lamarque, J.-F., G. P. Kyle, M. Meinshausen, K. Riahi, S. J. Smith, D. P. van Vuuren, A. J.
1226 Conley, and F. Vitt, Global and regional evolution of short-lived radiatively-active gases and
1227 aerosols in the Representative Concentration Pathways, *Climatic Change*, 109:191–212 DOI
1228 10.1007/s10584-011-0155-0, 2011.

1229 Lamarque, J.-F., and 25 co-authors, Multi-model mean nitrogen and sulfur deposition from
1230 the Atmospheric Chemistry and Climate Model Intercomparison Project (ACCMIP):

1231 evaluation of historical and projected future changes, *Atmos. Chem. Phys.*, 13, 7997-8018,
1232 2013.

1233 Lathière J., D. A. Hauglustaine, A. D. Friend, N. De Noblet-Ducoudre, N. Viovy, and G. A.
1234 Folberth, Impact of climate variability and land use changes on global biogenic volatile
1235 organic compound emissions, *Atmos. Chem. Phys.*, 6, 2129–2146, 2006.

1236 Lauer, A., J. Hendricks, I. Ackermann, B. Schell, H. Hass, and S. Metzger, Simulating aerosol
1237 microphysics with the ECHAM/MADE GCM – Part I: model description and comparison
1238 with observations, *Atmos. Chem. Phys.*, 5, 3251-3276, 2005.

1239 Law, R. M., Rayner, P. J., Denning, A. S., Erickson, D., Fung, I. Y., Heimann, M., Piper, S.
1240 C., Ramonet, M., Taguchi, S., Taylor, J. A., Trudinger, C. M., and Watterson, I. G.: Variations
1241 in modeled atmospheric transport of carbon dioxide and the consequences for CO₂ inversions,
1242 *Global Biogeochem. Cycles*, 10 (4), 783–796, 1996.

1243 Li, W. J., and L. Y., Shao, Observation of nitrate coatings on atmospheric mineral dust
1244 particles, *Atmos. Chem. Phys.*, 9, 1863-1871, doi:10.5194/acp-9-1863-2009, 2009.

1245 Liao, H., and Seinfeld, J. H., Global impacts of gas-phase chemistry-aerosol interactions on
1246 direct radiative forcing by anthropogenic aerosols and ozone, *J. Geophys. Res.*, 110, D18208,
1247 doi:10.1029/2005JD005907, 2005.

1248 Liao, H., Y. Zhang, W.-T. Chen, F. Raes, and J. H. Seinfeld, Effect of chemistry-aerosol-
1249 climate coupling on predictions of future climate and future levels of tropospheric ozone and
1250 aerosols, *J. Geophys. Res.*, 114, D10306, doi:10.1029/2008JD010984, 2009.

1251 Martin, S. T., J. C. Schlenker, A. Malinowski, H.-M. Hung, and Y. Rudich, Crystallization of
1252 atmospheric sulfate-nitrate-ammonium particles, *Geophys. Res. Lett.*, 30, 2102,
1253 doi:10.1029/2003GL017930, 2003.

1254 Martin, S. T., H.-M. Hung, R. J. Park, D. J. Jacob, R. J. D. Spurr, K. V. Chance, and M. Chin,
1255 Effects of the physical state of tropospheric ammonium-sulfate-nitrate particles on global
1256 aerosol direct radiative forcing, *Atmos. Chem. Phys.*, 4, 183-214, 2004.

1257 Metzger, S., F. Dentener, S. Pandis, and J. Lelieveld, Gas/aerosol partitioning: 1. A
1258 computationally efficient model, *J. Geophys. Res.*, 107, 4312, 10.1029/2001JD001102, 2002a.

1259 Metzger, S., F. Dentener, M. Krol, A. Jeuken, and J. Lelieveld, Gas/aerosol partitioning: 2.
1260 Global modeling results, *J. Geophys. Res.*, 107, 4312, 10.1029/2001JD001103, 2002b.

1261 Mozurkewich, M., The dissociation constant of ammonium nitrate and its dependence on
1262 temperature, relative humidity and particle size, *Atmos. Environ.*, 27A, 261-270, 1993.

1263 Myhre, G., A. Grini, and S. Metzger, Modelling of nitrate and ammonium-containing aerosols
1264 in presence of sea-salt, *Atmos. Chem. Phys.*, 6, 4809-4821, 2006.

1265 Myhre, G., and 40 co-authors, Radiative forcing of the direct aerosol effect from AEROCOM
1266 Phase II simulations, *Atmos. Chem. Phys.*, 13, 1853-1877, 2013.

1267 Nenes, A., S. Pandis, and C. Pilinis, ISORROPIA: a new thermodynamic equilibrium model
1268 for multiphase multicomponent inorganic aerosols, *Aquat. Geochem.*, 4, 123-152, 1998.

1269 Olivier, J. G. J., A. F. Bouwman, K. W. Van der Hoek, and J. J. M. Berdowski, Global air
1270 emission inventories for anthropogenic sources of NO_x, NH₃, and N₂O in 1990,
1271 *Environmental Pollution*, 102, 135-148, 1998.

1272 Park, R. J., D. J. Jacob, B. D. Field, R. M. Yantosca, and M. Chian, Natural and
1273 transboundary pollution influences on sulfate-nitrate-ammonium aerosols in the United States:
1274 implications for policy, *J. Geophys. Res.*, 109, D15204, doi:10.1029/2003JD004473, 2004.

1275 Pilinis, C., and J. H. Seinfeld, Continued development of a general equilibrium model for
1276 inorganic multicomponent atmospheric aerosols, *Atmos. Environ.*, 21(11), 2453–2466, 1987.

1277 Pilinis, C., K. P. Capaldo, A. Nenes, and S. N. Pandis, S. N.: MADM – A new
1278 multicomponent aerosol dynamics model, *Aerosol Sci. Technol.*, 32(5), 482–502, 2000.

1279 Pison, I., P. Bousquet, F. Chevallier, S. Szopa, and D. Hauglustaine, Multi-species inversion
1280 of CH₄, CO and H₂ emissions from surface measurements, *Atmos. Chem. Phys.*, 9, 5281-
1281 5297, 2009.

1282 Pringle, K., J., H. Tost, S. Metzger, B. Steil, D. Giannadaki, A. Nenes, C. Fountoukis, P.
1283 Stier, E. Vignati, and J. Lelieveld, *Geosci. Model Dev.*, 3, 391-412, 2010.

1284 Putaud, J. P., Raes, F., Van Dingenen, R., Brüggemann, E., Facchini, M.-C., Decesari, S.,
1285 Fuzzi, S., Gehrig, R., Hüglin, C., Laj, P., Lorbeer, G., Maenhaut, W., Mihalopoulos, N.,
1286 Müller, K., Querol, X., Rodriguez, S., Schneider, J., Spindler, G., ten Brink, H., Tørseth, K.,

1287 and Wiedensohler, A., European aerosol phenomenology-2: chemical characteristics of
1288 particulate matter at kerbside, urban, rural and background sites in Europe, *Atmos. Environ.*,
1289 38, 2579–2595, 2004a.

1290 Putaud, J.-P., R. Van Dingenen, A. Dell'Acqua, F. Raes, E. Matta, S. Decesari, M. C.
1291 Facchini, and S. Fuzzi, Size-segregated aerosol mass closure and chemical composition in
1292 Monte Cimone (I) during MINATROC, *Atmos. Chem. Phys.*, 4, 889-902, doi:10.5194/acp-4-
1293 889-2004, 2004b.

1294 Reidmiller, D. R., Fiore, A. M., Jaffe, D. A., Bergmann, D., Cuvelier, C., Dentener, F. J.,
1295 Duncan, B. N., Folberth, G., Gauss, M., Gong, S., Hess, P., Jonson, J. E., Keating, T., Lupu,
1296 A., Marmer, E., Park, R., Schultz, M. G., Shindell, D. T., Szopa, S., Vivanco, M. G., Wild,
1297 O., and Zuber, A., The influence of foreign vs. North American emissions on surface ozone in
1298 the US, *Atmos. Chem. Phys.*, 9, 5027-5042, 2009.

1299 Rivier, L., P. Ciais, D. A. Hauglustaine, P. Bakwin, P. Bousquet, P. Peylin, et A. Klonecki,
1300 Evaluation of SF₆, C₂Cl₄, and CO to approximate fossil fuel CO₂ in the Northern
1301 Hemisphere using a chemistry transport model, *J. Geophys. Res.*, 111, D16311, 2006.

1302 Sander, S. P., J. Abbatt, J. R. Barker, J. B. Burkholder, R. R. Friedl, D. M. Golden, R. E.
1303 Huie, C. E. Kolb, M. J. Kurylo, G. K. Moortgat, V. L. Orkin, and P. H. Wine, *Chemical*
1304 *Kinetics and Photochemical Data for Use in Atmospheric Studies*, Evaluation No. 17, JPL
1305 Publication 10-6, Jet Propulsion Laboratory, Pasadena, 2011.

1306 Schaap, M., van Loon, M., ten Brink, H. M., Dentener, F. J., and Builtjes, P. J. H., Secondary
1307 inorganic aerosol simulations for Europe with special attention to nitrate, *Atmos. Chem. Phys.*,
1308 4, 857–874, doi:10.5194/acp-4-857-2004, 2004.

1309 Schulz, M., *Constraining Model Estimates of the Aerosol Radiative Forcing*, Thèse
1310 d'Habilitation à Diriger des Recherches, Université Pierre et Marie Curie, Paris VI, 2007.

1311 Schulz, M., Y. Balkanski, F. Dulac, and W. Guelle, Role of aerosol size distribution and
1312 source location in a three-dimensional simulation of a Saharan dust episode tested against
1313 satellite-derived optical thickness, *J. Geophys. Res.*, 103, 10,579–10,592, 1998.

1314 Schulz, M., C. Textor, S. Kinne, Y. Balkanski, S. Bauer, T. Berntsen, T. Berglen, O. Boucher,
1315 F. Dentener, A. Grini, S. Guibert, T. Iversen, D. Koch, A. Kirkevåg, X. Liu, V. Montanaro, G.
1316 Myhre, J. Penner, G. Pitari, S. Reddy, Ø. Seland, P. Stier, and T. Takemura, Radiative forcing

1317 by aerosols as derived from the AeroCom present-day and pre-industrial simulations, *Atmos.*
1318 *Chem. Phys.*, 6, 5225-5246, 2006.

1319 Schulz M., Gauss, M., Benedictow, A., Jonson, J. E., Tsyro, S., Nyiri, A., Simpson, D.,
1320 Steensen, B. M., Klein, H., Valdebenito, 5 A., Wind, P., Kirkevåg, A., Griesfeller, J.,
1321 Bartnicki, J., Olivie, D., Grini, A., Iversen, T., Seland, Ø., Semeena, V. S., Fagerli, H., Aas,
1322 W., Hjellbrekke, A.-G., Mareckova, K., Wankmuller, R., Schneider, P., Solberg, S., Svendby,
1323 T., Liu, L., Posch, M., Vieno, M., Reis, S., Kryza, M., Werner, M., and Walaszek, K,
1324 *Transboundary acidification, eutrophication and ground level ozone in Europe in 2011*,
1325 EMEP Report 1/2013, Norwegian Meteorological Institute, ISSN 1504-6109, 2013.

1326 Schwartz, S. E., Mass transport considerations pertinent to aqueous-phase reactions of gases
1327 in liquid-water clouds, in *Chemistry of Multiphase Atmospheric Systems*, edited by W.
1328 Jaeschke, pp. 415-471, Springer, New York, 1986.

1329 Seinfeld, J. H., and S. N. Pandis, *Atmospheric chemistry and Physics*, John Wiley and Sons,
1330 New York, 1998.

1331 Shindell, D. T., Lamarque, J.-F., Schulz, M., Flanner, M., Jiao, C., Chin, M., Young, P. J.,
1332 Lee, Y. H., Rotstajn, L., Mahowald, N., Milly, G., Faluvegi, G., Balkanski, Y., Collins, W. J.,
1333 Conley, A. J., Dalsoren, S., Easter, R., Ghan, S., Horowitz, L., Liu, X., Myhre, G.,
1334 Nagashima, T., Naik, V., Rumbold, S. T., Skeie, R., Sudo, K., Szopa, S., Takemura, T.,
1335 Voulgarakis, A., Yoon, J.-H., and Lo, F.: Radiative forcing in the ACCMIP historical and
1336 future climate simulations, *Atmos. Chem. Phys.*, 13, 2939-2974, doi:10.5194/acp-13-2939-
1337 2013, 2013.

1338 Sun, Q. and Wexler, A. S., Modeling urban and regional aerosols near acid neutrality
1339 application to the 24-25 June SCAQS episode, *Atmos. Environ.*, 32, 3533–3545, 1998.

1340 Sutton, M. A., Dragosits, U., Tang, Y. S. and Fowler, D., Ammonia emissions from non-
1341 agricultural sources in the UK, *Atmos. Environ.*, **34**, 855 -869, 2000.

1342 Szopa, S., Balkanski, M., Schulz, S., Bekki, D., Cugnet, A., Fortems-Cheiney, S., Turquety, A.,
1343 Cozic, C., Deandreis, D., Hauglustaine, A., Idelkadi, J., Lathiere, M., Marchand, N., Yan, and J.-
1344 L. Dufresne, Aerosol and ozone changes as forcing for climate evolution between 1850 and
1345 2100, *Clim. Dyn.*, 40, 2223–2250, DOI 10.1007/s00382-012-1408-y, 2012.

1346 Tang, I. N., Chemical and size effects of hygroscopic aerosols on light scattering coefficients,
1347 *J. Geophys. Res.*, 101, D14, 2156-2202, doi:10.1029/96JD03003, 1996.

1348 Tie, X., S. Madronich, S. Walters, D. P. Edwards, P. Ginoux, N. Mahowald, R. Y. Zhang, C.
1349 Lou, and G. Brasseur, Assessment of the global impact of aerosols on tropospheric oxidants,
1350 *J. Geophys. Res.*, 110, D03204, doi:10.1029/2004JD005359, 2005.

1351 van Dorland, R., Dentener, F. J., and Lelieveld, J., Radiative forcing due to tropospheric
1352 ozone and sulphate aerosols, *J. Geophys. Res.*, 102, 28079–28100, 1997.

1353 Van Leer, B., Towards the ultimate conservative difference scheme. Part IV: a new approach
1354 to numerical convection, *J. Comput. Phys.*, 23, 276-299, 1977.

1355 Wang, R., S. Tao, W. Wang, J. Liu, H. Shen, G. Shen, B. Wang, X. Liu, W. Li, Y. Huang, Y.
1356 Zhang, Y. Lu, H. Chen, Y. Chen, C. Wang, D. Zhu, X. Wang, B. Li, W. Liu, J. Ma., Black
1357 carbon emissions in China from 1949 to 2050, *Environmental Science & Technology*, 46,
1358 7595-7603, 2012.

1359 Xu, L., and J. E. Penner, Global simulations of nitrate and ammonium aerosols and their
1360 radiative effects, *Atmos. Chem. Phys.*, 12, 9479-9504, 2012.

1361 Zhang, L., D. J. Jacob, E. M. Knipping, N. Kumar, J. W. Munger, C. C. Carouge, A. van
1362 Donkelaar, Y. X. Wang, and D. Chen, Nitrogen deposition to the United States: distributions,
1363 sources, and processes, *Atmos. Chem. Phys.*, 12, 4539-4554, 2012.

1364 Zhang, Y., Seigneur, C., Seinfeld, J. H., Jacobson, M., Clegg, S. L., and Binkowski, F. S., A
1365 comparative review of inorganic aerosol thermodynamic equilibrium modules: similarities,
1366 differences, and their likely causes, *Atmos. Environ.*, 34(1), 117–137, 2000.

1367

1368 Table 1. Total (anthropogenic + natural) and global emissions of NO_x and NH₃ (TgN/yr), SO₂
 1369 (TgS/yr), Black Carbon (BC) and Organic Carbon (OC) (Tg/yr) for the various simulations
 1370 performed in this study.

Scenario	NO _x	NH ₃	SO ₂	BC	OC
1850	10	21	10	3	22
2000	46	50	59	8	36
2030 RCP2.6	39	62	35	7	36
2050 RCP2.6	36	67	22	5	30
2100 RCP2.6	24	79	14	3	25
2030 RCP4.5	42	56	49	7	29
2050 RCP4.5	36	57	32	6	27
2100 RCP4.5	24	54	18	4	19
2030 RCP6.0	40	57	45	7	36
2050 RCP6.0	37	64	43	7	36
2100 RCP6.0	23	72	17	4	32
2030 RCP8.5	48	63	48	7	33
2050 RCP8.5	40	69	32	6	30
2100 RCP8.5	31	78	20	4	24
<i>Sensitivity simulations</i>					
2100 RCP4.5-NO _x	31	54	18	4	19
2100 RCP4.5-NH ₃	24	78	18	4	19
2100 RCP4.5-SO ₂	24	54	59	4	19

1371

1372 Table 2. Normalized mean bias (NMB, %) and correlation coefficient (R) of model results
 1373 versus EBAS measurements for the year 2006 and for various regions and for the world for
 1374 surface concentration of SO₄, NH₄ and NO₃, wet deposition of SO_x, NH_x and NO_y and
 1375 simulated total aerosol optical depth at 550 nm compared to AERONET data.

1376

		Europe	Northern America	Eastern Asia	Northern Africa	World
<i>Concentrations (ugS-N/m³)</i>						
SO ₄	<i>NMB</i>	20%	21%	N.A.	N.A.	20%
	<i>R</i>	0.58	0.68			0.66
NH ₄	<i>NMB</i>	62%	-16%	N.A.	N.A.	50%
	<i>R</i>	0.43	0.77			0.51
NO ₃	<i>NMB</i>	64%	115%	N.A.	N.A.	68%
	<i>R</i>	0.43	0.54			0.59
<i>Wet deposition (gS-N/m²/y)</i>						
SO ₄	<i>NMB</i>	-27%	-20%	-80%	N.A.	-59%
	<i>R</i>	0.47	0.70	0.60		0.31
NH _x	<i>NMB</i>	-4.5%	-32%	-60%	N.A.	-34%
	<i>R</i>	0.33	0.46	0.42		0.24
NO _y	<i>NMB</i>	-28%	13%	-54%	N.A.	-40%
	<i>R</i>	0.49	0.73	0.24		0.19
<i>Total Aerosol Optical Depth</i>						
AOD	<i>NMB</i>	6%	-4.5%	-10%	-39%	-11%
	<i>R</i>	0.58	0.77	0.66	0.64	0.57

1377

1378

1379 Table 3. Tropospheric budget of nitric acid (HNO₃) and nitrate particles (NO₃⁻) for the ‘pre-
 1380 industrial’ (1850) and ‘present-day’ (2000) simulations. The budget terms for HNO₃ are
 1381 integrated up to 200 hPa.

	1850	2000
<i>HNO₃</i>		
Sources (TgN/yr)	14.09	48.51
Gas phase	14.04	44.59
Aerosols	0.05	3.92
Loss (TgN/yr)	14.80	49.46
Gas phase	1.55	3.42
Fine nitrates	0.28	3.19
Dust nitrates	2.96	6.26
Sea-salt nitrates	1.57	4.92
Dry deposition	3.42	14.66
Wet deposition	5.02	17.02
Burden (TgN)	0.14	0.30
Lifetime (days)	3.57	2.25
<i>NO₃⁻</i>		
Sources (TgN/yr)	4.81	14.37
Fine	0.28	3.19
Dust	2.96	6.26
Sea-salt	1.57	4.92
Loss (TgN/yr)	4.80	14.33
Dry deposition	0.32	1.66
Wet deposition	4.49	12.67
Burden (TgN)	0.09	0.18
Fine	0.01	0.05
Dust	0.04	0.07
Sea-salt	0.03	0.06
Lifetime (days)	6.75	4.61

1382 Table 4. Tropospheric budget of ammonia (NH_3) and ammonium particles (NH_4^+) for the ‘pre-
 1383 industrial’ (1850) and ‘present-day’ (2000) simulations.

	1850	2000
<i>NH₃</i>		
Sources : emissions (TgN/yr)	20.99	50.51
Loss (TgN/yr)	20.98	50.47
Gas phase	0.28	0.63
Ammonium formation	5.14	17.46
Dry deposition	9.67	21.33
Wet deposition	5.89	11.05
Burden (TgN)	0.05	0.09
Lifetime (days)	0.81	0.63
<i>NH₄⁺</i>		
Sources : ammonia conversion (TgN/yr)	5.14	17.46
Loss (TgN/yr)	5.13	17.42
Dry deposition	0.32	2.50
Wet deposition	4.81	14.91
Burden (TgN)	0.08	0.22
Lifetime (days)	5.39	4.52

1384

1385 Table 5. Evolution of the tropospheric burdens of gaseous and particulate species for the
 1386 various simulations performed in this study. Units: TgN, except SO₄²⁻ (TgS).

Scenario	HNO ₃	NH ₃	NH ₄ ⁺	SO ₄ ²⁻	Fine NO ₃ ⁻	Coarse NO ₃ ⁻
1850	0.14	0.05	0.08	0.19	0.01	0.08
2000	0.30	0.09	0.21	0.42	0.05	0.13
2030 RCP2.6	0.25	0.14	0.23	0.33	0.09	0.12
2050 RCP2.6	0.24	0.17	0.22	0.27	0.11	0.12
2100 RCP2.6	0.16	0.26	0.21	0.22	0.12	0.09
2030 RCP4.5	0.28	0.11	0.23	0.39	0.07	0.13
2050 RCP4.5	0.26	0.13	0.21	0.31	0.08	0.12
2100 RCP4.5	0.24	0.14	0.17	0.24	0.07	0.11
2030 RCP6.0	0.28	0.11	0.22	0.37	0.07	0.12
2050 RCP6.0	0.27	0.14	0.24	0.36	0.09	0.12
2100 RCP6.0	0.19	0.21	0.21	0.24	0.11	0.10
2030 RCP8.5	0.32	0.12	0.25	0.39	0.09	0.14
2050 RCP8.5	0.28	0.16	0.24	0.32	0.11	0.13
2100 RCP8.5	0.27	0.23	0.24	0.25	0.13	0.12
<i>Sensitivity simulations</i>						
2100 RCP4.5-NO _x	0.27	0.14	0.18	0.24	0.08	0.12
2100 RCP4.5-NH ₃	0.21	0.24	0.22	0.24	0.12	0.10
2100 RCP4.5-SO ₂	0.26	0.12	0.21	0.42	0.05	0.11

1387

1388 Table 6. Aerosol Optical Depth (AOD) at 550 nm (X 1000) for 1850 and 2000 and
 1389 anthropogenic AOD (X 1000) for the various simulations performed in this study. The
 1390 anthropogenic AOD is calculated by subtracting the 1850 AOD to the considered scenario.

Scenario	NO ₃ ⁻	SO ₄ ⁼	OC	BC	Total
<i>Aerosol Optical Depth</i>					
1850	1.70	14.70	13.67	1.14	31.18
2000	5.27	32.18	18.77	2.45	58.67
<i>Anthropogenic Aerosol Optical Depth</i>					
2000	3.57	17.51	5.09	1.31	27.49
2030 RCP2.6	7.41	9.92	5.42	1.49	24.23
2050 RCP2.6	8.19	5.15	3.55	0.87	17.76
2100 RCP2.6	8.02	2.03	2.10	0.35	12.49
2030 RCP4.5	5.55	14.59	2.93	1.51	24.58
2050 RCP4.5	6.20	8.42	2.52	1.23	18.38
2100 RCP4.5	5.26	3.36	0.31	0.43	9.36
2030 RCP6.0	5.77	13.08	4.96	1.53	25.35
2050 RCP6.0	7.00	12.40	5.34	1.46	26.20
2100 RCP6.0	7.57	3.15	4.84	0.79	16.35
2030 RCP8.5	7.39	14.57	4.48	1.46	27.89
2050 RCP8.5	8.63	8.94	3.31	1.11	21.99
2100 RCP8.5	9.57	4.20	1.75	0.66	16.17

1391

1392 Table 7. All-sky direct radiative forcing at the Top of the Atmosphere (TOA) of the various
 1393 aerosol components since the 1850 period and future evolution under the different scenarios
 1394 considered in this study (mW/m^2).

Scenario	NO_3^-	SO_4^{2-}	OC	BC	Total
2000	-56	-315	-56	194	-234
2030 RCP2.6	-95	-118	-60	182	-153
2050 RCP2.6	-102	-94	-39	107	-130
2100 RCP2.6	-96	-33	-25	40	-113
2030 RCP4.5	-76	-270	-29	187	-189
2050 RCP4.5	-78	-159	-25	152	-110
2100 RCP4.5	-60	-60	-3	53	-70
2030 RCP6.0	-79	-235	-57	187	-184
2050 RCP6.0	-94	-225	-59	180	-198
2100 RCP6.0	-91	-58	-55	98	-106
2030 RCP8.5	-101	-273	-49	181	-241
2050 RCP8.5	-108	-173	-40	138	-184
2100 RCP8.5	-115	-79	-18	82	-130

1395

1396 **Figure Captions**

1397

1398 Figure 1. Annual mean surface concentration of (top) sulfate aerosols, (middle) ammonium
1399 aerosols, and (bottom) total nitrate aerosols simulated for present-day conditions ($\mu\text{g}/\text{m}^3$).

1400

1401 Figure 2. Annual mean surface concentration of (top) fine mode nitrate aerosols, (middle)
1402 coarse mode nitrates on dust, and (bottom) coarse mode nitrates on sea-salt simulated for
1403 present-day conditions ($\mu\text{g}/\text{m}^3$).

1404

1405 Figure 3. Annual mean tropospheric column of (top) sulfate aerosols, (middle) ammonium
1406 aerosols, and (bottom) total nitrate aerosols simulated for present-day conditions (mg/m^2).

1407

1408 Figure 4. Annual mean surface concentration of (top) ammonia, and (bottom) nitric acid
1409 simulated for present-day conditions ($\mu\text{g}/\text{m}^3$).

1410

1411 Figure 5. Annual mean free ammonia to total nitrate ratio calculated for present-day
1412 conditions at the surface, 900 hPa, 700 hPa, and 500 hPa.

1413

1414 Figure 6. Annual mean SO_x ($\text{mgS}/\text{m}^2/\text{yr}$), NH_x , and NO_y ($\text{mgN}/\text{m}^2/\text{yr}$) total surface deposition
1415 calculated for present-day conditions.

1416

1417 Figure 7. Annual mean total aerosol optical depth at 550 nm (top), and nitrate aerosol optical
1418 depth (bottom) simulated for present-day conditions.

1419

1420 Figure 8. (a) zonal and annual mean total (solid line), coarse mode (dashed line) and fine
1421 mode (dotted line) nitrate particles column (mg/m^2); (b) corresponding total, coarse, and fine
1422 nitrate particles optical depth at 550 nm ($\times 100$).

1423

1424 Figure 9. All-sky top of the atmosphere direct radiative forcing of sulfates, nitrates, organic
1425 carbon, and black carbon particles (W/m^2) calculated for present-day conditions.

1426

1427 Figure 10. Evolution of the nitrate surface concentration ($\mu\text{g}/\text{m}^3$) for scenario RCP8.5 (red),
1428 RCP6.0 (yellow), RCP4.5 (green) and RCP2.6 (blue) between the present-day and 2100. The
1429 averaged surface concentration is depicted for Europe, Northern America, Northern Asia,
1430 Southern Asia, India, and the globe.

1431

1432 Figure 11. Annual mean free ammonia to total nitrate ratio calculated for 2100 RCP8.5
1433 conditions at the surface, 900 hPa, 700 hPa, and 500 hPa.

1434

1435 Figure 12. Evolution of the global burden of fine mode nitrates, coarse mode nitrates,
1436 ammonia, ammonium, nitric acid (TgN), and sulfates (TgS) for scenario RCP8.5 (red),
1437 RCP6.0 (yellow), RCP4.5 (green) and RCP2.6 (blue) between present-day and 2100. The
1438 dashed green line refers to the sensitivity scenario RCP4.5-NH₃, the dotted green line to
1439 scenario RCP4.5-NO_x, and the dotted-dashed green line to scenario RCP4.5-SO₂.

1440

1441 Figure 13. Evolution of the contribution (%) of nitrates (yellow), sulfates (green), organic
1442 carbon (blue), and black carbon (red) to the total aerosol anthropogenic optical depth at 550
1443 nm for the four RCP scenarios and from the present-day to 2100.

1444

1445 Figure 14. All-sky top of the atmosphere total direct aerosol radiative forcing (W/m^2)
1446 calculated for the present-day and for 2030, 2050, and 2100 under scenario RCP8.5.

1447

1448 Figure 15. All-sky top of the atmosphere direct radiative forcing (W/m^2) of nitrates (yellow),
1449 sulfates (green), organic carbon (blue), and black carbon (red) calculated for the four RCP
1450 scenarios and from the present-day to 2100.

1451

1452 Figure 16. Evolution of A/ the aerosol anthropogenic optical depth at 550nm (X1000) and B/
1453 all-sky top of the atmosphere direct radiative forcing (W/m^2) for the four RCP scenarios and
1454 from present-day to 2100; RCP8.5 (red), RCP6.0 (yellow), RCP4.5 (green) and RCP2.6 (blue)
1455 Solids lines: nitrates included; dashed lines: nitrates excluded. Corresponding fractional
1456 contribution of nitrates to the C/ anthropogenic aerosol optical depth and D/ direct radiative
1457 forcing.

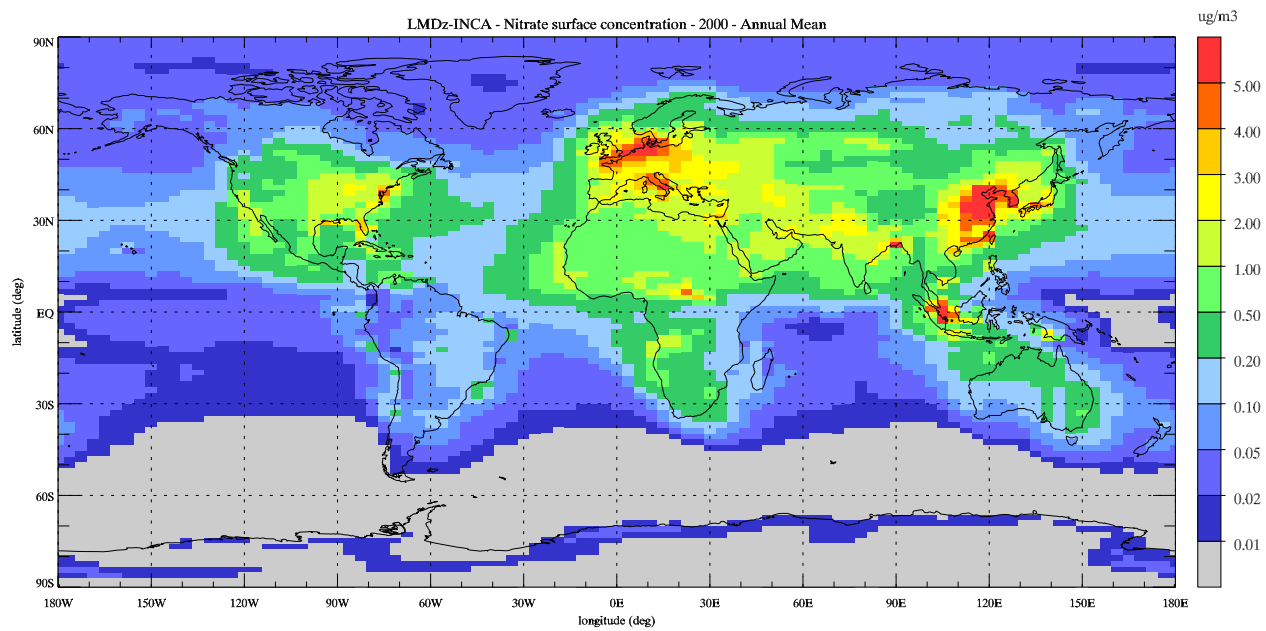
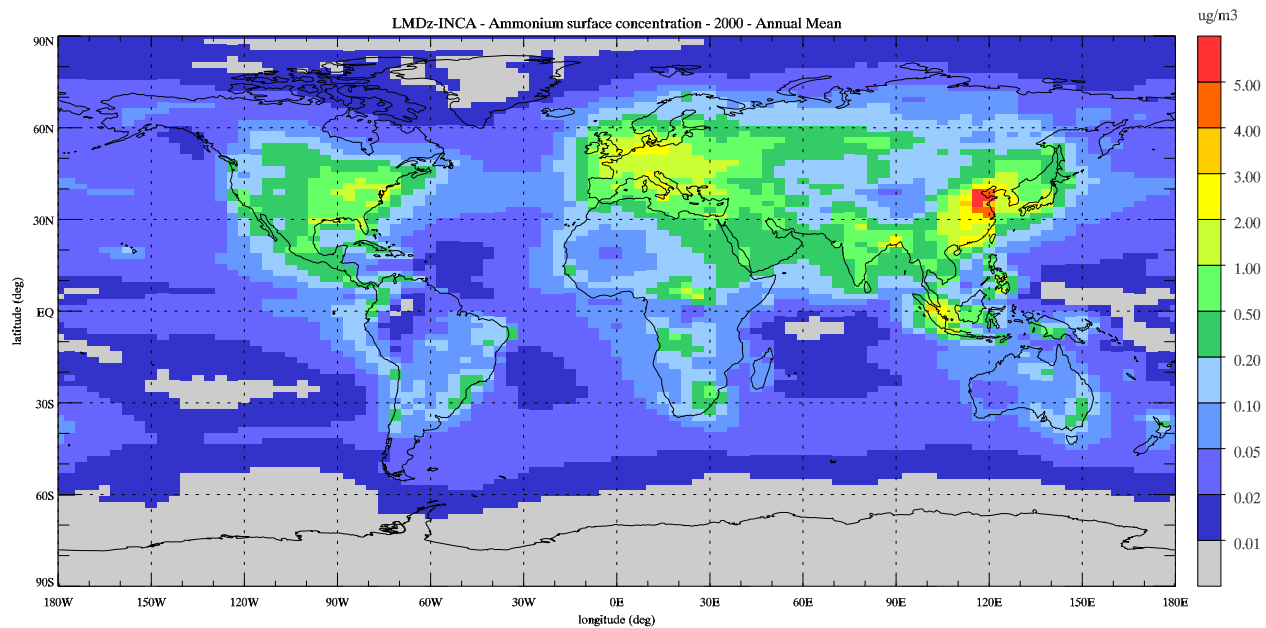
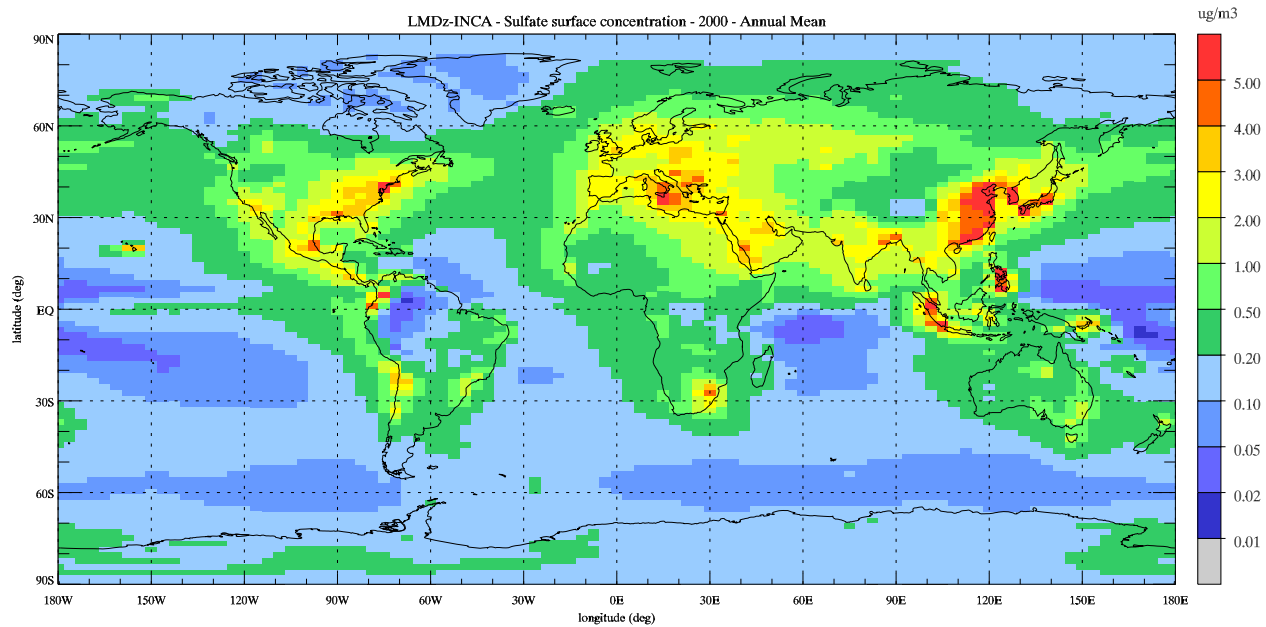


Figure 1

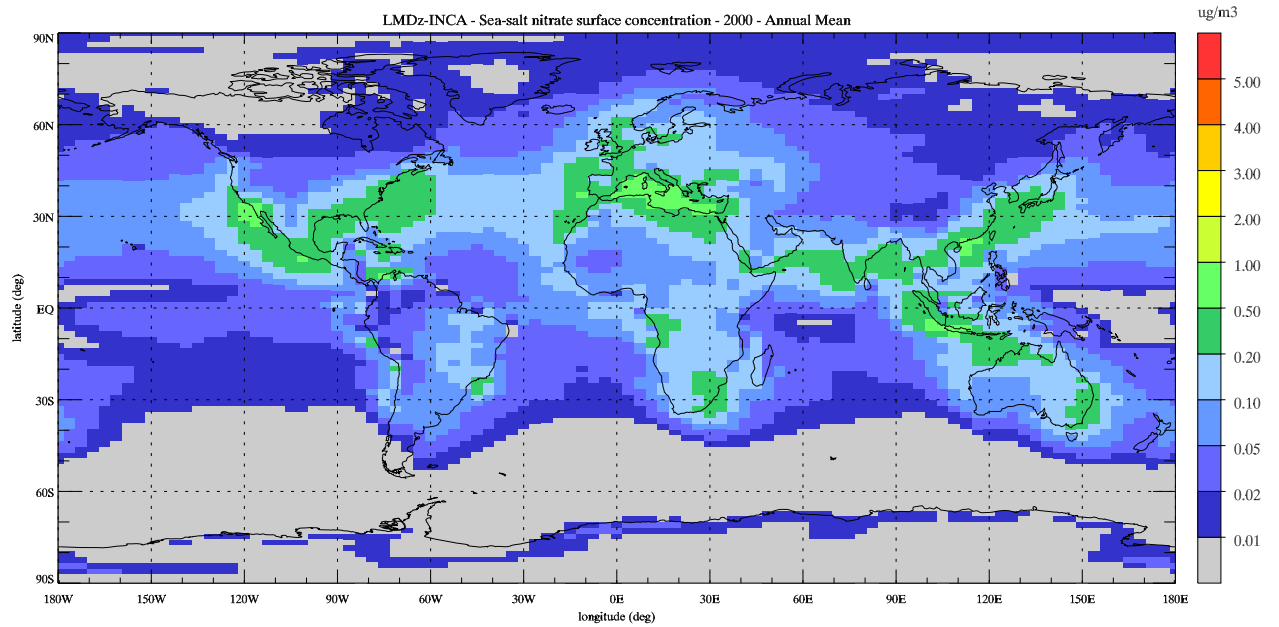
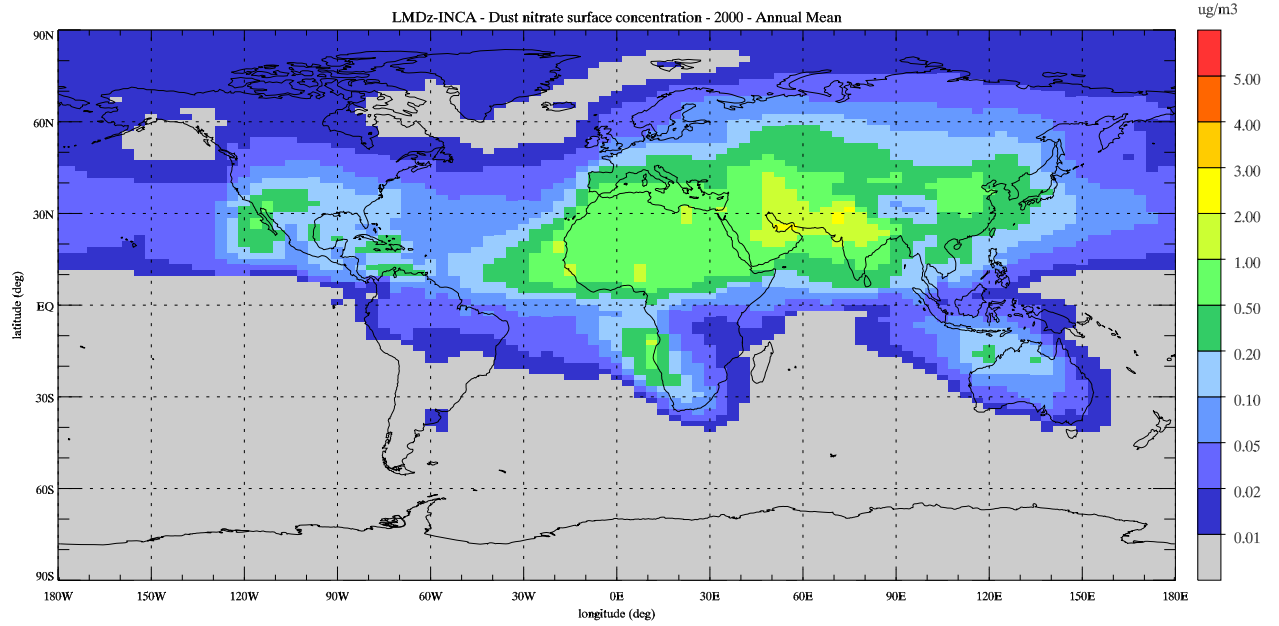
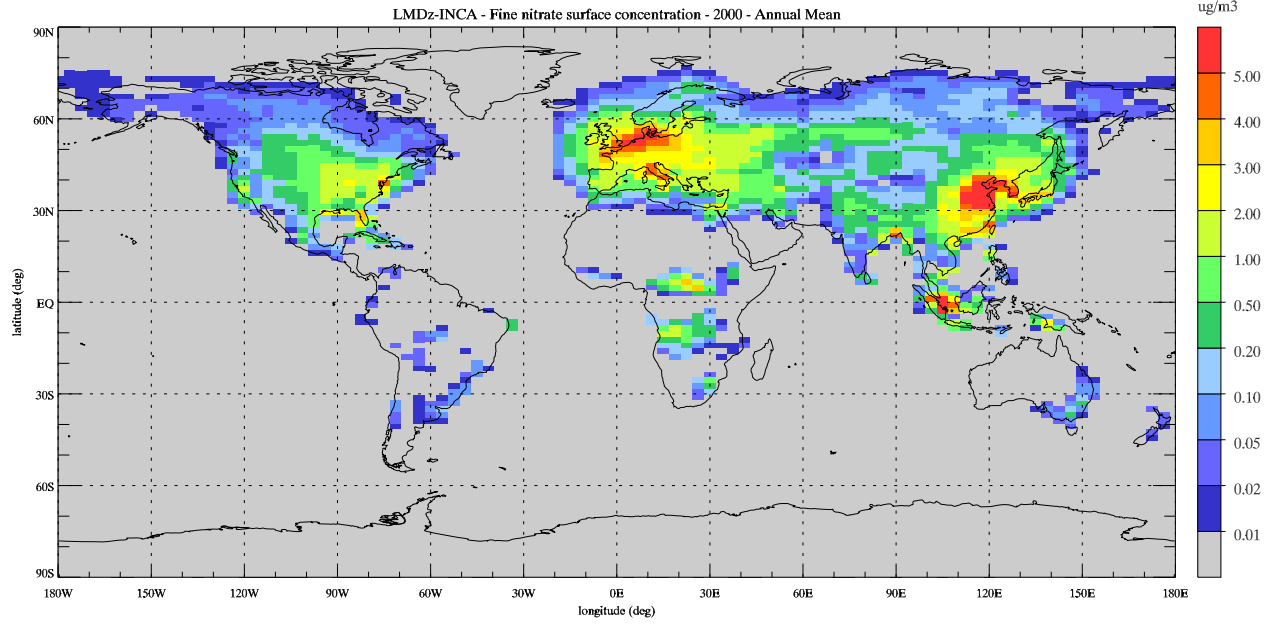


Figure 2

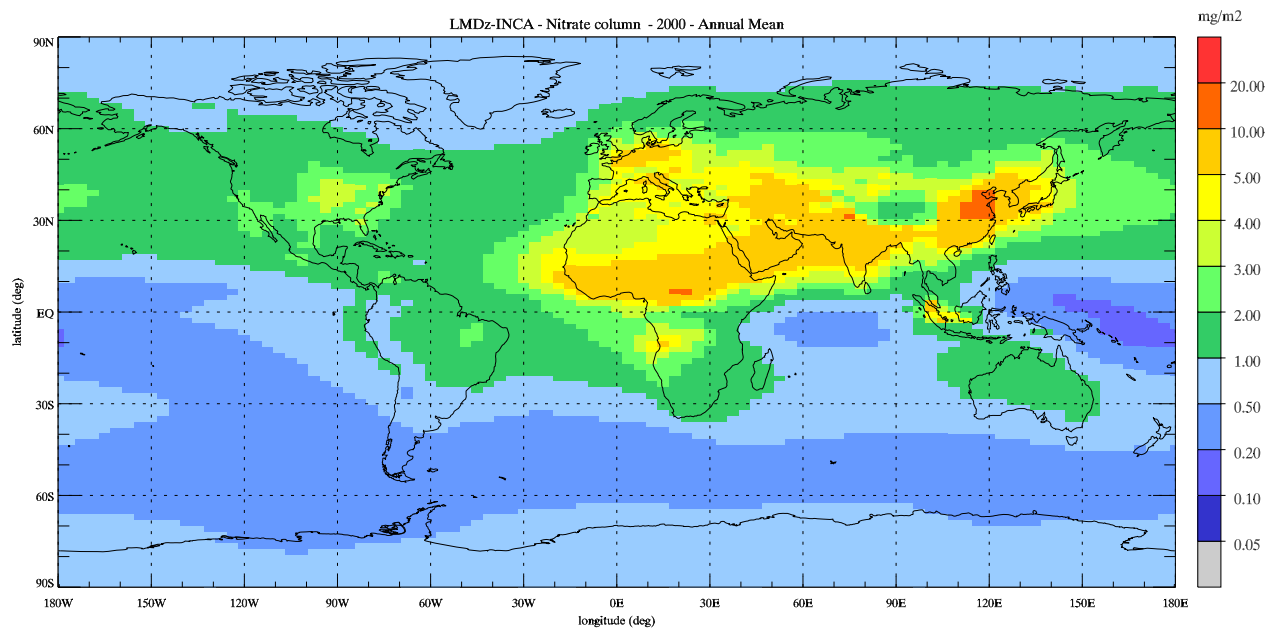
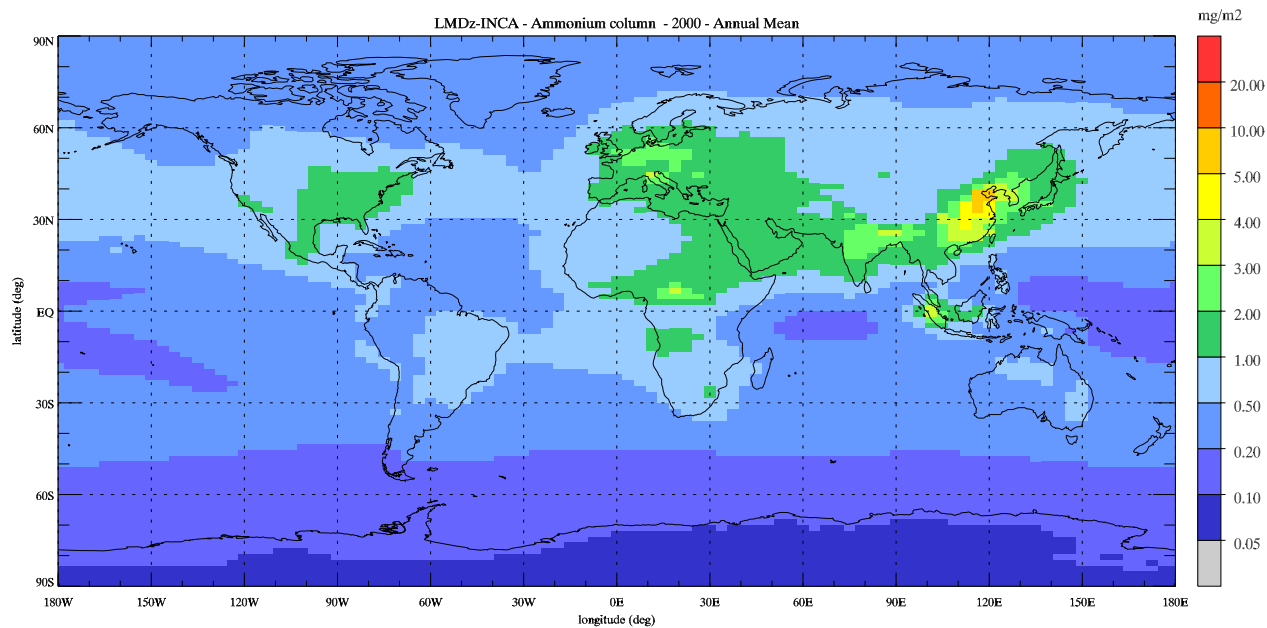
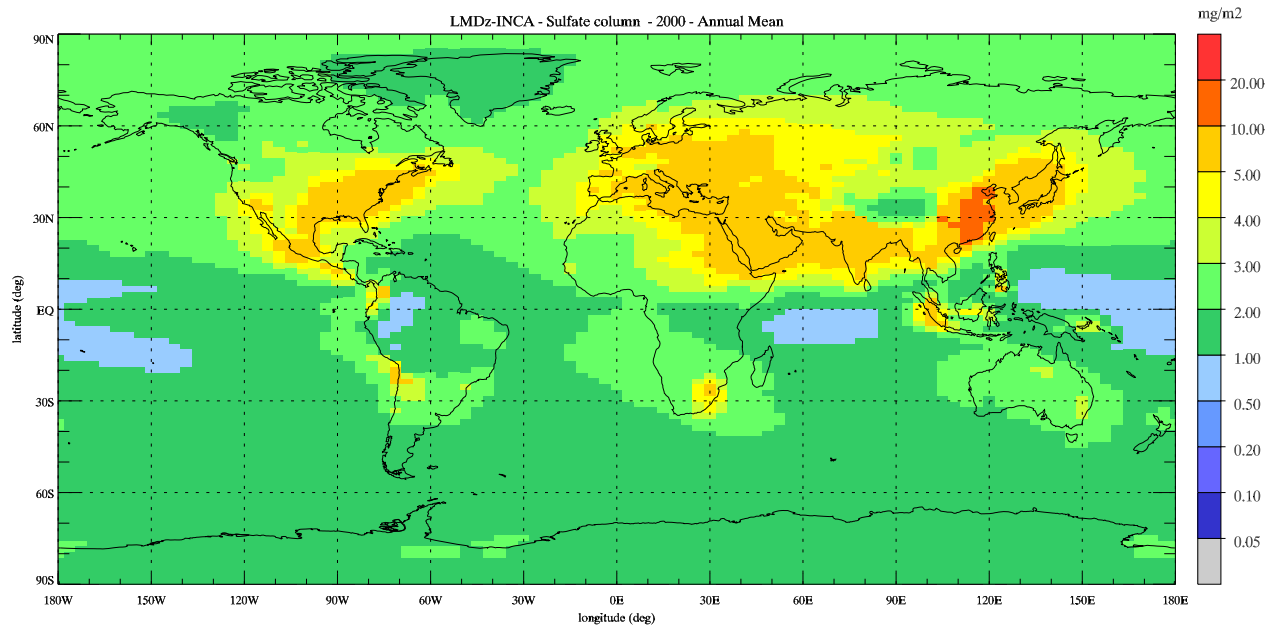


Figure 3

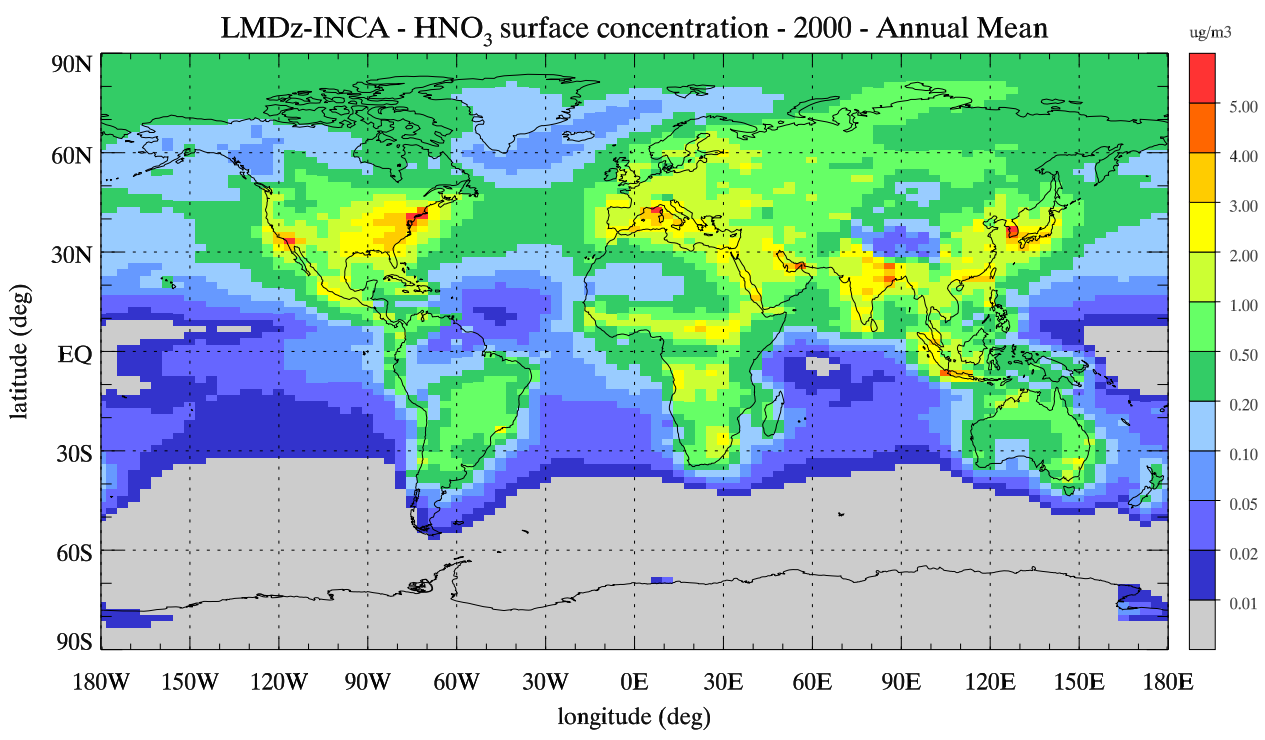
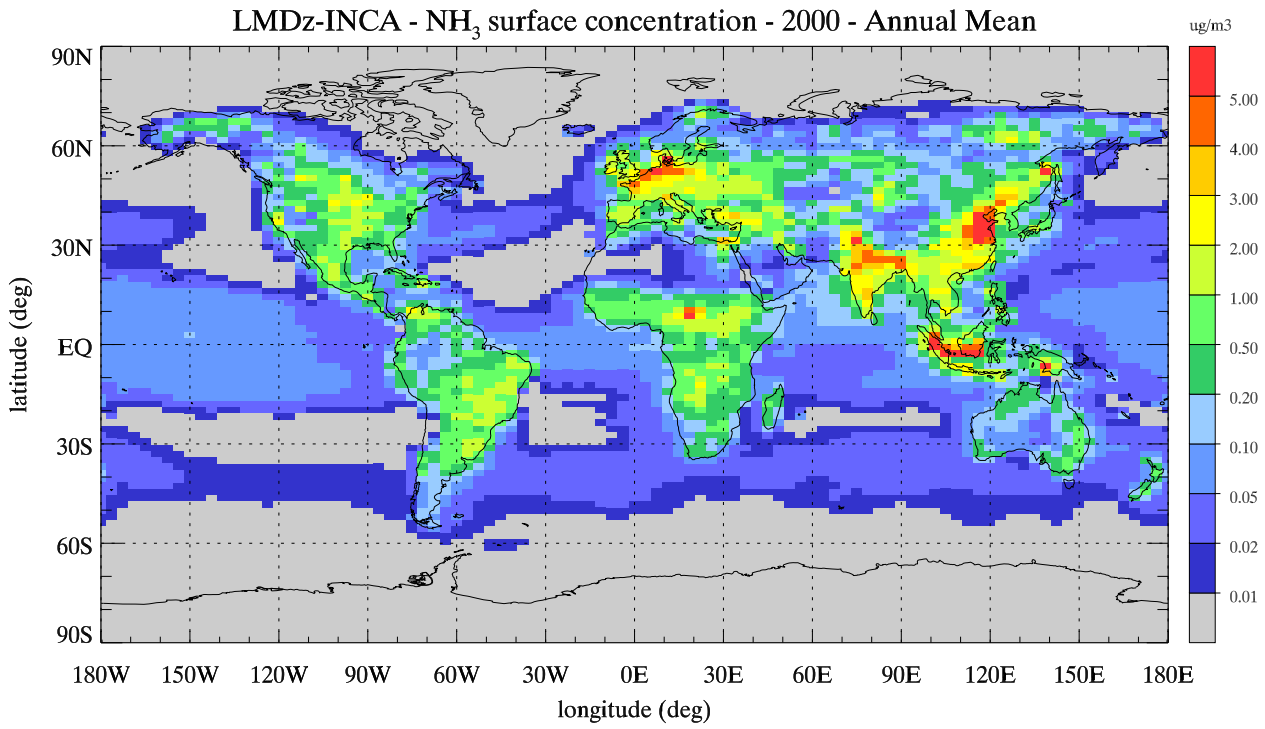


Figure 4

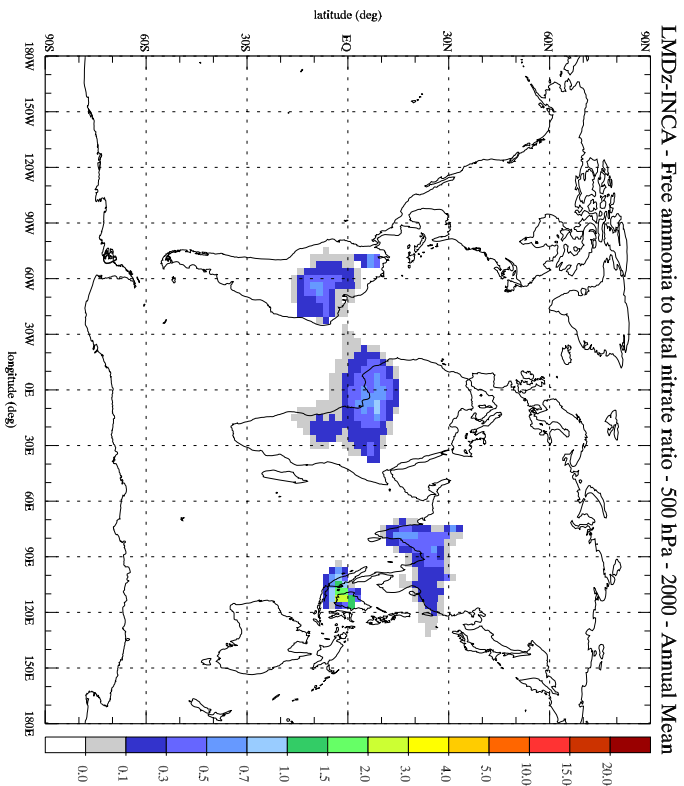
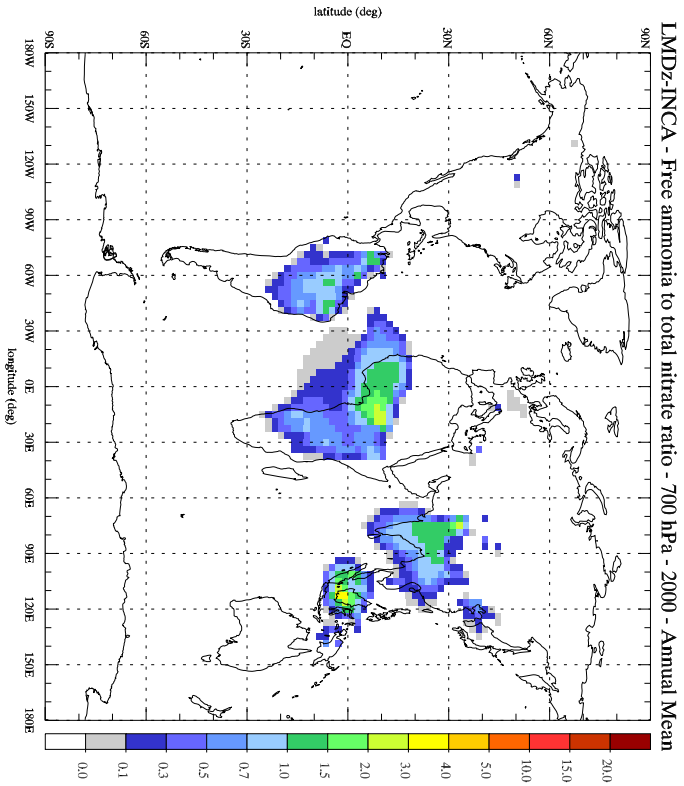
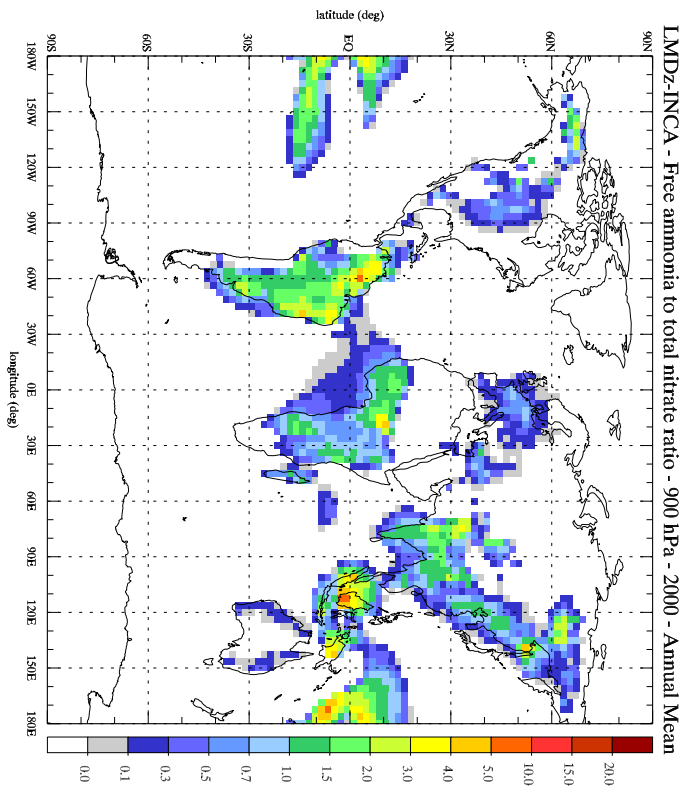
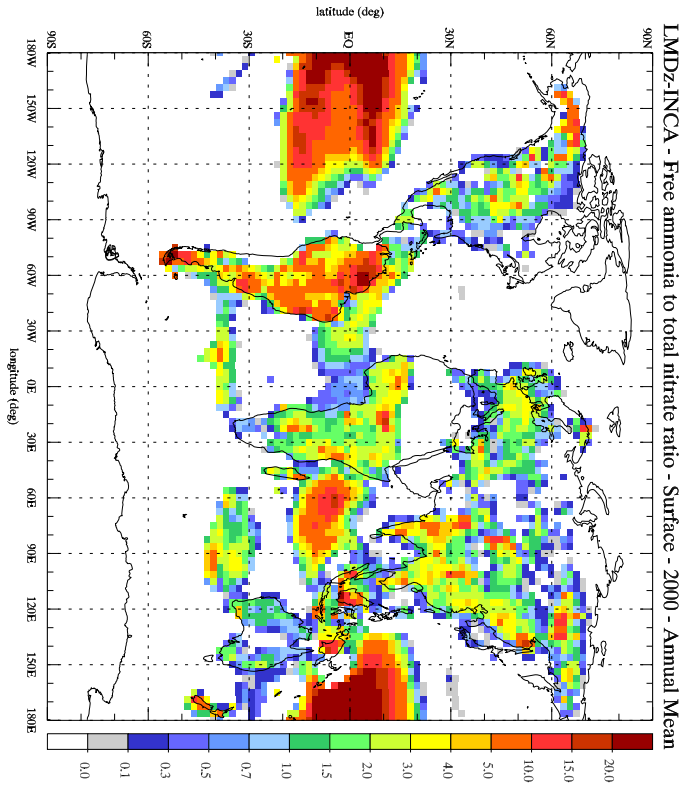


Figure 5

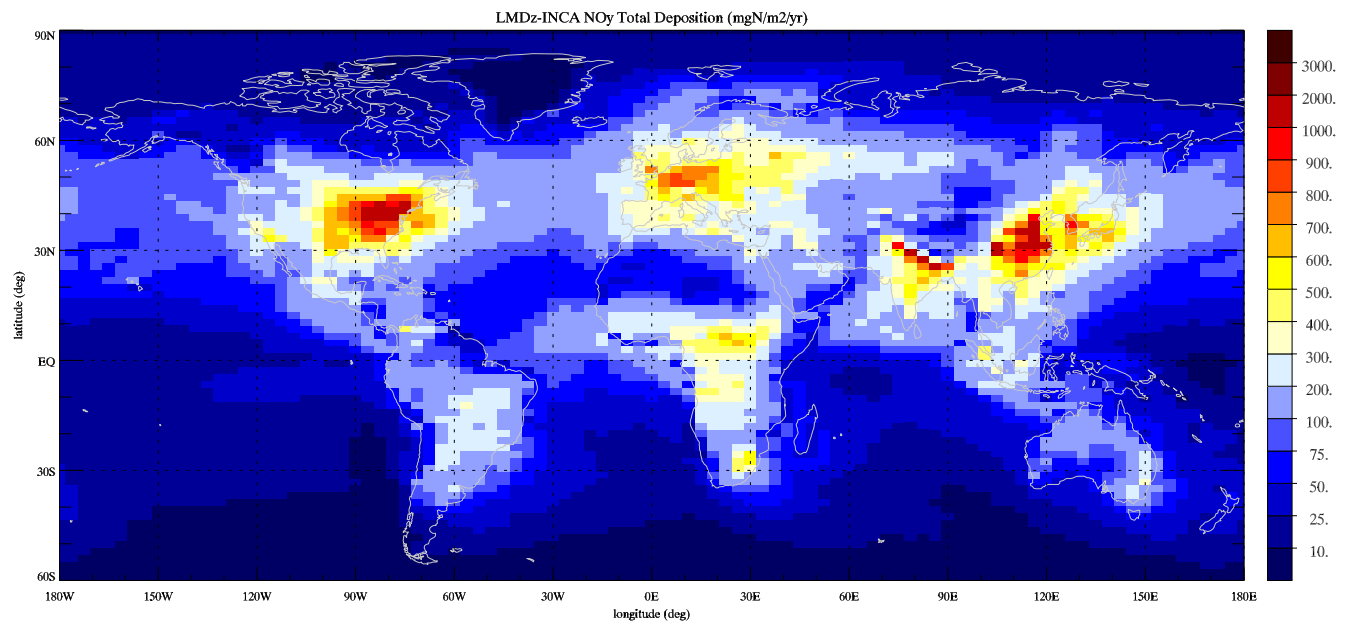
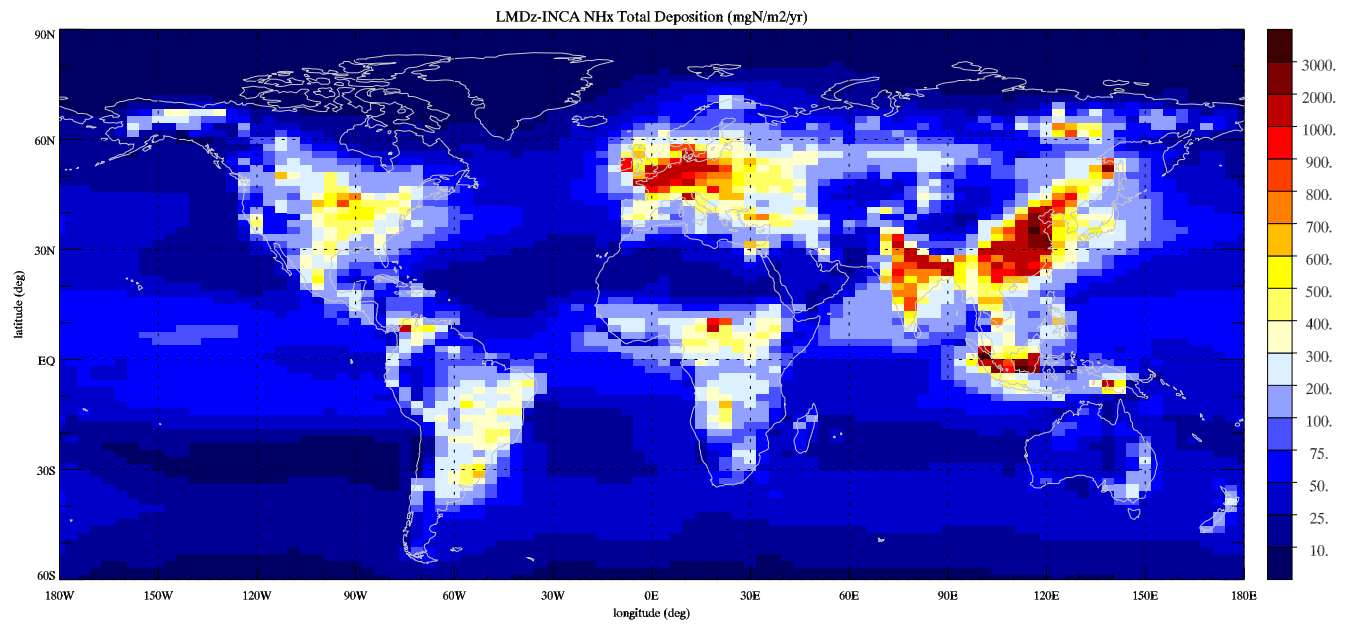
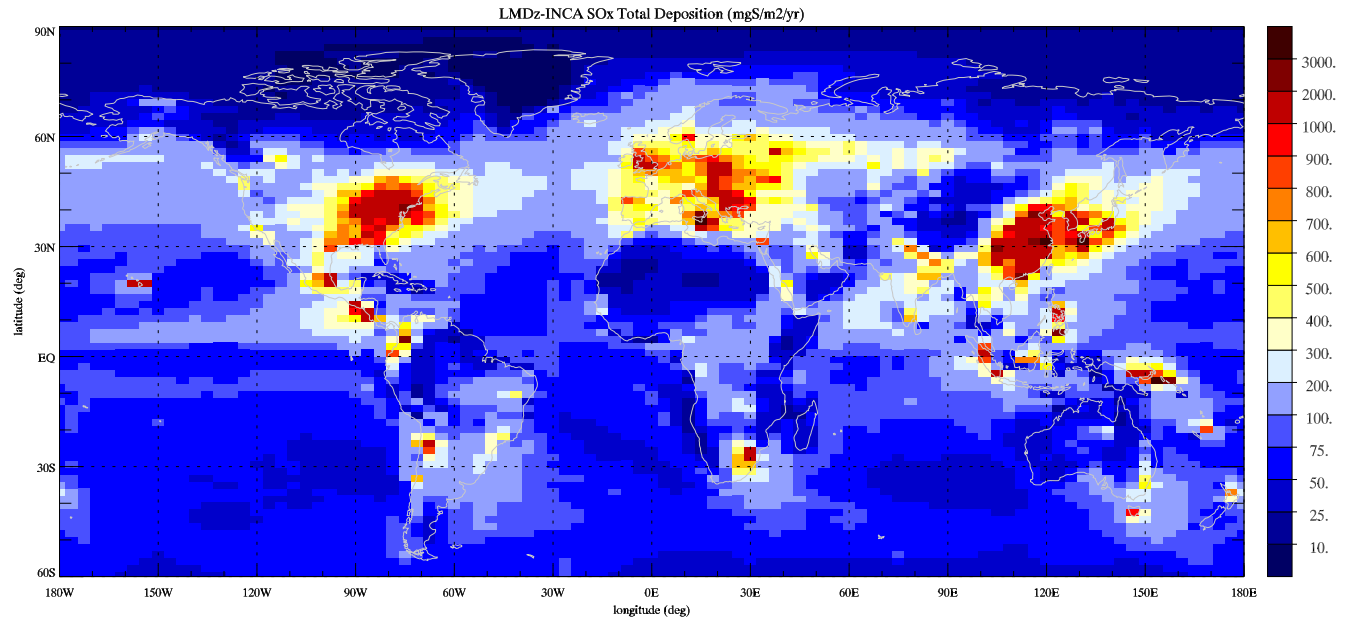


Figure 6

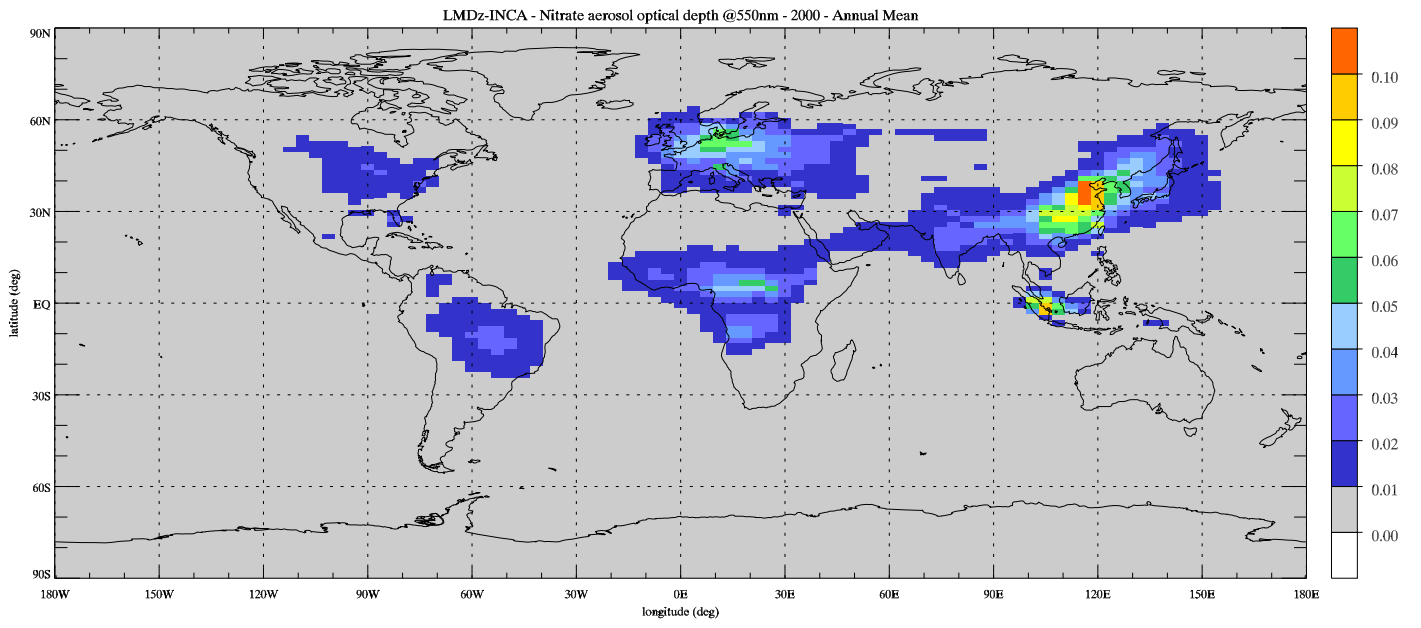
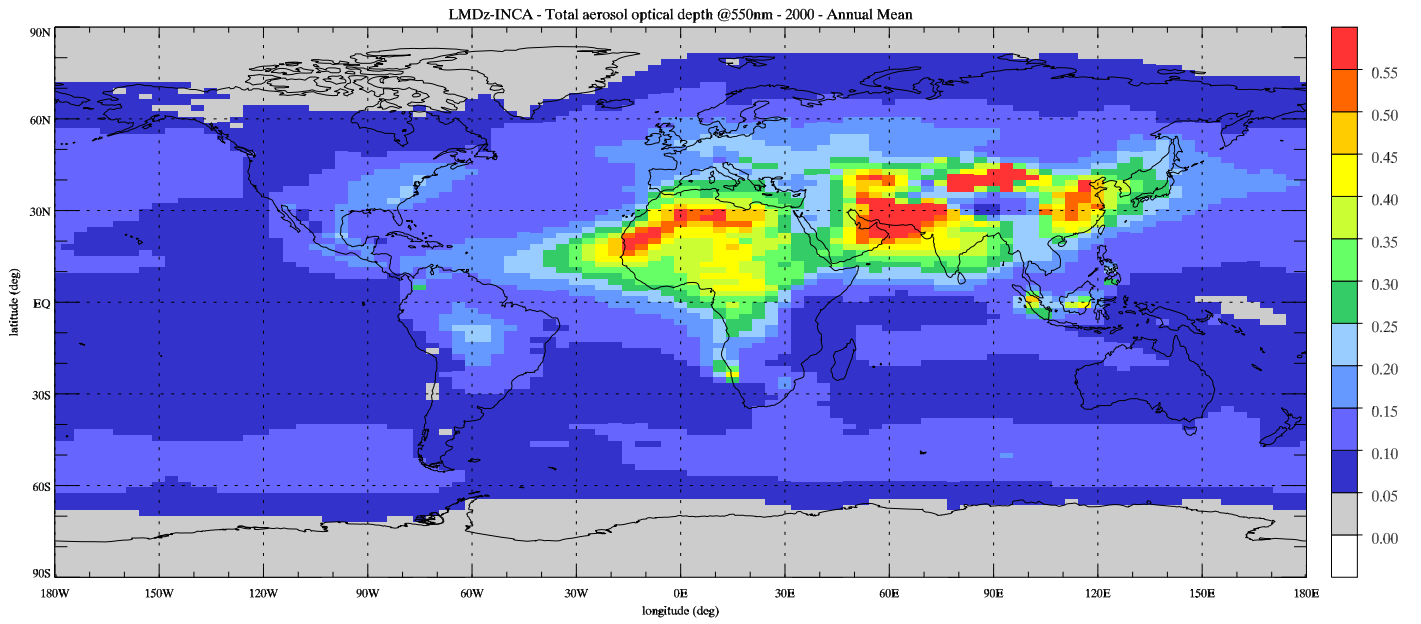


Figure 7

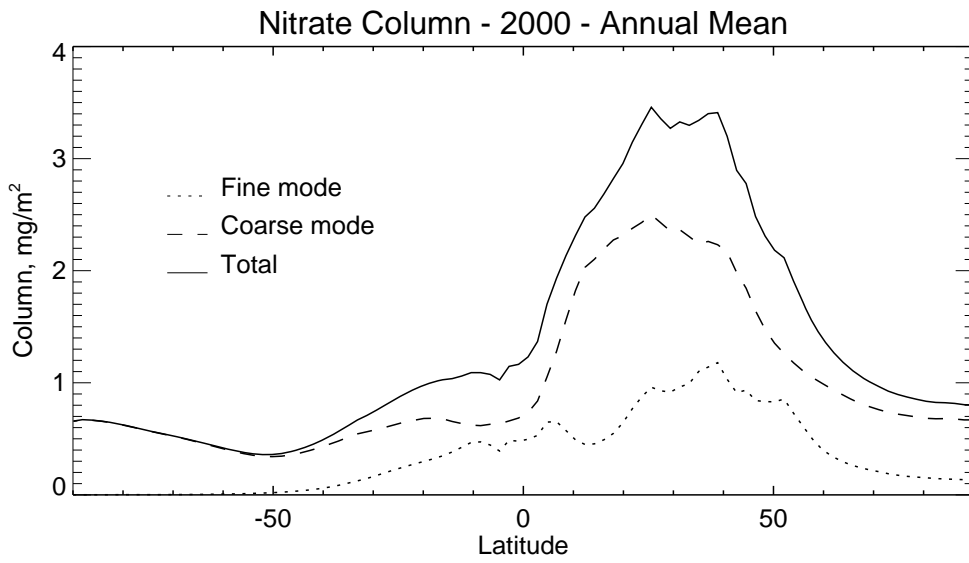


Figure 8a

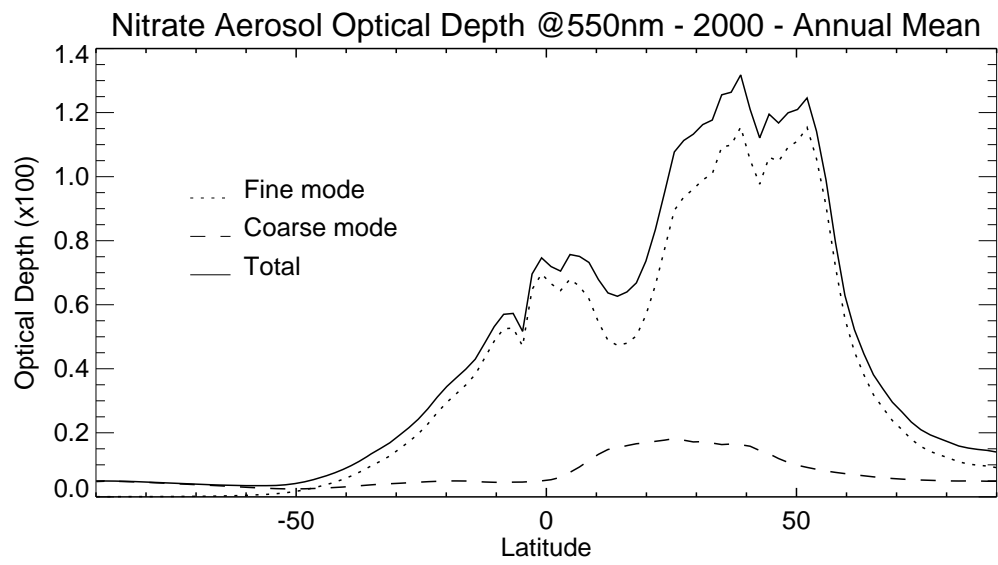


Figure 8b

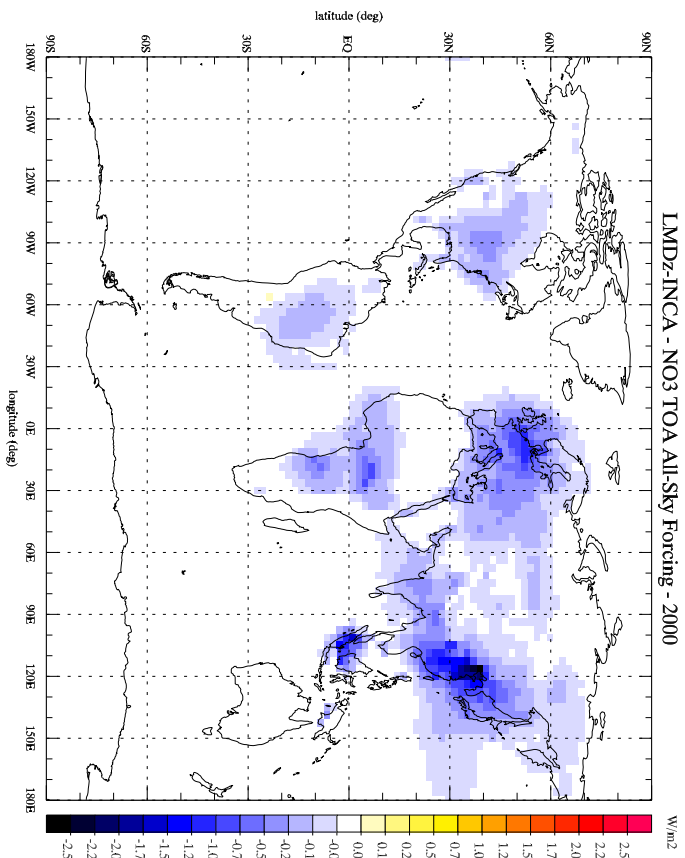
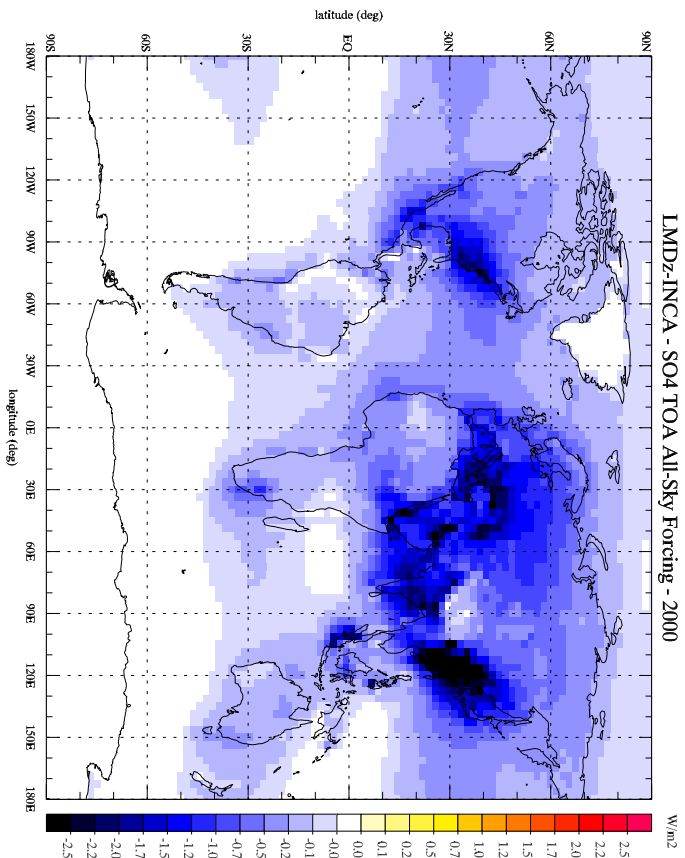
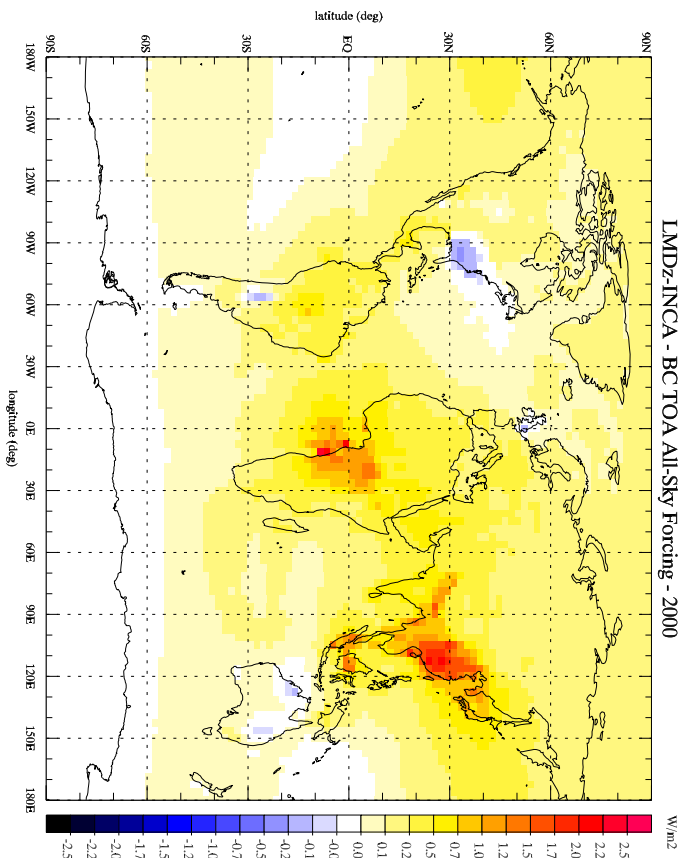
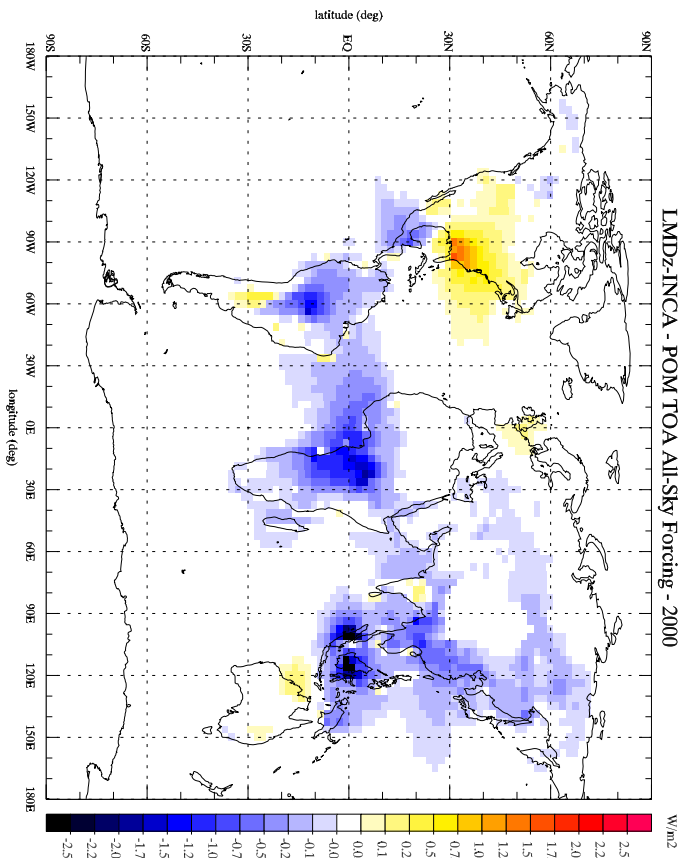


Figure 9

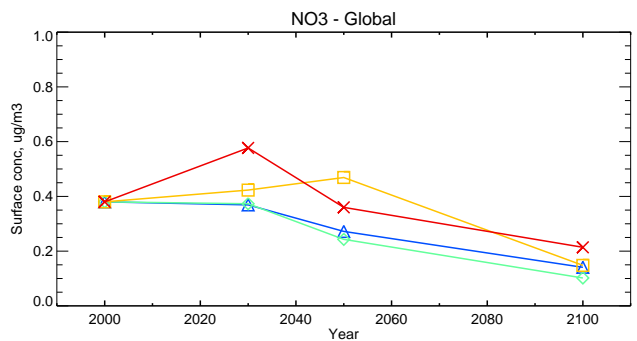
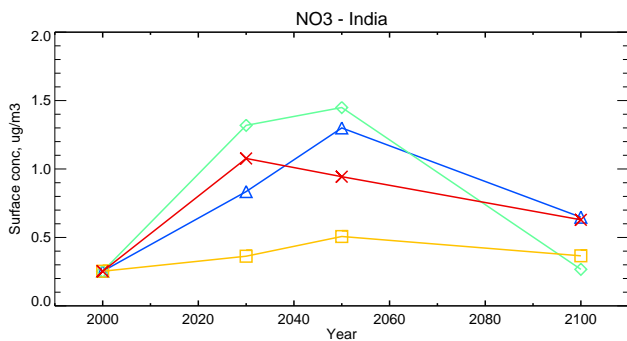
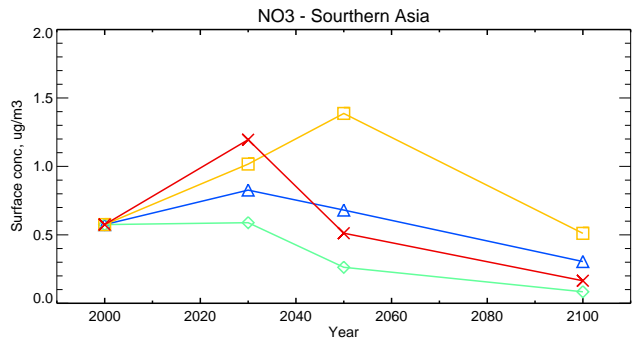
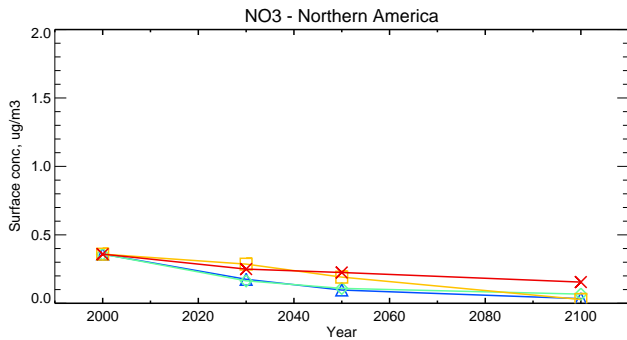
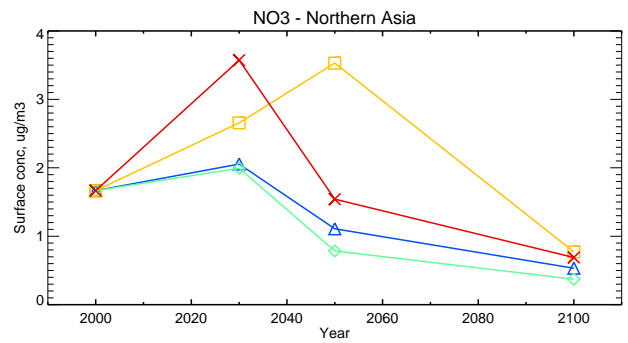
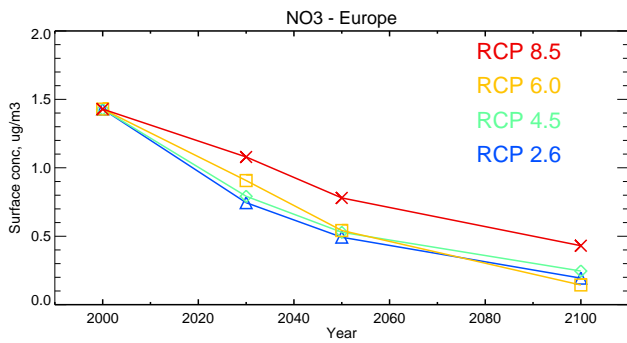


Figure 10

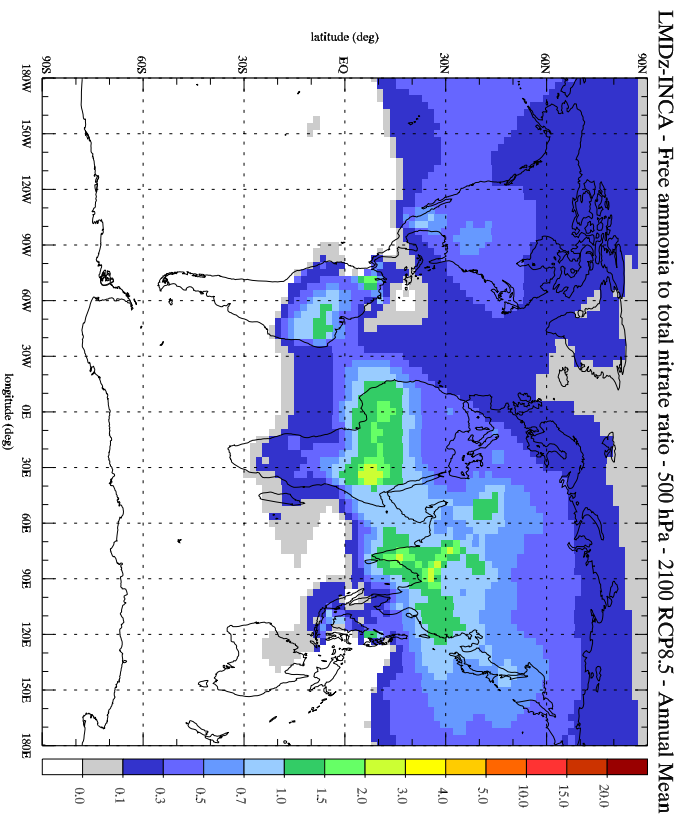
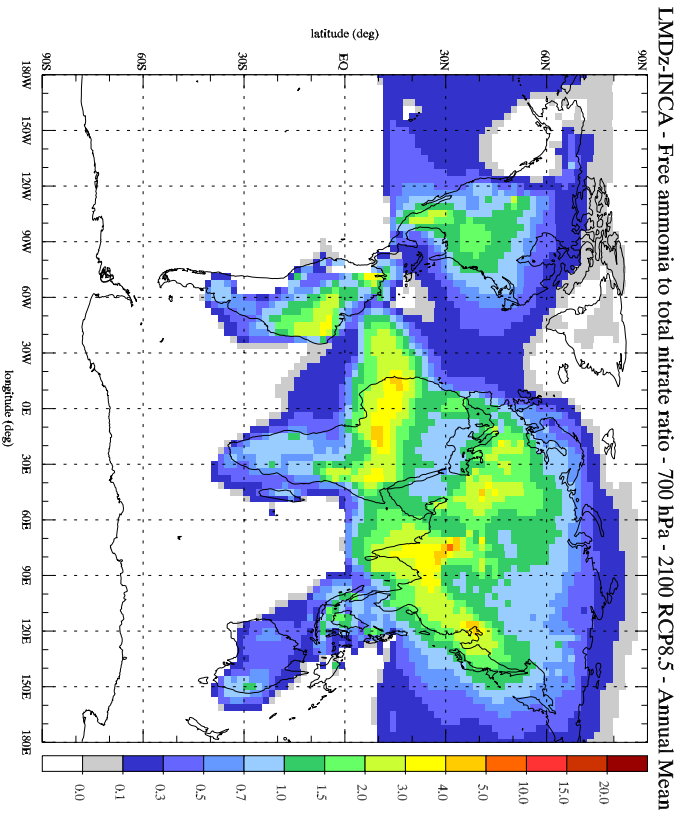
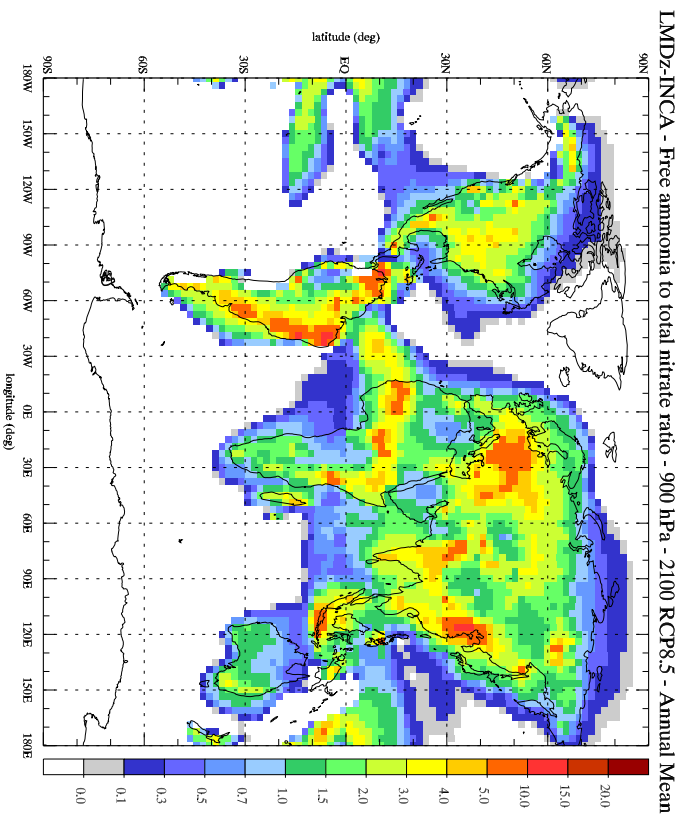
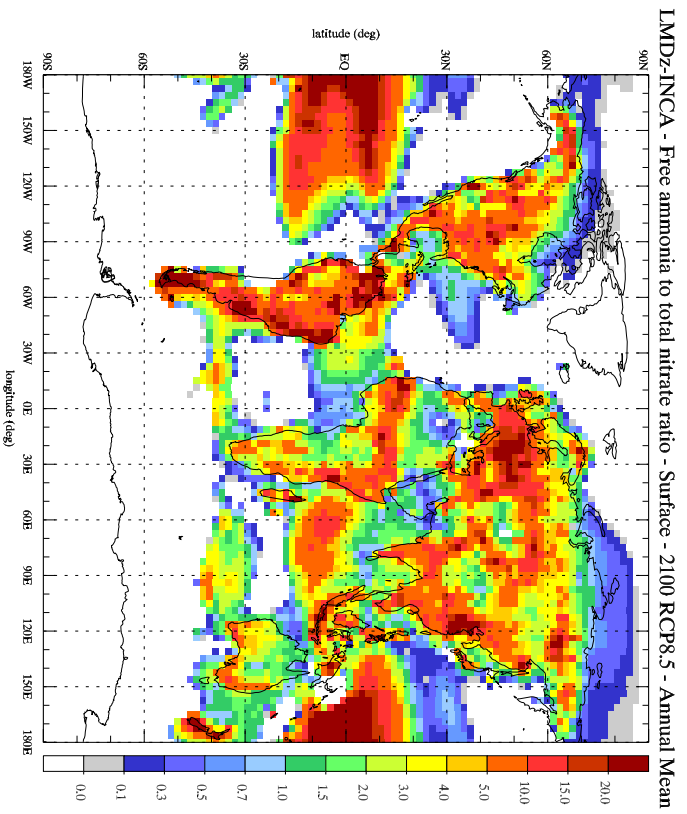


Figure 11

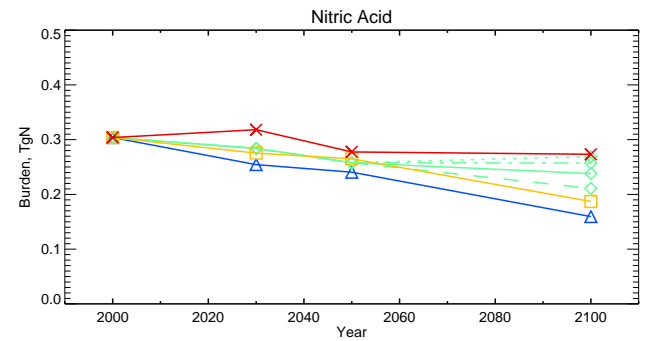
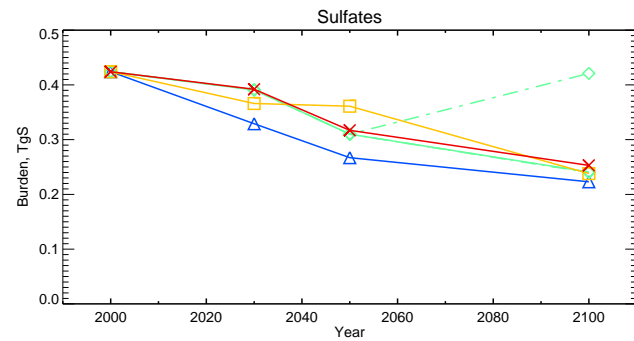
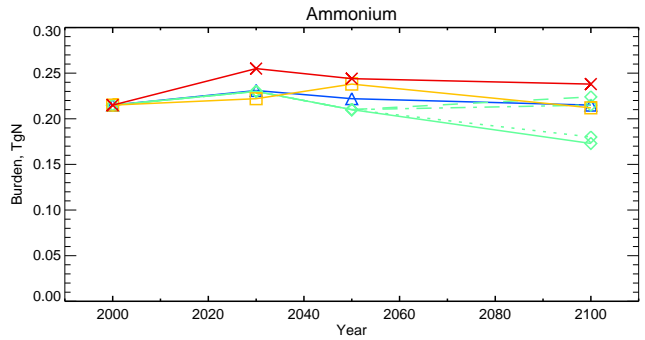
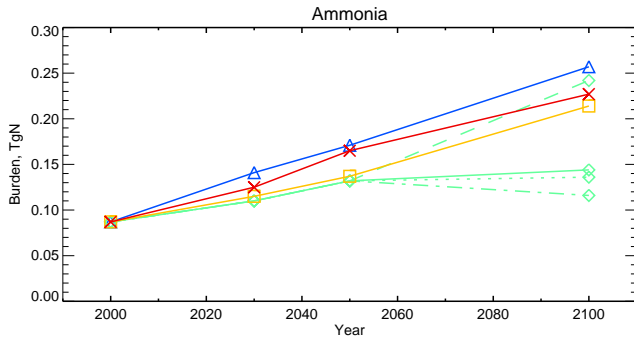
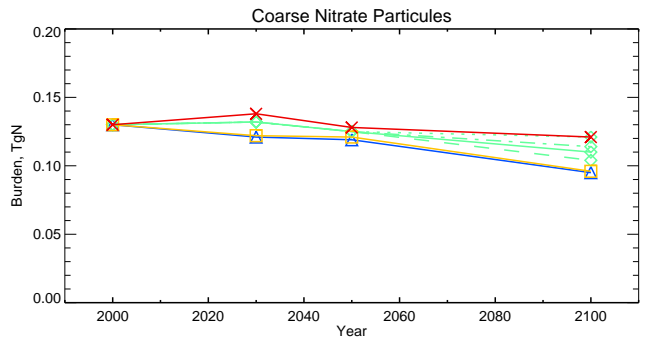
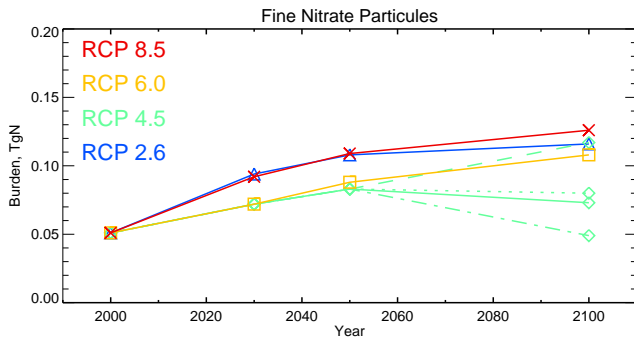


Figure 12

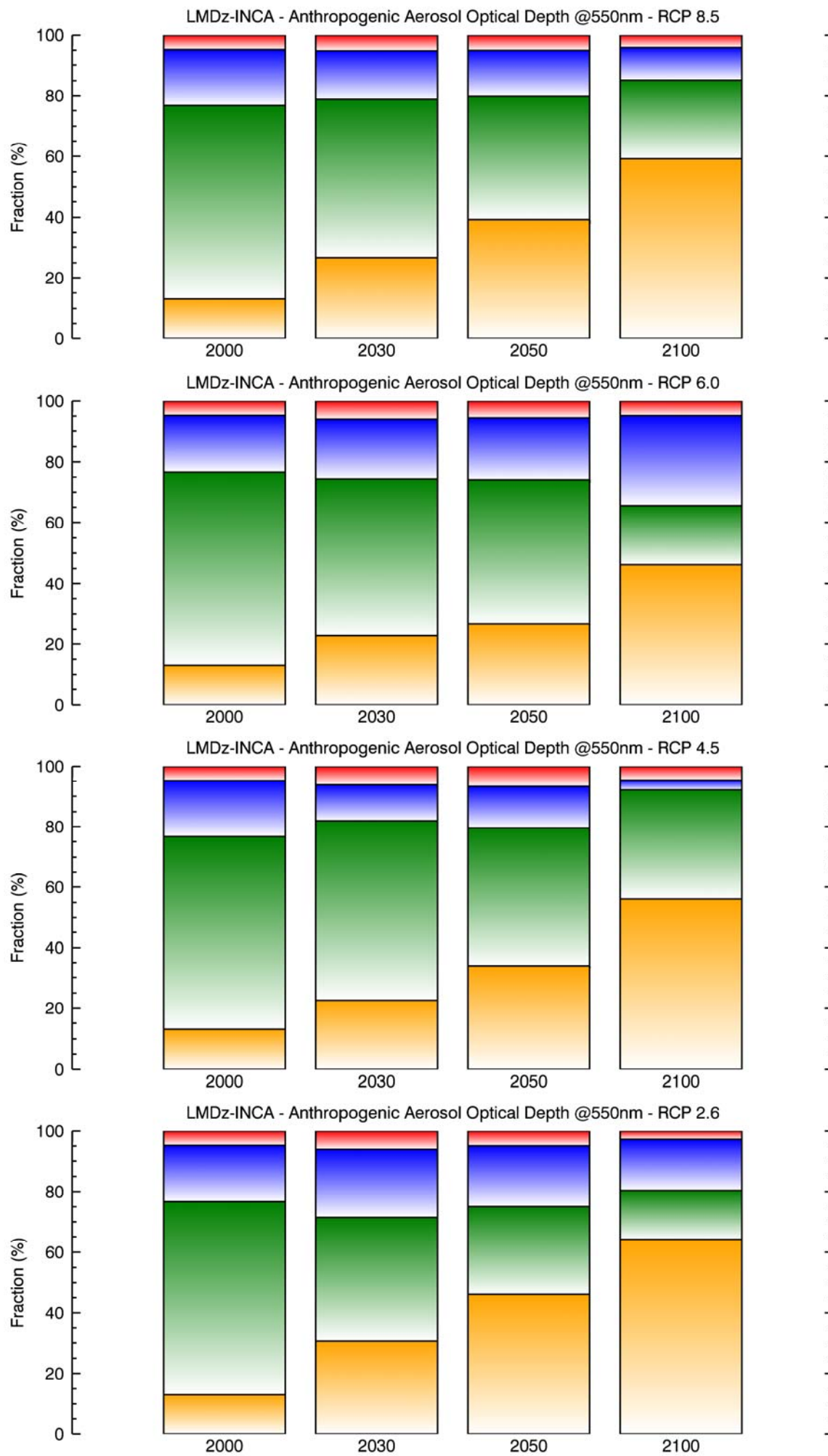


Figure 13

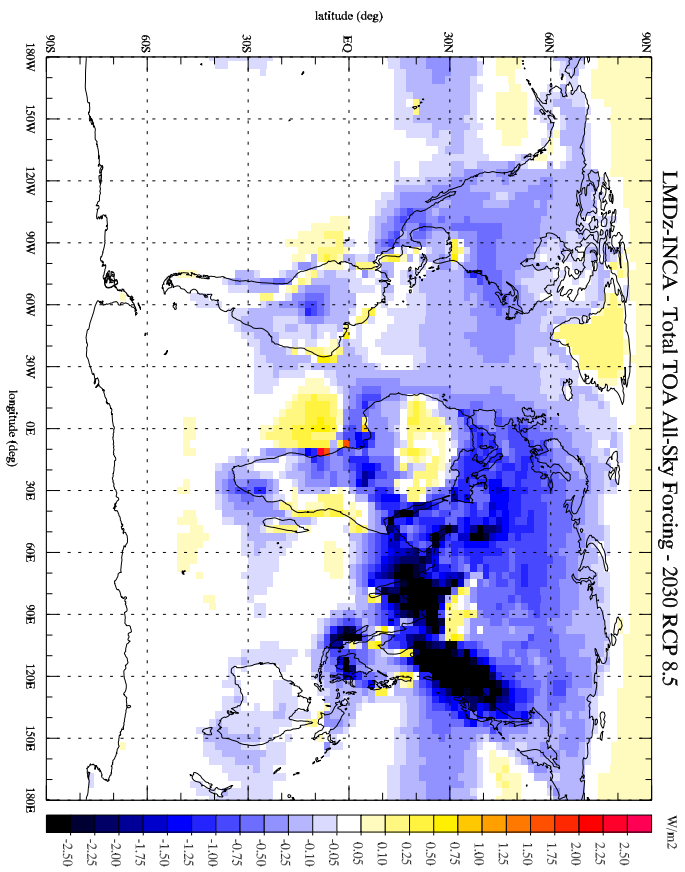
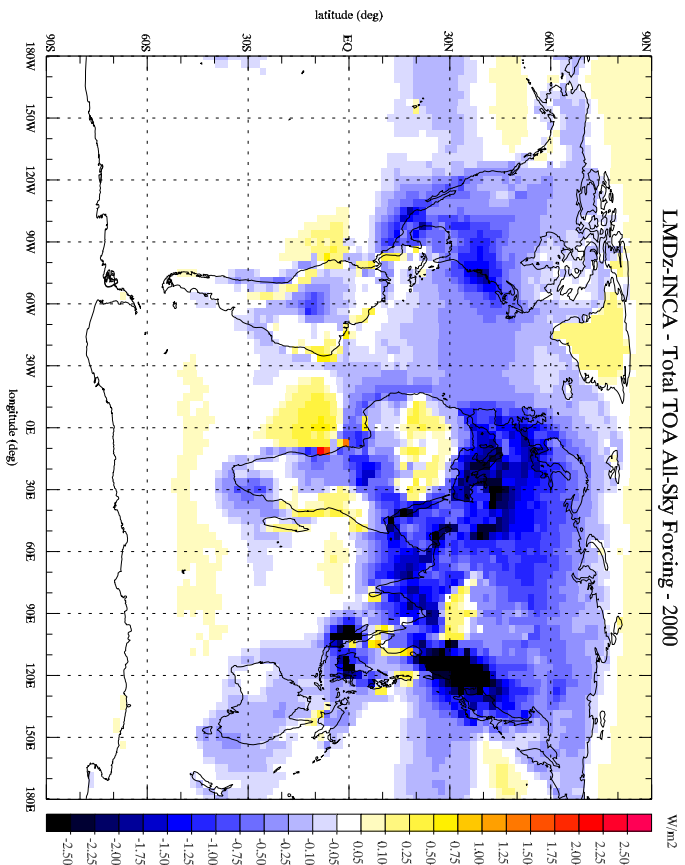
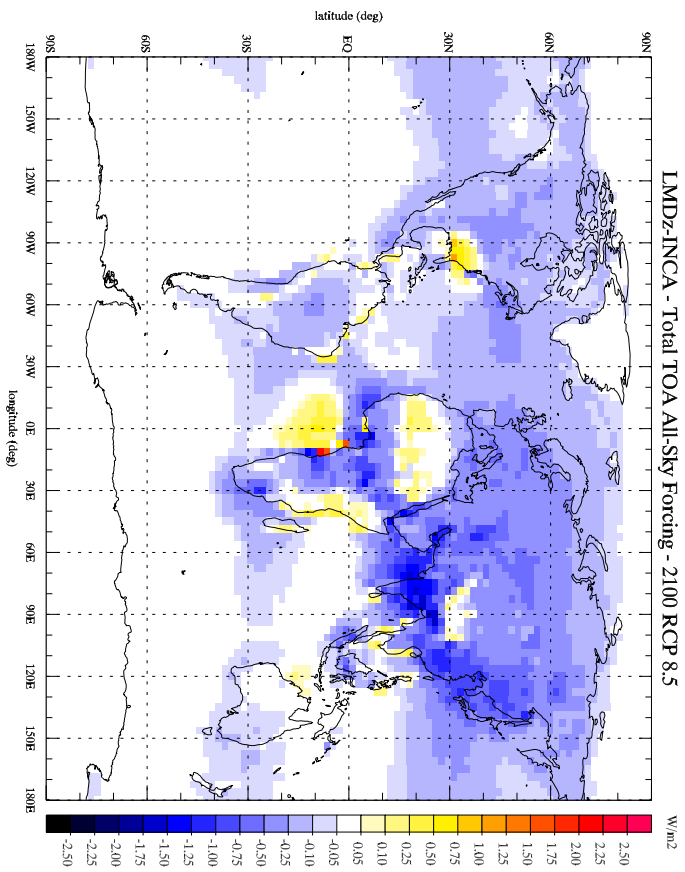
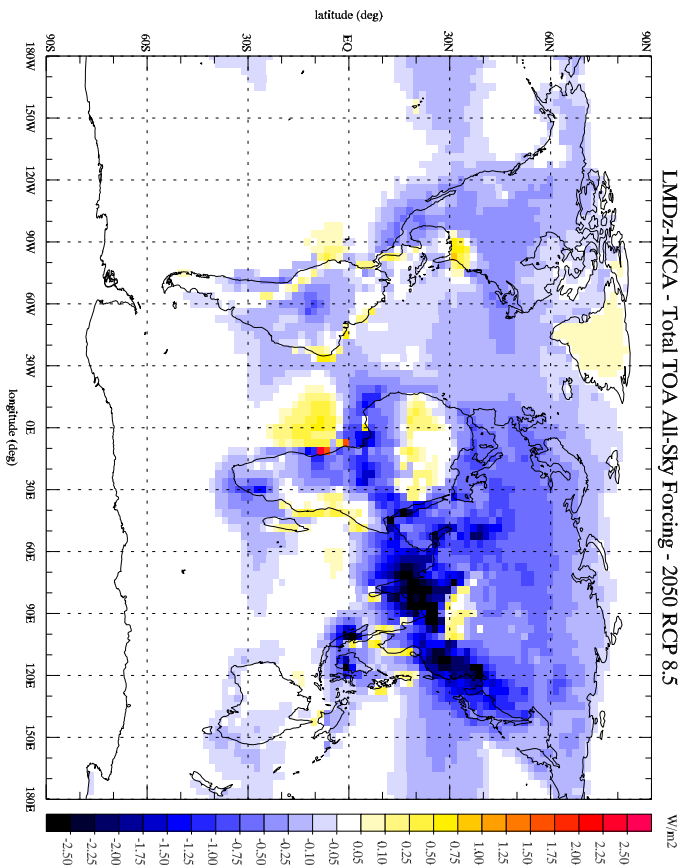


Figure 14

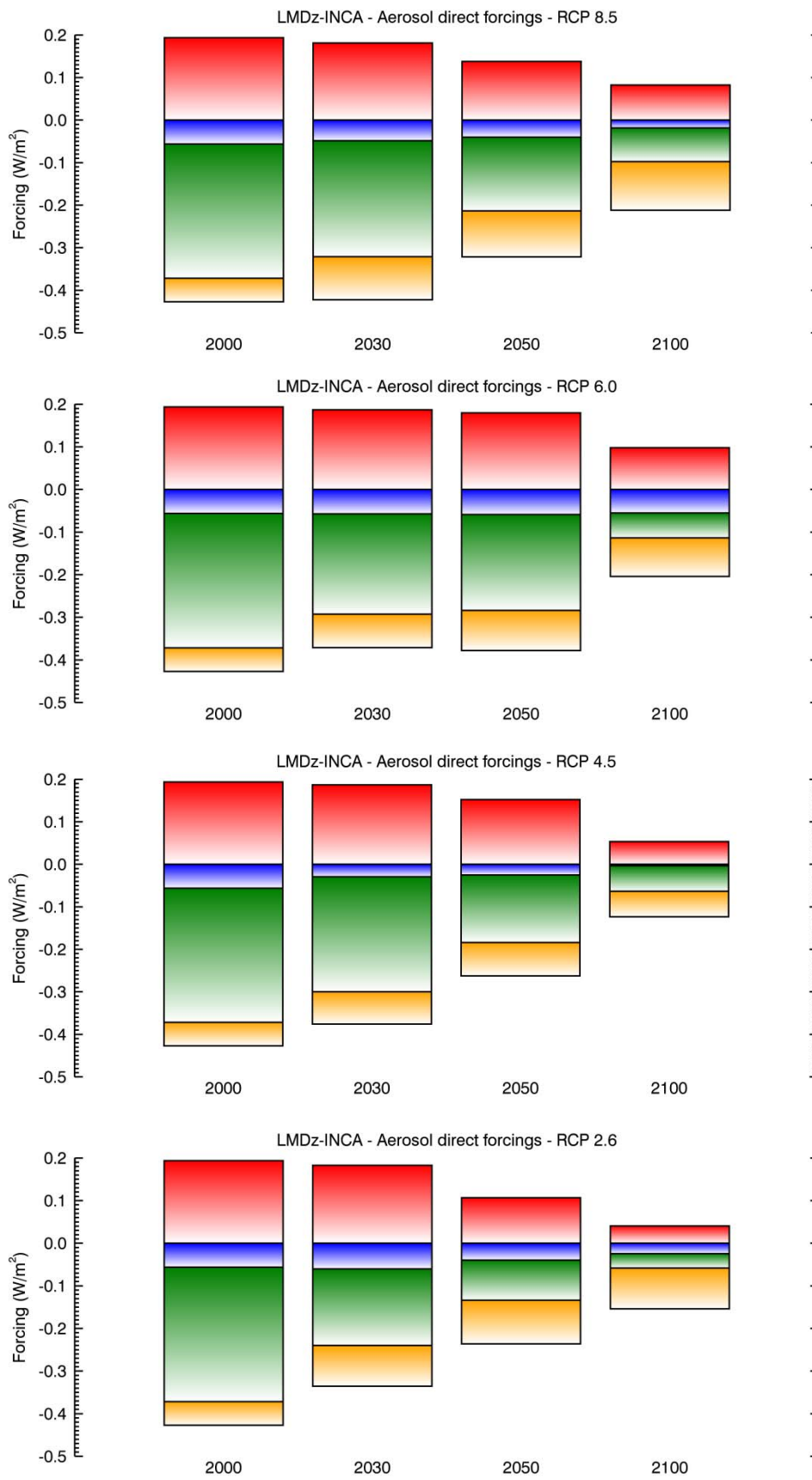


Figure 15

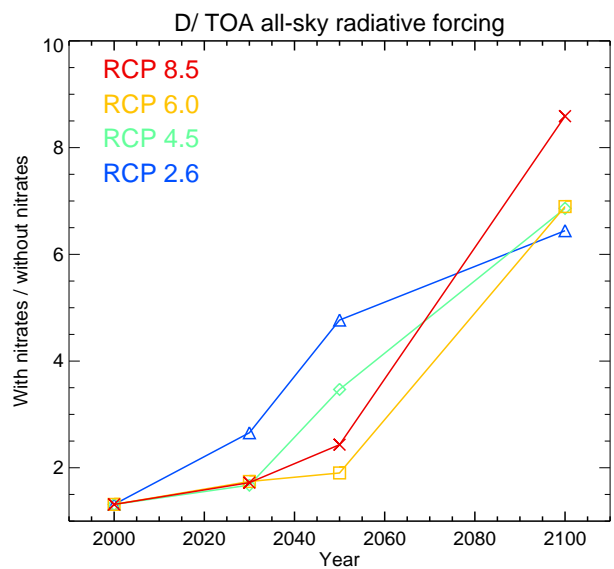
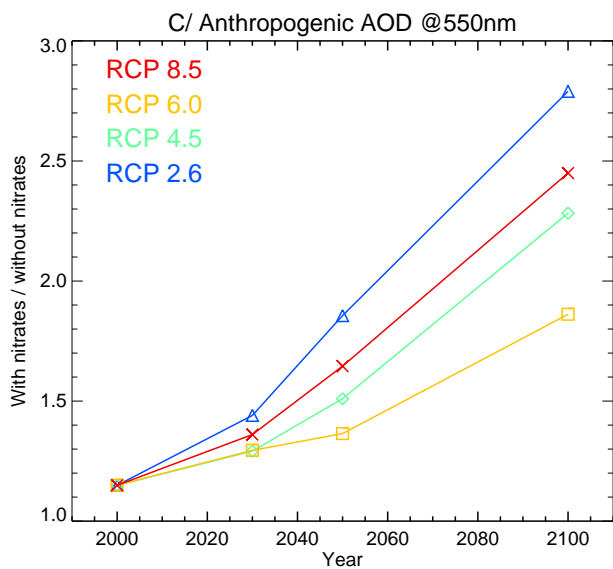
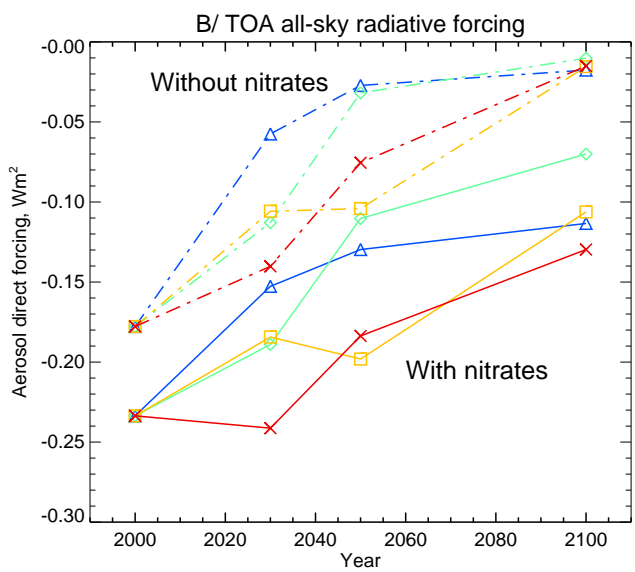
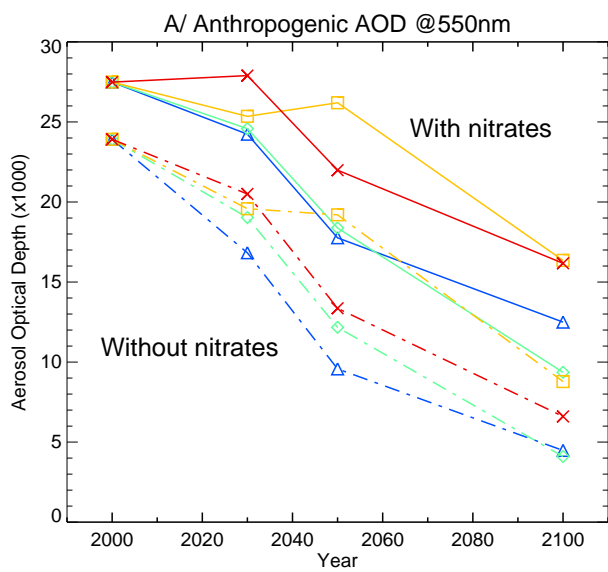


Figure 16